Tailoring Quantum Entanglement of Orbital Angular Momentum

by

Melanie McLaren

Dissertation presented for the degree of Doctor of Science in Physics in the Faculty of Physics at Stellenbosch University

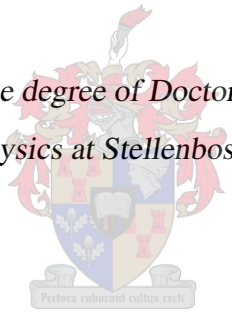

Department of Laser Physics,
University of Stellenbosch,
Private Bag X1, Matieland 7602, South Africa.

Promoter: Prof. A. Forbes, Dr. F.S. Roux, Prof. E. Rohwer

December 2014

Declaration

By submitting this dissertation electronically, I declare that the entirety of the work contained therein is my own, original work, that I am the sole author thereof (save to the extent explicitly otherwise stated), that reproduction and publication thereof by Stellenbosch University will not infringe any third party rights and that I have not previously in its entirety or in part submitted it for obtaining any qualification.

Signature: .....

M. McLaren

Date: 2014/03/20 .....

Abstract

Tailoring Quantum Entanglement of Orbital Angular Momentum

M. McLaren

Department of Laser Physics,

University of Stellenbosch,

Private Bag X1, Matieland 7602, South Africa.

Dissertation: PhDPhys

December 2014

High-dimensional quantum entanglement offers an increase in information capacity per photon; a highly desirable property for quantum information processes such as quantum communication, computation and teleportation. As the orbital angular momentum (OAM) modes of light span an infinite-dimensional Hilbert space, they have become frontrunners in achieving entanglement in higher dimensions. In light of this, we investigate the potential of OAM entanglement of photons by controlling the parameters in both the generation and measurement systems. We show the experimental procedures and apparatus involved in generating and measuring entangled photons in two-dimensions. We verify important quantum tests such as the Einstein, Podolsky and Rosen (EPR) paradox using OAM and angle correlations, as well as a violation of a Bell-type inequality. By performing a full state tomography, we characterise our quantum state and show we have a pure, highly entangled quantum state. We demonstrate that this method can be extended to higher dimensions. The experimental techniques used to generate and measure OAM entanglement place an upper bound on the number of accessible OAM modes. As such, we investigate new methods in which to increase the spiral bandwidth of our generated quantum state. We alter the shape of the pump beam in spontaneous parametric down-conversion and demonstrate an effect

on both OAM and angle correlations. We also made changes to the measurement scheme by projecting the photon pairs into the Bessel-Gaussian (BG) basis and demonstrate entanglement in this basis. We show that this method allows the measured spiral bandwidth to be optimised by simply varying the continuous radial parameter of the BG modes. We demonstrate that BG modes can be entangled in higher dimensions compared with the commonly used helical modes by calculating and comparing the linear entropy and fidelity for both modes. We also show that quantum entanglement can be accurately simulated using classical light using back-projection, which allows the study of projective measurements and predicts the strength of the coincidence correlations in an entanglement experiment. Finally, we make use of each of the techniques to demonstrate the effect of a perturbation on OAM entanglement measured in the BG basis. We investigate the self-healing property of BG beams and show that the classical property is translated to the quantum regime. By calculating the concurrence, we see that measured entanglement recovers after encountering an obstruction.

Uittreksel

Kwantumverwikkeling van orbitale hoekmomentum

("Tailoring Quantum Entanglement of Orbital Angular Momentum")

M. McLaren

Departement van laserfisika,

Universiteit van Stellenbosch,

Privaatsak X1, Matieland 7602, Suid Afrika.

Proefskrif: (PhDPhys)

Desember 2014

Hoë-dimensionele kwantumverstrengeldheid bied 'n toename in inligtingskapasiteit per foton. Hierdie is 'n hoogs wenslike eienskap vir kwantum inligting prosesse soos kwantum kommunikasie, berekening en teleportasie. Omdat die orbitale hoekmomentum (OAM) modusse van lig 'n oneindig dimensionele Hilbertruimte beslaan, het dit voorlopers geword in die verkryging van verstrengeling in hoër dimensies. In die lig hiervan, ondersoek ons die potensiaal van OAM verstrengeling van fotone deur die parameters in beide die generering en meting stelsels te beheer. Ons toon die eksperimentele prosedures en apparaat wat betrokke is by die generering en die meet van verstrengelde fotone in twee dimensies. Ons verifieer kwantumtoetse, soos die Einstein, Podolsky en Rosen (EPR) paradoks vir OAM en die hoekkorrelasies, sowel as 'n skending van 'n Bell-tipe ongelykheid. Deur middel van 'n volledige toestand tomografie, karakteriseer ons die kwantum toestand en wys ons dat dit 'n suiwer, hoogs verstrengel kwantum toestand is. Ons toon ook dat hierdie metode uitgebrei kan word na hoër dimensies. Die eksperimentele tegnieke wat tydens die generasie en meet van OAM verstrengeling gebruik is, plaas 'n bogrens op die aantal toeganklik OAM modusse. Dus ondersoek ons nuwe metodes om die spiraal bandwydte van ons gegenereerde

kwantum toestand te verhoog. Ons verander die vorm van die pomp bundel in spontane parametriese af-omskakeling en demonstreer die uitwerking daarvan op beide OAM en die hoekkorrelasies. Ons het ook veranderinge aan die meting skema gemaak deur die foton pare op die Bessel-Gauss (BG) basis te projekteer. Ons wys dat hierdie metode die gemeetde spiraal bandwydte kan optimeer deur eenvoudig die kontinue radiale parameter van die BG modes te verander. Ons demonstreer dat BG modusse verstrengel kan word in hoër dimensies as die heliese modusse, wat algemeen gebruik word, deur berekeninge te maak en te vergelyk met lineêre entropie en vir beide modusse. Ons wys ook dat kwantumverstrengling akkuraat nageboots kan word, met behulp van die klassieke lig terug-projeksie, wat die studie van projeksie metings toelaat en voorspel die krag van die saamval korrelasies in ’n verstrengeling eksperiment. Ten slotte, gebruik ons elk van die tegnieke om die effek van ’n storing op OAM verstrengling wat in die BG basis gemeet is, te demonstreer. Ons ondersoek die self-genesingseienskap van BG bundels en wys dat die klassieke eienskap vertaal na die kwantum-gebied. Deur die berekening van die konkurrensie (concurrence), sien ons dat die gemeetde verstrengeling herstel word nadat ’n obstruksie ondervind is.

Acknowledgements

I would like to express my gratitude to everyone who provided support throughout the course of my PhD work. Specifically, I would like to thank the following people:

My supervisors, Prof. Andrew Forbes and Dr. Stef Roux, thank you for all the guidance and support during my PhD. In particular, I am grateful to Andrew for the detailed discussions and planning of each aspect of my PhD work. I have gained not only valuable experimental techniques, but have also learnt the art to expressing one's work to the international community, both in journals and at conferences.

I am also grateful to the CSIR National Laser Centre for providing me with opportunities to conduct this research within our own labs as well as those of our collaborators around the world.

These collaborators include Prof. Miles Padgett from the University of Glasgow, who has offered a great deal of support by allowing me to visit his labs to work together with him and his students, Dr. Jacqui Romero and Daniele Giovannini. Both Jacqui and Daniele have become great friends, whom I hope to continue to work with in the future. I was also fortunate to visit the University of Ottawa and work within Prof. Robert Boyd's group, which at the time was coordinated by Dr. Jonathan Leach. Much of my experimental knowledge was gained from Jonathan on my first visit. However, it was during my second visit, working with Megan Agnew, Xinru Cheng, Eliot Bolduc and Jonathan, that I really learnt to enjoy my PhD and for that I am truly grateful.

While at the NLC, there were two individuals, Angela (the Doc) and Darryl, who provided a great deal of support both in and out of the lab. Experimental work is not without its frustrations, but thanks to Ange and Darryl, I managed to maintain my sanity and come out the better for it. I look forward to seeing your names in *Forbes* top 100.

Lastly, I'd like to thank my family and friends for supporting me throughout these years.

I am grateful to my Dad for enthusiastically supporting my pursuit of this degree, I know it has been difficult at times, but hopefully it was all worth it. Marko, who has put up with this journey from the beginning and I am incredibly thankful for all our discussions about work, family and the future, which kept me motivated throughout.

Dedications

To my parents

Contents

Declaration iii

Abstract v

Uittreksel vii

Acknowledgements ix

Dedications xi

Contents xii

List of Figures xv

List of Tables xxv

List of Publications xxvii

Peer-reviewed Journal Papers: xxvii

International Conference Papers: xxviii

National Conference Papers: xxviii

Nomenclature xxxi

List of symbols xxxi

Acronyms/Abbreviations xxxii

1 Introduction 1

1.1 History 2

1.2 Angular momentum of light 3

1.3 Entangled photon states 8
1.4 Entangled states of OAM 9
1.5 Outline 11

2 Experimental methods and apparatus 13
2.1 Spontaneous Parametric Down-conversion 14
2.2 OAM generation and measurement 17
2.3 Experimental setup 21
2.4 Quantum measurements 25
2.5 Conclusion 40

3 Shaping the pump beam 43
3.1 Introduction 44
3.2 Pump shape and SPDC 44
3.3 Experiment and results 47
3.4 Conclusion 50

4 Bessel-Gaussian entanglement 51
4.1 Introduction 52
4.2 Theory 53
4.3 Back-projection results 57
4.4 Down-conversion experiment and results 63
4.5 Conclusion 69

5 Self-healing of quantum entanglement 71
5.1 Introduction 72
5.2 Bessel beams 73
5.3 Setup 74
5.4 Measuring the degree of entanglement 78
5.5 Discussion 81

6 Conclusion 83
6.1 Future Work 85

Bibliography **89**

List of Figures

1.1 (a) The superposition of the electric fields of two linearly polarised fields, $\pi/2$ out of phase, produce circularly polarised light. (b) The Poincaré sphere can be used to represent any polarisation state, where $|H\rangle$ and $|V\rangle$ represent horizontally and vertically polarised light, respectively, and $|L\rangle$ and $|R\rangle$ represent left and right circularly polarised light, respectively. 4

1.2 (a) A Gaussian beam with planar phasefronts does not carry orbital angular momentum (OAM). (b) A beam with helical phasefronts will carry OAM, the amount of which is specified by the azimuthal index ℓ. 5

1.3 Bloch sphere diagram used to describe any orbital angular momentum state with azimuthal index ℓ. 6

1.4 Laguerre-Gaussian modes have both a radial p and an azimuthal ℓ component. . 7

2.1 Conservation of momentum and energy in the process of parametric down-conversion, where $\mathbf{k}$ and ω are the wavevectors and frequencies of the respective photons. 14

2.2 SPDC is the most efficient method for producing entangled photons, however, the probability of a spontaneous decay into a pair of entangled photons is very low. Therefore a very sensitive electron multiplier CCD camera is needed to image the ring of photons. (a) Far-field image of the collinear down-converted light from the non-linear crystal. (b) Far-field image of the near-collinear down-converted light from the non-linear crystal. (c) Far-field image of the non-collinear down-converted light from the non-linear crystal. The change from non-collinear to collinear requires a very small change in tilt. 15

2.3 Diagram of a spiral phase plate with step height, h_s. 18

2.4 Generation of a forked hologram used to measure orbital angular momentum correlations. 18

2.5 A spatial light modulator encoded with an azimuthal phase dependence, $\exp(i\ell\phi)$, shapes a Gaussian beam into a helically-phased beam in the first diffraction order. This process also works in reverse such that a helical beam can be converted into a Gaussian beam. 19

2.6 Generation of an angle hologram used to measure angular position correlations. 20

2.7 (a) Schematic of an entanglement setup. The entangled photon pairs were generated by the nonlinear crystal, the combination of the spatial light modulators (SLMs) and detectors projected the photon pair into a particular state and the detection of the pairs was measured with a coincidence counter. (b) Back-projection schematic, where the nonlinear crystal is replaced with a mirror such that SLM A is imaged onto SLM B (the imaging details are given in Sec. 2.3.2). Light from a 710 nm diode laser was coupled into fibre A, where after it was imaged to SLM A followed by SLM B and then re-coupled into fibre B. 22

2.8 Experimental setup used to detect the orbital angular momentum eigenstate after spontaneous parametric down-conversion. The plane of the crystal was relay imaged onto two separate spatial light modulators (SLMs) using lenses, L_1 and L_2 ($f_1 = 200$ mm and $f_2 = 400$ mm), where the helical modes were selected. Lenses L_3 and L_4 ($f_3 = 500$ mm and $f_4 = 2$ mm) were used to relay image the SLM planes through 10 nm band-width interference filters (IF) to the inputs of the single-mode fibres (SMF). Each SMF was connected to an avalanche photo-diode (APD), which were connected to a common coincidence counter to measure the simultaneous arrival of a photon in each arm. 24

2.9 The original Einstein-Podolsky-Rosen paradox, where particles A and B move away from a source, S. A position measurement (x) on A, predicts the position of B from their relative positions and a momentum measurement (p) on A predicts the momentum of B from the conservation of momentum. 26

2.10 Experimental results showing (a) a density plot of the coincidence counts per second as a function of the azimuthal index ℓ of the holograms and (b) the non-zero diagonal elements representing a spiral bandwidth plot. The full-width-half-maximum of the spiral bandwidth is approximately 15. 27

2.11 Experimental measurements showing (a) a density plot of the coincidence counts per second as a function of the orientation of the angular holograms. The holograms on each spatial light modulator were rotated through 2π. (b) Probability distribution of the angular position ϕ_A for $\phi_B = 0$, taken along the red dotted line in (a). 28

2.12 Probability distributions for (a) the orbital angular momentum ℓ_A for $\ell_B = 0$ and (b) the angular position ϕ_A for $\phi_B = 0$. A Gaussian distribution has been fitted to both to determine the widths of each plot, which were used to demonstrate the EPR-Reid criterion. 29

2.13 The normalised coincidence counts as a function of the orientation of the holograms on each spatial light modulator (SLM). The orientation of the hologram on SLM A was fixed while those on SLM B were rotated from 0 to π. 31

2.14 Graphical representation of the (a) real and (b) imaginary parts of the two-dimensional density matrix. 35

2.15 (a) The complete set of measured probabilities for dimension 5. (b) The pure orbital angular momentum (OAM) states. (c) A sample of the superposition states. Here, θ_i denotes the phase difference in the idler arm, from Eq. (2.4.19), and θ_s denotes the same in the signal arm. The OAM states separated by a comma denote ℓ_1, ℓ_2 as in Eq. (2.4.19), while the single states denote ℓ as in Eq. (2.4.18). 37

2.16 The density matrices for even dimensions 2 through 6. The axes for dimension 2 are labelled, and the higher dimensions follow the same convention. For example, the labels for the $d = 4$ case would read $\langle 2,2|, \langle 2,1|, \langle 2,-1|, ...$ and $|-2,-2\rangle, |-2,-1\rangle, |-2,1\rangle$, etc., where we use the convention $|\ell_s, \ell_i\rangle$ to be equivalent to $|\ell\rangle_s |\ell\rangle_i$. 38

2.17 (a) Linear entropy and (b) fidelity as a function of dimension. The error for both of these measurements is ± 0.01, which is too small to be seen clearly on the graphs. In each case, the blue points represent the measured data, while the red shaded area represents the states that will not violate the appropriate high-dimensional Bell inequality. 40

3.1 Experimental setup for spontaneous parametric down-conversion. The pump is shaped by a cover slip thereby introducing a π-phase shift to half of the outputted Gaussian beam. The orbital angular momentum or angular position of signal and idler photons are measured by programming the spatial light modulator with either a forked diffraction grating or an angular slit respectively. . . . 48

3.2 Orbital angular momentum (OAM) and angular position correlations. Since the pump is in a superposition of odd OAM states, with $|1\rangle$ and $|-1\rangle$ making the largest contribution, from theory, we expect the coincidences to be high when $\ell_s + \ell_i = \pm 1$ (a). Apart from an almost uniform background (there is no background subtraction in this result), this is supported by the OAM correlations we obtain from our experiment (b). The angular position correlations also reflect the shape of the pump, and in theory can be obtained via the Fourier relationship between OAM and angular position. From the OAM correlations in (a), we expect the modulated coincidence in (c). Coincidence is high along the diagonal when $\phi_s = \phi_i$, but with minima corresponding to the position of the phase discontinuity in the pump. Apart from some background counts, our experiment results support this (d). 49

4.1 Comparison of the orbital angular momentum (OAM) spectra for the helical modes ($k_r = 0$) and Bessel-Gaussian modes ($k_r = 20, 40, 60, 80$ rad/mm) using Eqs. (4.2.14) and (4.2.13), respectively, with $\omega_0 = 0.5$ mm and $\omega_1 = 0.23$ mm. The number of usable OAM modes increases with the radial wavevector k_r. . . 56

4.2 (a) Phase pattern used to define an axicon of $k_r = 21$ rad/mm and $\ell = 1$. (b) CCD image of a Bessel-Gaussian beam generated from a blazed axicon function of $k_r = 21$ rad/mm and $\ell = 1$ at the plane of the crystal. (c) Density plot of the single count rates measured in back-projection for different blazed axicon phase patterns; varying k_r with $\ell = 0$. (d) Density plot of the single count rates measured in back-projection for a particular blazed axicon; $k_r = 21$ rad/mm and varying ℓ. 59

4.3 (a) Formation of a Bessel-Gaussian (BG) beam by directing a Gaussian beam on a standard axicon. No rings are seen in the plane of the dotted line (1) (corresponding to the plane immediately after the spatial light modulator (SLM)) as the BG beam has not yet formed. At plane (2) the interfering plane waves produce a well-defined BG beam after propagating a distance z_0. (b) Formation of a Bessel-Gaussian mode by directing a Gaussian beam on a binary axicon. A BG-like beam is observed immediately after the SLM due to the interference of the diffraction orders, $m = \pm 1$, of the binary hologram. 60

4.4 (a) Phase pattern at the plane of the spatial light modulator (SLM) to define a binary axicon of $k_r = 21$ rad/mm and $\ell = 1$. (b) Bessel-Gaussian (BG) beam formed at the plane of the mirror (crystal) by a binary axicon function of $k_r = 21$ rad/mm and $\ell = 1$ with a Gaussian input. (c) Density plot of the single count rates measured in back-projection for different binary axicon phase patterns; varying k_r with $\ell = 0$. The photons from SLM A assume a value of either positive or negative k_r from the binary function. SLM B was encoded with the same function, which allowed BG modes of either positive or negative radial wavevectors to be converted to a Gaussian mode. (d) Density plot of the single count rates measured in back-projection for a particular binary axicon; $k_r = 21$ rad/mm and varying ℓ. 61

4.5 (a) Phase pattern at the plane of the spatial light modulator to define a binary Bessel function of $k_r = 21$ rad/mm and $\ell = 1$. (b) Bessel-Gaussian beam formed at the plane of the mirror (crystal) by a binary Bessel function of $k_r = 21$ rad/mm and $\ell = 1$ with a Gaussian input. (c) Density plot of the single count rates measured in back-projection for different binary Bessel phase patterns; varying k_r with $\ell = 0$. (d) Density plot of the single count rates measured in back-projection for a particular binary Bessel function; $k_r = 21$ rad/mm and varying ℓ. 62

4.6 Experimental setup used to detect the orbital angular momentum eigenstate after spontaneous parametric down-conversion. The plane of the crystal was relay imaged onto two separate spatial light modulators (SLMs) using lenses, L_1 and L_2 ($f_1 = 200$ mm and $f_2 = 400$ mm), where the Bessel-Gaussian modes were selected. Lenses L_3 and L_4 ($f_3 = 500$ mm and $f_4 = 2$ mm) were used to relay image the SLM planes through 10 nm bandwidth interference filters (IF) to the inputs of the single-mode fibres (SMF). 63

4.7 Comparison of the measurements recorded in back-projection, (a) & (b), with those taken in down-conversion mode, (c) & (d). Density plots (a) and (c) both illustrate similar patterns for the measurements taken with $\ell = 0$ and varying k_r. The orbital angular momentum correlations are displayed in (b) & (d) for $k_r = 21$ rad/mm. 64

4.8 Graph of the measured coincidence count rate as a function of orbital angular momentum for four different measurement schemes. The Bessel-Gaussian measurements were all measured for $k_r = 21$ rad/mm. The empty orange circles represent the measurements recorded for helical modes. The blue squares represent the measurements recorded using a blazed axicon function. The binary axicon function is represented by the green triangles and the measurements from the binary Bessel function are illustrated by red circles. 65

4.9 (a) Density plot of the modal spectrum in the Bessel-Gaussian basis for k_r and ℓ. The efficiency of the coincidence count rate decreases as k_r, however the full-width-half-maximum of the bandwidth increases with k_r, seen more clearly in (b). The coloured dashed lines in (a) correspond to the profiles plotted in (b) for $k_r = 0$ rad/mm (red), $k_r = 21$ rad/mm (purple) and $k_r = 35$ rad/mm (green). 66

4.10 Effect of the radial wavevector on the Schmidt number. For $k_r = 0$, the transmission function corresponds to that of a vortex mode. An increase in the number of available orbital angular momentum modes is observed as the radial component is increased. The experimental measurements (red dots) together with a theoretical prediction (solid blue line) are plotted for $\omega_0 = 0.5$ mm and $\omega_1 = 0.23$ mm. 66

4.11 Sinusoidal behaviour of the normalised coincidence counts as a function of the angular position of the holograms, for $\ell = \pm 1$ subspace at positions $\theta_A = 0$ rad (blue), $\pi/4$ rad (pink), $\pi/2$ rad (green) and $3\pi/4$ rad (yellow). The insets show the holograms used for $\theta_A = 0$ rad and $\theta_A = \pi/4$ rad, where the phase varies from 0 (black) to π (white). 67

4.12 Results from a full quantum state tomography of a Bessel-Gaussian (BG) mode with $k_r = 21$ rad/mm. (a) & (b) Graphical representation of the real part of the density matrix for dimension $d = 2$ and $d = 5$, respectively. (c) Linear entropy and (d) fidelity as a function of dimension. The red triangles represent the measured data for the azimuthal modes, the green squares represent the measured data for the BG modes and the blue circles represent the threshold states in Eq. (13). 68

5.1 Self-healing property of Bessel-Gaussian (BG) beams. The BG beam is generated using a computer-generated hologram of an axicon (yellow triangle) and exists in a finite region, $z_{\max}$ (pink diamond). An obstacle placed in the centre of the BG region (black rectangle) obstructs the beam for a minimum distance, $z_{\min}$ (grey triangle), after which the BG field reforms. The insets display the expected image of the beam at four different planes. 74

5.2 Experimental setup. The setup shown was used to measure the effect of an obstruction in the path of the down-converted light. (a) A UV laser source pumped a type-I barium borate (BBO) crystal to produce pairs of entangled photons via spontaneous parametric down-conversion. The crystal plane was imaged onto two separate spatial light modulators (SLMs) using lenses L_1 ($f_1 =$ 200 mm) and L_2 ($f_2 = 400$ mm). Each SLM plane was again imaged to the input of a single-mode fibre using lenses L_3 ($f_3 = 500$ mm) and L_4 ($f_4 = 2$ mm). (b) Down-converted beam at the plane of the crystal. (c) A circular obstruction (radius = 200 μm) was placed between the crystal and lens L_1, in the path of the down-converted light. 75

5.3 CCD images of the crystal plane for different on-axis obstruction positions. Images for a Bessel-Gaussian (BG) mode (a-d) and a Laguerre-Gaussian (LG) mode (e-h) with azimuthal index $\ell = 2$. The unobstructed modes are shown in (a) and (e). The obstruction was first placed at the plane of the crystal, which is clearly shown in both (b) and (f). It was then moved 20 mm away from the crystal plane, shown in (c) and (g). The final images, (d) and (h), were taken 50 mm away from the crystal. It is clear the BG mode has reformed at 50 mm, while the LG mode has not resumed it's original structure. 76

5.4 Movement of the obstruction within the Bessel-Gaussian (BG) region. Consider the back-projected beam reflecting off the spatial light modulator (SLM) onto the barium borate (BBO) crystal. The Bessel hologram on the SLM creates a beam with a particular cone angle. (a) The obstruction is at the closest position to the crystal, resulting in a clear shadow region falling on the crystal. (b) The obstruction is moved away from the crystal, reducing the shadow region. (c) The obstruction is moved further away such that the shadow region no longer falls on the crystal and a recovered BG image is seen (Fig. 5.3(d)). . . . 76

5.5 Effect of an obstacle on the coincidence count rate. Measured coincidence count rates as a function of the position of the obstruction after the barium borate crystal for a Bessel-Gaussian (BG) (green squares) and Laguerre-Gaussian (LG) (purple circles) mode for $|\ell = \pm 2\rangle$ subspace. The BG mode with $k_r = 30$ rad mm^{-1} is expected to reconstruct after an obstruction with radius, $R = 200$ μm, after a distance of approximately 29 mm (yellow dashed line). The coincidence count rate remains consistently low when measured in the LG basis (purple dashed line). The count rates were averaged over a set of 10 measurements, each taken over an integration period of 5s. Errors were estimated assuming Poisson statistics for the photon counts given as a standard deviation. 77

5.6 CHSH-Bell measurements. (a) Normalised coincidence count rate as a function of the orientation of the hologram on spatial light modulator B. Hologram A was oriented at 4 different angles: 0 rad (blue curve), $\pi/8$ rad (yellow curve), $\pi/4$ rad (green curve) and $3\pi/8$ rad (red curve). The measured count rates were normalized by the denominator in equation 2.4.7. The typical sinusoidal Bell-curve was measured with the obstruction placed in the propagation path at 45 mm from the crystal. Examples of the binary Bessel holograms ($|\ell = \pm 2\rangle$) used to perform a CHSH-inequality experiment are shown in the insets (b-e). . 78

5.7 Reconstructed density matrices from full state tomography measurements. The density matrices are shown for dimensions $d = 2$ (a - c) and $d = 4$ (d - f). Real and imaginary parts of the reconstructed density matrices for (a) & (d) no obstruction, (b) & (e) obstruction placed 5 mm from the crystal and (c) & (f) obstruction placed 45 mm from the crystal. It is clear that the density matrix recovers to the original unobstructed form for a two-dimensional state as well as higher dimensional states. The density matrices were calculated by measuring an over-complete set of modes and applying a maximum likelihood estimation using a least squares fit to the measurements. This optimisation technique ensures a density matrix with non-negative eigenvalues and a trace of unity. 79

5.8 Comparison between an obstructed and attenuated beam. Measurements of the coincidence count rate, quantum contrast and concurrence of obstructed (a-c) and attenuated (d-f) entangled photons for $|\ell = \pm 2\rangle$. The obstruction was moved in 5 mm intervals along the propagation axis, at which the measurements were recorded. The dashed yellow line represents $z_{\min}$, the calculated distance at which recovery is expected (recovery is not expected within the yellow shaded region). A polariser was rotated to attenuate the coincidence count rate and vary the degree of transmission from 0 (background levels) to 1 (unattenuated and unobstructed). The coincidence count rates and quantum contrast represent the average of 10 measurements. The average error for the concurrence is ± 0.01, which is calculated by generating additional data sets by adding $\sqrt{C_i}$ fluctuations to the measured coincidence counts C_i and then repeating the concurrence calculations described in the text. The unobstructed concurrence value is represented by the blue dashed lines. 80

6.1 The Shannon mutual information I(A:B) *(green)* and the secret key rate $r_{\min}$ *(blue)* plotted as a function of the dimension. 86

List of Tables

3.1 Decomposition of the flipped-mode in terms of the $LG^{\ell p}$ modes. 47

5.1 Measured fidelity at different obstacle positions from the crystal 81

6.1 Distance scale at which entanglement decays for OAM entangled photons in a beam with $w_0 = 10$ cm, a wavelength of $\lambda = 1550$ nm, on a horizontal path in moderate turbulence ($C_n^2 = 10^{-15}$ $m^{-2/3}$). 88

List of Publications

Peer-reviewed Journal Papers:

1. Agnew, M., Leach, J., **McLaren, M.**, Roux, F.S. and Boyd, R.W.: Tomography of the quantum state of photons entangled in high dimensions. *Phys. Rev. A*, vol. 84, p. 062101, 2011.

2. Romero, J., Giovannini, D., **McLaren, M.**, Galvez, E.J., Forbes, A. and Padgett, M.J.: Orbital angular momentum correlations with a phase-flipped Gaussian mode pump beam. *J. Opt.*, vol. 14, p. 085401, 2012.

3. **McLaren, M.**, Agnew, M., Leach, J., Roux, F.S., Padgett, M.J., Boyd, R.W. and Forbes, A.: Entangled Bessel-Gaussian beams. *Opt. Express*, vol. 20, pp. 23589-23597, 2012.

4. Hamadou Ibrahim, A., Roux, F.S., **McLaren, M.**, Konrad, T. and Forbes, A.: Orbital-angular-momentum entanglement in turbulence. *Phys. Rev. A*, vol. 88, p. 012312, 2013.

5. Mafu, M., Dudley, A., Goyal, S., Giovannini, D., **McLaren, M.**, Padgett, M.J., Konrad, T., Petruccione, F., Lütkenhaus, N. and Forbes, A.: Higher-dimensional orbital-angular-momentum-based quantum key distribution with mutually unbiased bases. *Phys. Rev. A*, vol. 88, p. 032305, 2013.

6. **McLaren, M.**, Romero, J., Padgett, M.J., Roux, F.S. and Forbes, A.: Two-photon optics of Bessel-Gaussian modes. *Phys. Rev. A*, vol. 88, p. 033818, 2013.

7. **McLaren, M.**, Mhlanga, T., Padgett, M.J., Roux, F.S. and Forbes, A.: Self-healing of quantum entanglement after an obstruction. *Nat. Commun.*, vol. 5, p. 3248, 2014.

International Conference Papers:

1. Roux, F.S., **McLaren, M.**, Padgett, M.J., Forbes, A. and Konrad, T.: Down-converted bi-photons in a Bessel-Gaussian basis. *Proceedings of SPIE*, vol. 8637, p. 86370R, 2013.

2. **McLaren, M.**, Roux, F.S., and Forbes, A., Modal decomposition of Bessel-Gaussian beams. *CIOMP-OSA Summer Session*, 2013.

3. Hamadou Ibrahim, A., Roux, F.S., **McLaren, M.**, Konrad, T. and Forbes, A.: The decay of the orbital angular momentum entanglement in turbulence. *OSA Frontiers in Optics*, paper FW4D 2013.

4. **McLaren, M.**, Romero, J., Mhlanga, T., Roux, F.S., Padgett, M.J. and Forbes, A.: Recovery of quantum-entanglement after encountering an obstruction. *Proceedings of SPIE*, To be published, 2014.

5. Dudley, A., Mafu, M., Goyal, S., Giovannini, D., **McLaren, M.**, Padgett, M.J., Konrad, T., Petruccione, F., Lütkenhaus, N. and Forbes, A.: Encoding mutually unbiased bases in orbital angular momentum for quantum key distribution. *Proceedings of SPIE*, To be published, 2014.

6. Hamadou Ibrahim, A., Roux, F.S., Goyal, S.K., **McLaren, M.**, Konrad, T. and Forbes, A.: The evolution of OAM-entanglement between two qutrits in turbulence. *Proceedings of SPIE*, To be published, 2014.

National Conference Papers:

1. **McLaren, M.,**, Roux, F.S., and Forbes, A.: Comparison of phase-dependent only and complete Laguerre-Gaussian beams using modal decomposition. *56th Annual Conference of the South African Institute of Physics*, 2011.

2. **McLaren, M.,**, Roux, F.S., and Forbes, A.: High-dimensional entanglement, *57th Annual Conference of the South African Institute of Physics*, 2012.

3. **McLaren, M.**, Agnew, M., Leach, J., Roux, F.S., Padgett, M.J., Boyd, R.W. and Forbes, A.: Entangled Bessel-Gauss beams. *Quantum Africa II*, 2012.

4. Romero, J., Giovannini, D., **McLaren, M.**, Galvez, E.J., Franke-Arnold, S., Forbes, A., Barnett, S.M. and Padgett, M.J.: Orbital angular momentum and angular position correlations of entangled photons. *Quantum Africa II*, 2012.

5. **McLaren, M.**, Roux, F.S., and Forbes, A.: Quantum entanglement. *IONS Africa*, 2012.

6. **McLaren, M.**, Romero, J., Giovannini, D., Galvez, E.J., Padgett, M.J. and Forbes, A.: Quantum entanglement with a Hermite-Gaussian pump, *58th Annual Conference of the South African Institute of Physics*, 2013.

7. **McLaren, M.**, Roux, F.S., and Forbes, A.: Bessel-Gaussian entanglement. *58th Annual Conference of the South African Institute of Physics*, 2013.

8. Dudley, A., Mafu, M., Goyal S., Giovannini, D., **McLaren, M.**, Padgett, M.J., Konrad, T., Petruccione, F., Lütkenhaus, N. and Forbes, A.: Encoding mutually unbiased bases in orbital angular momentum for quantum key distribution. *58th Annual Conference of the South African Institute of Physics*, 2013.

9. **McLaren, M.**, Hamadou Ibrahim, A., Roux, F.S. and Forbes, A.: Is long distance free-space quantum communication with the OAM state of light feasible? *58th Annual Conference of the South African Institute of Physics*, 2013.

10. Mhlanga, T., **McLaren, M.**, Roux, F.S., and Forbes, A., Modal decomposition of Bessel-Gaussian beams, *58th Annual Conference of the South African Institute of Physics*, 2013.

Nomenclature

List of symbols

$h =$	6.626×10^{-34}	[m^2kg/s]
$e =$	2.718	
$\pi =$	3.142	
λ	Wavelength	[m]
k	Radial wavenumber	[m^-1]
ℓ	Azimuthal mode index	[ ]
ϕ	Azimuthal angle	[rad]
θ	Spherical co-ordinate	[rad]
p	Radial mode index	[ ]
$w(0)$	Gaussian beam waist	[m]
z_R	Rayleigh range	[m]
$L_p^{\|\ell\|}$	Laguerre polynomial	[ ]
ρ	Density matrix	[ ]
ω	Frequency	[Hz]
L	Crystal length	[m]
n	Refractive index	[ ]
f	Focal length	[m]
h_s	Step height	[m]

θ	Spherical co-ordinate	[rad]
$\mathbf{k}$	Radial wavevector	[rad.m^{-}1]

Acronyms/Abbreviations

OAM	Orbital angular momentum
EPR	Einstein-Podolsky-Rosen
CHSH	Clauser-Horne-Shimony-Holt
SPDC	Spontaneous parametric down-conversion
SAM	Spin angular momentum
LG	Laguerre-Gaussian
BG	Bessel-Gaussian
HG	Hermite-Gaussian
FWHM	Full-width-half-maximum
SLM	Spatial light modulator
LCD	Liquid crystal display
SMF	Single-mode fibre
APD	Avalanche photo-diode
BBO	Barium borate
IF	Interference filter
CCD	Charge-coupled device
MUB	Mutually unbiased basis
QKD	Quantum key distribution

Chapter 1

Introduction

One of the most astonishing features of quantum mechanics is that of the entanglement of particles. A great deal of work investigating the properties of entanglement of two photons has been performed, initially focused on two-dimensional entanglement of polarisation. However, high-dimensional entanglement is of greater interest to most quantum information processes and thus the infinite-dimensional orbital angular momentum (OAM) has become the preferred basis in which to measure entanglement. In this chapter, we introduce the concept of quantum entanglement by highlighting its origins, development and the current state of OAM entanglement. We focus particularly on entanglement in the OAM basis, briefly discussing existing studies and central issues encountered in the field.

1.1 History

First introduced as an objection to quantum mechanics by the famous Einstein, Podolsky and Rosen (EPR) thought experiment [1], entanglement represents the notion of non-local quantum correlations between two or more quantum-mechanical systems. That is, for an entangled pair of particles the measurement of an observable for one particle immediately determines the corresponding value for the other particle, regardless of the distance between the two particles. This property of entangled systems led to a number of implications that disturbed many scientists and resulted in the emergence of hidden variable theories, of which Einstein was a strong proponent. Local hidden variable theory assumes that nature can be described by local processes, where information and correlations propagate at most at the speed of light and where the observables of a physical system are determined by some unknown (hidden) variables.

It was not until the 1960s, when Bell's inequality and its generalization, Clauser-Horne-Shimony-Holt (CHSH) Bell's inequality [2], demonstrated the possibility of practical experiments to test the validity of quantum theory with respect to local hidden variable theories. A slew of experiments followed to test Bell's inequality, each of which violated the inequality and in turn verified quantum mechanical predictions of entanglement [3; 4; 5; 6]. These results encouraged the search for a method of producing maximally entangled states. Spontaneous parametric down-conversion (SPDC) has proved to be the most efficient technique in generating two-particle entanglement. Shih and Alley were the first to demonstrate a violation of Bell's inequality using SPDC generated photon pairs [7].Two-dimensional polarisation entanglement has been employed for quantum cryptography [8].

This was the start of various polarisation-entanglement experiments, however, in 2001 it was shown that orbital angular momentum (OAM) could not only be used as a basis for entanglement but more importantly provided an advantage over polarisation with regard to the number of states available [9]. Spatial modes possessing OAM have been studied often in recent years because of the infinite-dimensional alphabets they can possibly provide. In particular, the OAM modes of a photon are a very good avenue for exploring higher dimensions [10]. Quantum mechanics in higher dimensional systems has the potential of revolutionising quantum communication and computation protocols. As an example, quantum cryptography using qu*d*its (systems in which there are d orthogonal states) has been

shown to be more secure and robust in the presence of noise [11; 12; 13].

OAM is steadily being considered as a quantum resource for entanglement concentration [14], quantum coin tossing [15] and (when coupled with spin) quantum teleportation protocols [16; 17; 18]. The potential of OAM entanglement is enormous, however a number of related issues need to be understood and solved before we can take full advantage of these spatial modes.

1.2 Angular momentum of light

Maxwell's equations in the early 1860s demonstrated that electromagnetic waves travelled at the speed of light and consequently showed that light must be a manifestation of the electromagnetic field [19]. Building upon that work, the mechanical effects of light were highlighted in the form of radiation pressure or linear momentum [20]. We now know that light carries a linear momentum of $\hbar\mathbf{k}$ per photon, where $\hbar = h/2\pi$ and the wavenumber $k = 2\pi/\lambda$ for the wavelength λ and Planck's constant h. However, light also carries angular momentum, which is simply related to linear momentum by $\mathbf{L} = \mathbf{r} \times \mathbf{p}$, with the particle's position from the origin given by $\mathbf{r}$ and its linear momentum by $\mathbf{p} = m\mathbf{v}$. In the paraxial approximation, the angular momentum of light can be separated into two independent components: spin angular momentum (SAM) and orbital angular momentum (OAM).

1.2.1 Spin-angular momentum

Angular momentum associated with circularly polarised light is known as spin angular momentum and is quantified by $\pm\hbar$ per photon. The more well-known of the two angular momenta, SAM was first acknowledged by Poynting [21] in 1909 who assumed that circularly polarised light, when passed through a quarter waveplate, would exert a torque on the plate causing it to rotate. This concept was experimentally realised in 1936 when Beth [22] used polarised light to rotate a suspended birefringent waveplatet.

The direction of the electric field oscillation of light as it propagates, specifies the type of polarisation. For linearly polarised light, the field oscillates in a single plane, whereas the field rotates about the propagation axis for circularly polarised light. Figure 1.1(a) illustrates the oscillations of linear and circular polarised fields. The direction of the rotation specifies

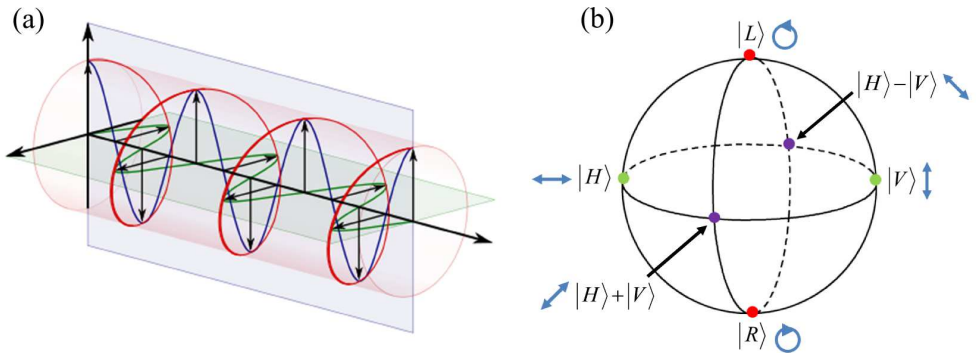

Figure 1.1: (a) The superposition of the electric fields of two linearly polarised fields, $\pi/2$ out of phase, produce circularly polarised light. (b) The Poincaré sphere can be used to represent any polarisation state, where $|H\rangle$ and $|V\rangle$ represent horizontally and vertically polarised light, respectively, and $|L\rangle$ and $|R\rangle$ represent left and right circularly polarised light, respectively.

the handedness of the circular polarisation; clockwise specifies right-handed, anti-clockwise specifies left-handed circularly polarised light. Any polarisation state can be represented in a convenient graphical manner using the Poincaré sphere, shown in Fig. 1.1(b).

According to this representation, the two circularly polarised states lie at the north (right-handed) and south (left-handed) poles. Linearly polarised states lie on the equator, while the states which lie between the poles and equator represent elliptical polarisation. The circular polarisation states can be written as superpositions of linear states and vica versa. More generally, any state on the Poincaré sphere can be written as a superposition of two other states on the sphere.

1.2.2 Orbital Angular Momentum

The other component of angular momentum has only recently been exploited experimentally. In 1992, Allen [23] demonstrated that beams with helical phase fronts result in an azimuthal component to the Poynting vector (gives the direction and magnitude of momentum flow), which produces OAM parallel to the beam axis. The momentum circulates around the beam axis, while along the beam axis the phase is undefined and known as a phase singularity, which results in destructive interference and zero intensity at that centre point. Helically phased beams possess an azimuthal phase dependence of $\exp(i\ell\phi)$, where the azimuthal phase index ℓ represents the number of azimuthal phase rotations in one full cycle from 0 to 2π and ϕ is the angular coordinate. Figure 1.2 illustrates the difference in the phase of a beam carrying OAM and one without. Interestingly, like SAM, the OAM

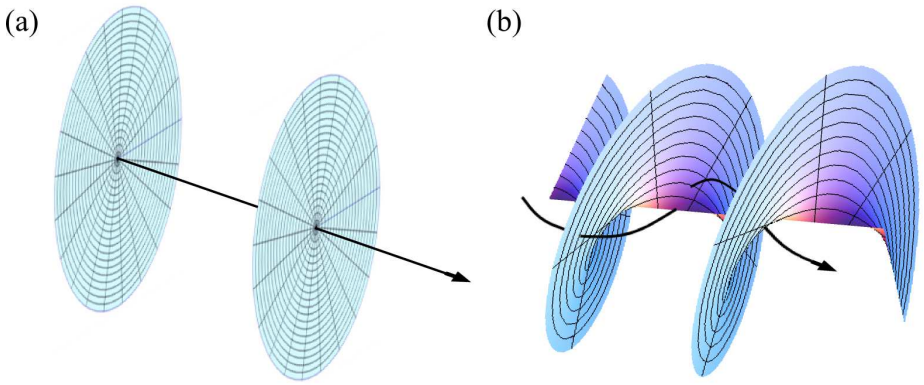

Figure 1.2: (a) A Gaussian beam with planar phasefronts does not carry orbital angular momentum (OAM). (b) A beam with helical phasefronts will carry OAM, the amount of which is specified by the azimuthal index ℓ.

of helically phased beams is in units of $\hbar$; that is $\ell\hbar$ per photon, where ℓ is any positive or negative integer.

An analogy between polarisation and OAM can be made using the Poincaré sphere and its equivalent, the Bloch sphere [24] shown in Fig. 1.3. Any OAM state can be represented on the surface of an equivalent sphere, known as the Bloch sphere. The north and south poles of the sphere represent the states $|\ell\rangle$ and $|-\ell\rangle$ (using Dirac notation), while the points around the equator, $\theta = \pi/2$, represent the superposition states. Any vector $|q\rangle$ on the sphere can be described using the spherical co-ordinates θ and ϕ by

$$|q\rangle = \cos\left(\frac{\theta}{2}\right)|\ell\rangle + \exp(i\phi)\sin\left(\frac{\theta}{2}\right)|-\ell\rangle\,. \tag{1.2.1}$$

The rotation of a particle from transferred polarisation shown by Beth can also be generated from OAM. In 1995, it was shown that by directing an OAM carrying beam onto graphite particles they would rotate [25]. Instead of passing light through the particle, as with polarisation, the graphite particles absorbed the light and its OAM. While SAM causes the particle to rotate on its own axis, OAM causes the particle to orbit around the beam axis. This property has been used in optical tweezers to manipulate and rotate mircomachines for the use in microfluidics [26].

A common example of helically phased beams is the Laguerre-Gaussian (LG) modes

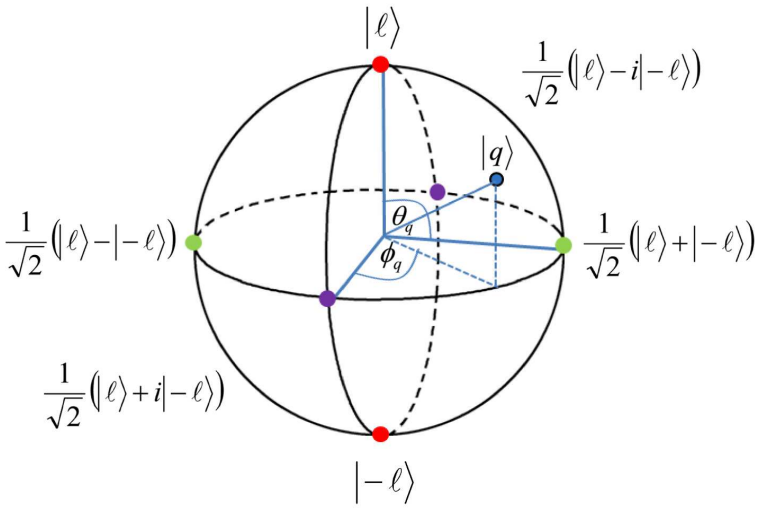

Figure 1.3: Bloch sphere diagram used to describe any orbital angular momentum state with azimuthal index ℓ.

[27], a complete basis set of orthonormal modes:

$$\begin{aligned} \mathrm{LG}_{pl} &= \sqrt{\frac{2p!}{\pi(p+|\ell|)!}}\frac{1}{w(z)}\left[\frac{r\sqrt{2}}{w(z)}\right]\exp\left[\frac{-r^2}{w^2(z)}\right]L_p^{|\ell|}\left(\frac{2r^2}{w^2(z)}\right)\exp[i\ell\phi] \\ &\quad\times\exp\left[\frac{ik_0r^2z}{2(z^2+z_R^2)}\right]\exp\left[-i(2p+|\ell|+1)\arctan\left(\frac{z}{z_R}\right)\right]. \end{aligned} \tag{1.2.2}$$

where ℓ and p are the azimuthal and radial mode indices, respectively. The $1/e$ radius of the Gaussian term is given by $w(z) = w(0)\left[\left(z^2+z_R^2\right)/z_R^2\right]^{1/2}$ with the beam waist $w(0)$, z_R is the Rayleigh range, $\arctan(z/z_R)$ is the Guoy phase and $L_p^{|\ell|}(x)$ represents a Laguerre polynomial. The intensity distribution of an LG mode with $\ell > 0$, consists of a zero on-axis intensity surrounded by $p+1$ concentric rings. The radius of maximum intensity for such modes is proportional to $\sqrt{\ell}$ for $p = 0$. Figure 1.4 illustrates a set of LG modes.

LG beams can be generated experimentally using a computer-generated hologram. By considering only the azimuthal phase term of Eq. (1.2.2), a good approximation to an LG beam can be created, which we refer to as a helical beam. These helical modes are commonly used in experiments and will be used throughout this thesis, unless otherwise stated.

OAM is not a unique property to LG beams and is found in both higher-order Bessel-Gaussian (BG) beams [28] and Ince-Gaussian beams [29]. These modes can also be generated using specific holograms, allowing OAM entanglement to be studied using modes other than those in the LG basis.

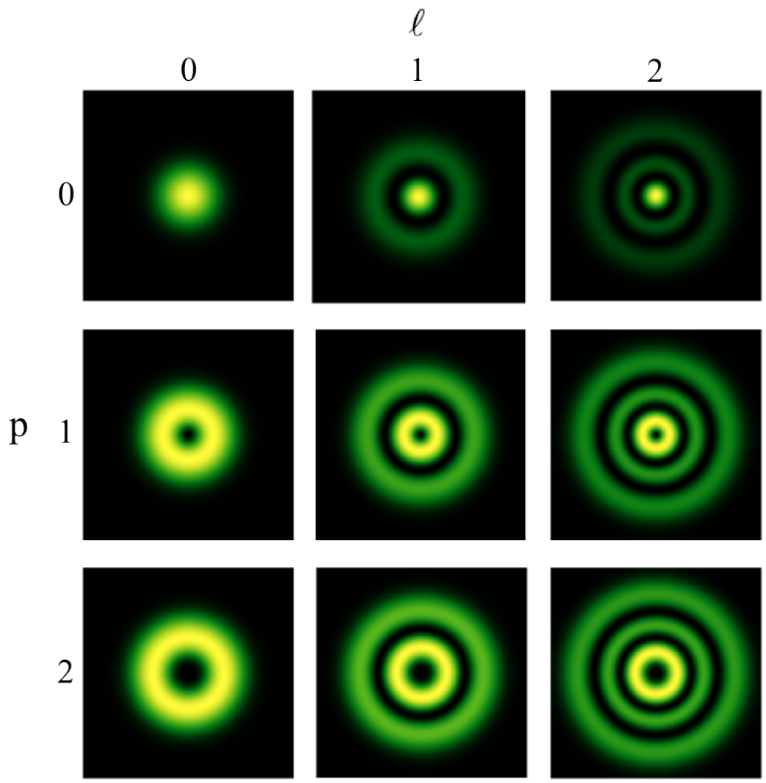

Figure 1.4: Laguerre-Gaussian modes have both a radial p and an azimuthal ℓ component.

1.2.3 Angular position and OAM

The conjugate variable of OAM is angular position [30; 31] and the Fourier relationship between them can be written as

$$A_\ell = \frac{1}{\sqrt{2\pi}} \int_{-\pi}^{\pi} \Psi(\phi) \exp(-i\ell\phi) d\phi, \tag{1.2.3}$$

$$\Psi(\phi) = \frac{1}{\sqrt{2\pi}} \sum_{\ell=-\infty}^{\infty} A_\ell \exp(i\ell\phi), \tag{1.2.4}$$

where A_ℓ are the amplitudes of the OAM states and $\Psi(\phi)$ is the azimuthal dependence of the corresponding complex beam amplitude [32].

Although an analogy between the linear and angular position-momentum Fourier relationships can be made, there are important differences. Firstly, the position, $\mathbf{x}$, and momentum, $\mathbf{p}$, variables are continuous and range from $-\infty$ to ∞. An angular function, $\Psi(\phi)$ is continuous, but is also 2π cyclic. This 2π periodicity has led to discussion over whether or not angle can be an observable in quantum mechanics (a periodic function has an ill-defined standard deviation). For our purposes it is sufficient to bound the function within

the region $\pm\pi$. The periodic nature of angle is the reason that the OAM eigenstates ℓ are a discrete series of integers. Although light can have a fractional net OAM, it can always be expressed in terms of the integer OAM eigenstates. In 2008, Jha *et al.* demonstrated that the Fourier relationship between angle and OAM was not only valid for classical light but also for entangled photon pairs [33].

1.3 Entangled photon states

An entangled state can be simply viewed as two states which are inseparable. If we consider two subsystems A and B of a pure state $|\psi\rangle$, then the state can be written as

$$|\psi\rangle = |i\rangle_A |j\rangle_B , \tag{1.3.1}$$

where $\{|i\rangle\}$ and $\{|j\rangle\}$ are orthonormal bases of A and B, respectively. This state is not entangled; it is merely a product of the two systems, allowing the properties of each system to be separated. A superposition state of the form of Eq. (1.3.1) is given as,

$$|\psi\rangle = \sum_{i,j} c_{ij} |i\rangle_A |j\rangle_B . \tag{1.3.2}$$

Here c_{ij} represents the expansion coefficients and $\sum_{i,j} \left|c_{i,j}\right|^2 = 1$. This formalism is known as the Schmidt decomposition. The Schmidt basis depends on the quantum state and must be calculated in each case. If the state cannot be separated into a product of the two systems A and B, it is entangled. For example, the following superposition state is entangled:

$$|\psi\rangle = \frac{1}{\sqrt{2}} \left(|i\rangle_A |j\rangle_B \pm |j\rangle_A |i\rangle_B\right). \tag{1.3.3}$$

Both Eq. (1.3.2) and (1.3.3) represent a two-photon state, where each photon can carry bits of information, the number of which depends on the basis used.

When states lose phase coherence between the bases, they also lose their degree of entanglement. The degree of entanglement of any quantum system can be characterised by calculating the two-photon density matrix:

$$\rho = |\psi\rangle \langle\psi| . \tag{1.3.4}$$

In order for this matrix to be physically allowed, it must have positive eigenvalues and a trace equal to unity. Eq. (1.3.4) is only true for pure quantum states. Quantum systems

including mixed states use a more general density matrix:

$$\rho = \sum_n p_n |\psi_n\rangle \langle\psi_n| , \tag{1.3.5}$$

where p_n is the probability that the system is in state $|\psi_n\rangle$. The density matrix allows various measurements to be calculated, which describe the quantum state, such as linear entropy, fidelity and concurrence. These will be defined in Sec. 2.4.3.

The amount of information carried per photon is dependent on the basis in which the quantum state is measured. A qubit system can carry at most only two bits of information per photon. For example, polarisation entangled photons consist of two states, horizontal ($|H\rangle$) or vertical ($|V\rangle$), and the superpositions thereof. The polarisation basis is therefore an example of an entangled two-photon qubit state, written as

$$|\psi\rangle = \frac{1}{\sqrt{2}} \left(|H\rangle_A |V\rangle_B \pm |V\rangle_A |H\rangle_B \right) . \tag{1.3.6}$$

Early studies of entangled states of light focused on polarisation-based experiments. In particular, Aspect *et al.* demonstrated an effective method in which to violate Bell's inequality and thus discounting local hidden-variable theories [5; 6]. The first quantum teleportation experiment was also achieved using polarisation entangled photons [17].

Despite the success of the polarisation states, a need for increased information capacity per photon resulted in a search for a qu*d*it system, where d bits of information could be carried per photon. This progression naturally led to investigations into entanglement in the OAM basis, where high-dimensional entanglement was not only possible but achievable too. Although these orthogonal modes have a clear advantage over polarisation, they also introduce new experimental challenges, which we aim to investigate in this work.

1.4 Entangled states of OAM

The simplest method of generating entangled photons is via SPDC, where a single photon incident on a non-linear crystal produces two photons of half the original wavelength, which are entangled. Historically, the two entangled photons have been given the names signal and idler. These down-converted photons also possess the property of OAM and the seminal paper by Mair *et al.* [9] was the first experiment to demonstrate conservation of OAM in the down-conversion process. They consequently showed entanglement involving these

modes. That is, the OAM of the entangled photon pair must sum to the OAM of the pump:

$$m = \ell_s + \ell_i. \tag{1.4.1}$$

Here m is the OAM carried by the pump photon and $\ell_{s,i}$ is the OAM of the signal and idler photons, respectively. The Schmidt decomposition [34] for the OAM states can be represented using the LG basis. The two-photon state can then be written as:

$$|\psi\rangle = \sum_{p_{s,i}=0}^{\infty} \sum_{\ell=-\infty}^{\infty} c_{\ell}^{p_{s,i}} |\ell, p_s\rangle |m-\ell, p_i\rangle , \tag{1.4.2}$$

where $|c_{\ell}^{p_{s,i}}|^2$ is the probability of finding one photon in state $|\ell, p_s\rangle$ and the other in state $|m-\ell, p_i\rangle$. Most experiments focus on the azimuthal component of the LG modes as it is typically easier to measure than the radial component. Thus, we ignore the radial components of the LG basis and write the two-photon state for OAM as

$$|\psi\rangle = \sum_{\ell} c_{\ell} |\ell\rangle |m-\ell\rangle , \tag{1.4.3}$$

where $|c_{\ell}|^2$ is the probability of finding one photon in state $|\ell\rangle$ and the other in state $|m-\ell\rangle$. As ℓ can assume any integer value, OAM entanglement represents a qu*d*it system where, in principle, each photon can carry an infinite amount of information.

OAM entanglement became a priority for many groups due to its potential for increased information capacity per photon. A violation of Bell's inequality is a significant experiment in which to test for quantum correlations. Polarisation-entangled photons had already demonstrated such a violation [5; 35]. By using the analogy between polarisation and OAM from the Bloch sphere, Leach *et al.* [36] succeeded in violating a CHSH-Bell inequality for different OAM subspaces (the details of which are discussed in Chap. 2). This violation distinguishes quantum correlations from classical correlations.

Determining the degree of entanglement of a quantum state is crucial for quantum applications such as quantum communication. Thus, upon discounting the hidden-variable theory, the density matrix of the state was reconstructed using a method of full state tomography to allow full characterisation of the quantum state [37]. Although performed in the OAM basis, these results were obtained for a two-photon qubit system and had not yet quantified high-dimensional entangled systems.

Yet the advantage in measuring entanglement in the OAM basis is the access to more than two states, which is the limiting factor in the polarisation basis. In 2011, high-

dimensional entanglement was demonstrated through violations of Bell-type inequalities up to dimension $d = 12$ [10]. This was an important step in realising quantum information protocols such as teleportation [16] and quantum key distribution protocols [38]. High-dimensional entanglement requires access to higher-order OAM modes. Theoretically, these modes are attainable, however there are many experimental elements which have a considerable effect on the number of accessible OAM modes. These include both the length [39] and orientation [40; 41] of the non-linear crystal, as well as the mode sizes of the pump, signal and idler photons [42].

While the success of OAM entanglement is evident, the measurements thus far have only used helical modes (phase-only approximation to the LG modes). However, it has been shown that the inclusion of the radial modes has a significant effect on the number of accessible OAM modes [43]. The challenge in including the radial modes lies in the hologram required to measure the OAM states. There are no devices that allow the control of amplitude and phase of light, resulting in clever manipulation of phase-only devices to vary amplitude as well [44]. The diffraction efficiency is drastically reduced when using these phase-amplitude holograms, which can be an issue when recording measurements at the single photon level.

Additionally, the feasibility of quantum communication relies on the ability of OAM entangled states to propagate in free-space. Polarisation modes can be propagated over a distance using fibres [45]. Presently, however, fibres do not support the propagation of OAM modes, leaving the alternative option of free-space propagation. However, OAM modes suffer distortion due to the scintillation process while propagating through a turbulent medium [46]. There has therefore been a great deal of work both theoretically [47; 48; 49] and experimentally [50; 51; 52] in understanding the effects of turbulence on OAM entanglement. Typically, these effects are examined for weak turbulence [47; 50], while the predictions of strong turbulence are somewhat more challenging to investigate [53].

1.5 Outline

This thesis is structured as follows. In Chapter 2 we discuss how the OAM-entangled photon pairs are generated via SPDC and describe in detail the experimental setup used to measure and characterise OAM entanglement. We use the experimental setup to perform a

demonstration of an EPR-type paradox and test local hidden-variable theories by showing a violation of a Bell-type inequality. We also investigate high-dimensional entanglement and describe a method in which to characterise the qu*d*it systems using state tomography.

Chapter 3 introduces a manner in which to engineer our entangled system by looking at the effect of the pump mode on the OAM-entangled photon pair. By using a simple technique to shape the pump mode, we investigate the effect of a phase-flipped Gaussian mode, which can be approximated as a Hermite-Gaussian (HG) beam. We look at the measurements made in the OAM basis as well as its conjugate variable, angular position.

Chapter 4 tackles the challenge of increasing the number of accessible OAM modes by changing the measurement basis from LG to BG modes. We describe the two-photon optics of BG entanglement by studying three different methods in which to measure OAM entanglement in the BG basis. We show that the quantum correlations in each method can be accurately predicted using a classical light source. By choosing one particular method, we show that the number of accessible OAM modes can be increased in the BG basis. We extend this concept by characterising our BG entanglement using full state tomography. We show that the increase in accessible OAM modes directly results in the ability to entangle in higher dimensions when compared with the LG basis, thereby increasing the potential for many quantum information processes.

In chapter 5, we introduce a perturbation to our BG entanglement system by placing an obstacle in the propagation path. We use the self-healing property of BG modes to recover the measured entanglement after the obstacle.

Finally,we conclude my thesis by summarising the contributions we have made to the field of OAM entanglement and discussing our future work within this field.

Chapter 2

Experimental methods and apparatus

The spatial orbital angular momentum (OAM) modes of entangled photon pairs are investigated in light of their potential for high-dimensional entanglement. We thoroughly examine the methods used to generate, measure and characterise entangled OAM states by performing the first entanglement experiment in South Africa. We highlight the experimental challenges contained within each step and provide practical techniques for future experiments in the quantum regime.

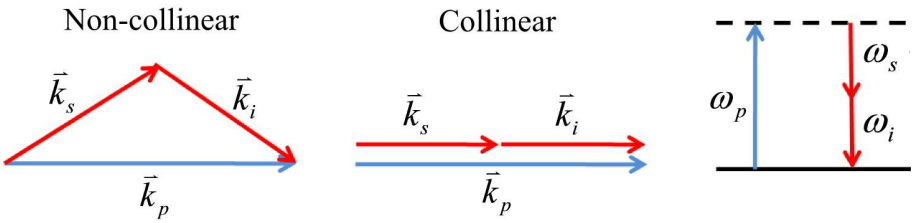

Figure 2.1: Conservation of momentum and energy in the process of parametric down-conversion, where **k** and ω are the wavevectors and frequencies of the respective photons.

2.1 Spontaneous Parametric Down-conversion

The most commonly used and most efficient method of producing entangled photon pairs is that of spontaneous parametric down conversion (SPDC). First introduced as parametric noise or fluorescence [54; 55], this non-linear optical process decays a pump photon into two photons (signal and idler) in a crystal of optical non-linearity, χ^2. Both energy and momentum are conserved in this decay process (see Fig. 2.1), also known as the phase matching conditions:

$$\omega_p = \omega_s + \omega_i, \tag{2.1.1}$$

and

$$\mathbf{k}_p = \mathbf{k}_s + \mathbf{k}_i. \tag{2.1.2}$$

Here, $\omega_p, \omega_s, \omega_i$ and $\mathbf{k}_p, \mathbf{k}_s, \mathbf{k}_i$ are the frequencies and wavevectors of the pump, signal and idler photon, respectively. Due to these conditions, the measurement of one photon in a particular direction and energy, forces the existence of the other correlated photon of definite energy and direction.

Initially, SPDC was not used as a source for entanglement measurements. However, Burnham and Weinberg [56] noted the simultaneous arrival of photon pairs at separate detectors (referred to as a coincidence count), thereby verifying the quantum mechanical description of SPDC. Nonetheless, entanglement experiments continued to use photons generated from cascade atomic decays using calcium [3; 5; 6; 57] and mercury [4; 58] atoms. This method of generation was problematic in that the entangled photons were randomly emitted over a full solid angle, causing the collection of the entangled photons to be very difficult. The time of emission of the photons was also unknown in such schemes. The phase matching conditions of SPDC forced the generation of photon pairs in specific directions within a narrow cone of light. Shih and Alley were the first to use SPDC to demonstrate

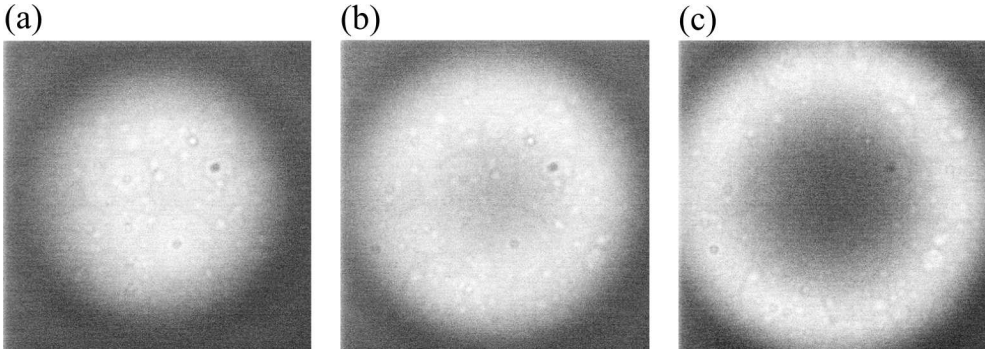

Figure 2.2: SPDC is the most efficient method for producing entangled photons, however, the probability of a spontaneous decay into a pair of entangled photons is very low. Therefore a very sensitive electron multiplier CCD camera is needed to image the ring of photons. (a) Far-field image of the collinear down-converted light from the non-linear crystal. (b) Far-field image of the near-collinear down-converted light from the non-linear crystal. (c) Far-field image of the non-collinear down-converted light from the non-linear crystal. The change from non-collinear to collinear requires a very small change in tilt.

polarisation entanglement in 1988, where they observed EPR type correlations and demonstrated a violation of Bell's inequality [7]. Entangled photon generation via SPDC has since been used to measure additional properties such as phase [59], time and energy [60], linear momentum and position [61] and in particular the orbital angular momentum (OAM) modes of photons [36]. Throughout this thesis we examine only OAM entangled photons generated from SPDC.

2.1.1 SPDC characterisation

There are two types of SPDC, namely type I and type II. In type I, the down-converted photons are produced with the same polarisation, orthogonal to that of the pump. Photons of the same wavelength are emitted on concentric cones centred around the pump axis of propagation. The diameter of the cone depends on the angle between the pump beam and the optical axis of the crystal. Type II SPDC emits one photon with the same polarisation as the pump and the other with orthogonal polarisation. In both cases, the process is said to be degenerate if the down-converted photon pair have the same wavelength (i.e. $\lambda_i = \lambda_s = 2\lambda_p$) and non-degenerate otherwise. We use type I, degenerate down-conversion for all our experiments presented in this thesis.

SPDC can be further characterised into collinear and non-collinear processes, depending on the position of the optic axis relative to the pump, shown in Fig. 2.2. By simply

changing the tilt of the crystal, a phase mismatch occurs causing the opening angle of SPDC to change, moving from non-collinear to collinear down-conversion, allowing an optimal position to be found depending on the application [40]. Romero *et al.* found that even small variations to the angular orientation of the crystal of approximately 1/20 of a degree can affect the number of usable OAM modes detected [41]. The intensity profile of the far-field down-converted light follows the function:

$$I(r) = \mathrm{sinc}^2\left(\frac{ar^2}{f^2} + \alpha\right), \tag{2.1.3}$$

where f is the focal length of the Fourier lens with radial coordinate r. The phase-matching parameter establishes the opening angle of SPDC and is given by $\alpha = (|\mathbf{k}_p| - |\mathbf{k}_s| - |\mathbf{k}_i|)\,L/2$, and $a = (|\mathbf{k}_s| + |\mathbf{k}_i|)\,L/4n^2$, for refractive index n and crystal length L [41]. The propagation of light through an optical system can be described by étendue, which when normalised to the wavelength λ, gives an estimate of the number of detectable transverse modes, written as [62]

$$N = \frac{A\Omega}{\lambda^2}. \tag{2.1.4}$$

Here, A is the area of the near-field beam and Ω is the far-field opening angle. By choosing to measure OAM entanglement in the near-field, A is effectively constant. Thus, as α is changed from collinear to near-collinear, the opening angle Ω increases, yielding a larger number of usable OAM modes. Our early experiments were performed for non-collinear down-conversion, however following the work by Romero *et al.* [41], we altered our setup to near-collinear down-conversion to increase the number of usable OAM modes measured.

2.1.2 Spiral Bandwidth

The quantum spiral bandwidth was first coined by Torres *et al.* in 2003 and refers to the number of OAM modes [39]. A large spiral bandwidth is important for quantum information processes where high information capacity per photon is required [12; 63; 64]. We can describe this term further by defining the number of OAM modes generated in SPDC as the *generation* spiral bandwidth, which is dependent on both the size of the pump beam and the length of the non-linear crystal [39; 65]. An increase in the pump beam size or a decrease in the thickness of the crystal produces a wider spiral bandwidth [42]. The radial intensity distribution of helical modes increases with $\sqrt{\ell}$, thus the size of the pump waist determines

the highest OAM mode achievable. Thus a larger pump waist is favourable over a tightly focused spot. The phase matching conditions of SPDC can also be manipulated to produce a larger spiral bandwidth [40; 41] An analytical description of the complete OAM spectrum as generated by SPDC was calculated from the measured visibility in a Hong-Ou-Mandel type interferometer [40]. This experiment demonstrated for the first time that the full generated bandwidth could be measured without experiencing effects from the measurement and detection apparatus.

This leads us to the number of OAM modes that can be physically measured, known as the *measurement* spiral bandwidth. Both the generation spiral bandwidth and the efficiency of the detection scheme affect the final measurement bandwidth. Typically, holograms or phase plates are used in conjunction with single-mode fibres to perform projective measurements of OAM. These measurements are sensitive to the radial field distribution [62; 65; 66], resulting in a different spiral bandwidth than that initially generated. Law and Eberly [34] used the Schmidt decomposition technique, which completely characterised entanglement [67], to provide an estimate of the measured OAM bandwidth by computing the azimuthal Schmidt number given by

$$K_{az} = \frac{1}{\sum_\ell P_\ell^2}, \tag{2.1.5}$$

where $P_\ell = |c_\ell|^2$ is the probability of measuring a particular OAM state [40]. The total Schmidt number, K, is related to the azimuthal Schmidt number by $K_{az} = 2\sqrt{K}$ [68]. The full-width at half maximum (FWHM) value is often used as a measure of bandwidth, however, it is not the equivalent of the Schmidt number.

2.2 OAM generation and measurement

A spiral phase plate is an optical element with a helical surface that can be used to generate beams carrying OAM [69]. The transparent plate with refractive index, n, has a phase dislocation with step height, h_s, shown in Fig. 2.3. A Gaussian beam with a planar wavefront incident on the plate will gain OAM of $\ell = h_s(n-1)/\lambda$, where λ is the wavelength of the incident beam. This technique nicely demonstrates how a planar wavefront is converted into a helical wavefront.

These elements can be described using a digital hologram encoded onto a spatial light

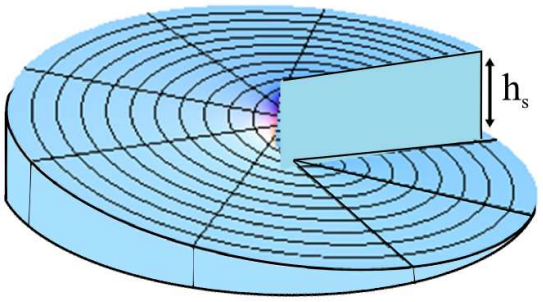

Figure 2.3: Diagram of a spiral phase plate with step height, h_s.

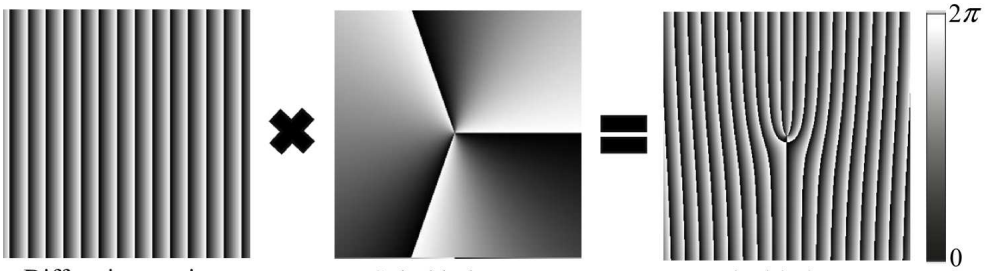

Figure 2.4: Generation of a forked hologram used to measure orbital angular momentum correlations.

modulator (SLM), which enables the phase of an incoming beam to be shaped according to the encoded hologram. An SLM consists of a liquid crystal display (LCD) made up of a number of pixels, each of which is addressed by two electrodes such that the molecules making up the pixels are aligned parallel to the electrodes. By applying an electric field to the electrodes, the molecules tilt in the direction of the field. This tilt changes the refractive index seen by the light and in turn changes the phase of the incident light beam. An SLM connects to a computer such that the computer generated holograms are then displayed on the LCD screen. This allows us to change the displayed hologram quickly and easily without re-alignment. The phase function used to describe a spiral phase plate is give as

$$T(\phi) = \exp(i\ell\phi), \tag{2.2.1}$$

where ϕ is the azimuthal angle. The azimuthal index ℓ is easily varied, allowing helical beams carrying different amounts of OAM to be generated.

As SLMs are diffractive optical elements, the field reflected from the LCD will consist

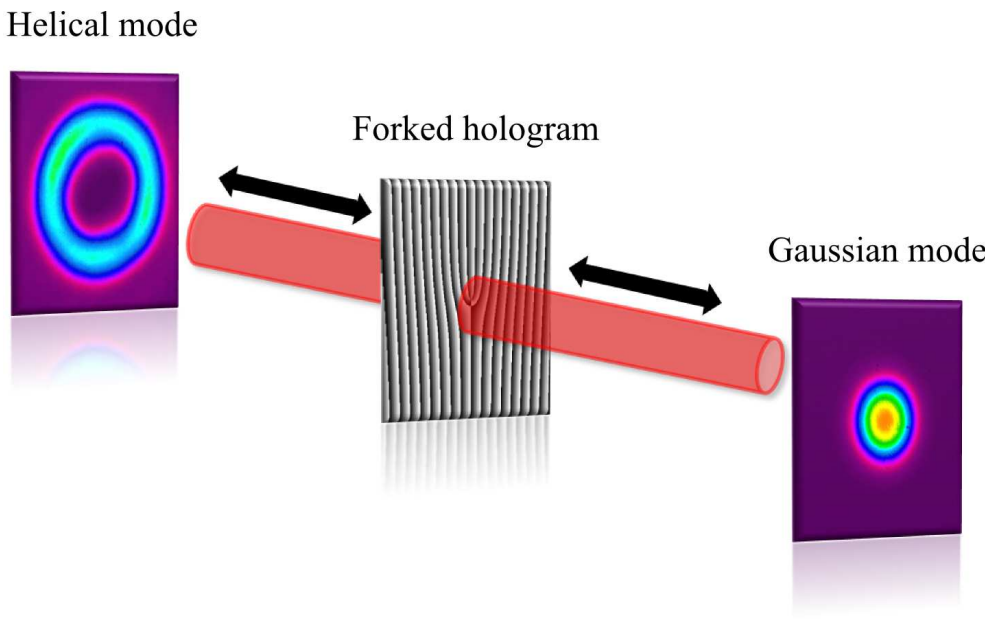

Figure 2.5: A spatial light modulator encoded with an azimuthal phase dependence, $\exp(i\ell\phi)$, shapes a Gaussian beam into a helically-phased beam in the first diffraction order. This process also works in reverse such that a helical beam can be converted into a Gaussian beam. .

of a superposition of the desired object beam and undiffracted reference beam, which produces a distorted object beam. To overcome this issue, a diffraction grating is placed on top of the computer-generated hologram so as to separate the diffracted object beam (the first order) from the undiffracted reference beam (the zero order). Thus the holographic spiral phase plate with a diffraction grating will produce a helical beam in the first diffraction order. Such holograms are referred to as "forked" diffraction gratings, where the number of fork prongs is proportional to the azimuthal index, shown in Fig. 2.4. That is, a Gaussian beam illuminating a phase-only forked hologram of particular azimuthal index, ℓ, produces a helically-phased beam in the first diffraction order.

This process also operates in reverse, in that a beam with OAM ℓ incident on a forked hologram with an azimuthal index $-\ell$, will produce a Gaussian beam as illustrated in Fig. 2.5. When coupled to a single-mode fibre (SMF), this becomes an efficient method in which to measure the OAM of a laser beam. Only the fundamental mode (a Gaussian beam) can propagate through a SMF, such that the hologram on the SLM together with the SMF, act as a "match-filter". An incoming beam with OAM ℓ will only couple into the SMF if the hologram is encoded with an azimuthal phase index of equal magnitude but opposite

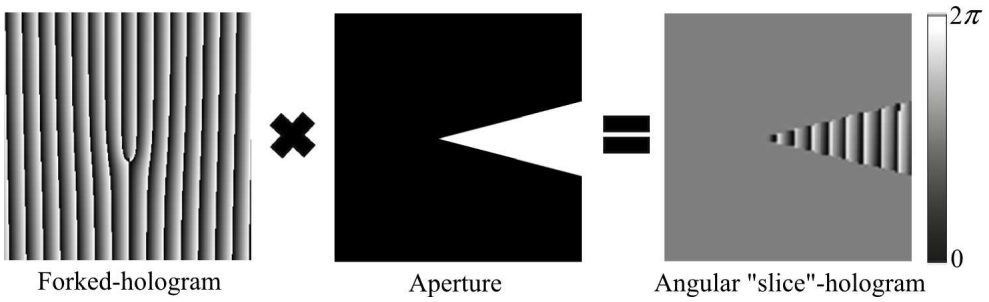

Figure 2.6: Generation of an angle hologram used to measure angular position correlations.

sign, ℓ. If the SMF is connected to a detector sensitive to single photons, then the technique can be similarly applied to entangled photon pairs.

The conjugate variable of OAM, angular position, can also be measured in a similar manner. Angular slits of width $\Delta\theta$ are encoded with the same forked holograms (shown in Fig. 2.6), where the orientation of the slit-hologram is specified by ϕ.

A clear advantage in using SLMs is the ease in which the displayed hologram can be changed and positioned. The symmetrical intensity distribution seen in a helical mode is extremely sensitive to the position of the centre of the hologram with that of the incident Gaussian mode. A lateral shift of less than 50 μm will produce an uneven intensity distribution. This sensitivity is often difficult to achieve using physical translation stages, but is readily achievable with digital re-positioning programs. Thus, the forked holograms offer an effective method to test whether a setup is correctly aligned. Similarly, the slit holograms can be used to ensure the optics are placed in the correct image planes. A sharp, clear "slice" should be seen at the image plane of the SLM if the subsequent optics have been correctly positioned. The correct alignment and positioning of the optics is particularly important when attempting simultaneous-arrival measurements of single photons.

2.2.1 Detection of single photons

The arrival of a pair of single photons requires particular detection devices, which are both electronically fast and efficient. Typically, single photons are detected using avalanche photo-diodes (APDs) with a quantum efficiency of approximately 60%. Evidently, the laboratory must be as dark as possible when using these detectors. Nonetheless, the measured single photon count rate of the dark laboratory without a lasing source (the dark counts), is

approximately 200 counts per second.

Of course, in entanglement we wish to detect the arrival of a photon pair, that is, the simultaneous arrival of a photon at each detector. A coincidence counter, connected to both detectors allows the simultaneous arrival or coincidence count to be measured. When a photon is detected by one detector it initiates the trigger in the second detector such that the arrival of a photon in the second, registers a coincidence count. Naturally, there must be a limit placed on the interval in which the second photon is detected, known as the gating time. Even with a very narrow time interval, uncorrelated photon coincidence counts may be recorded, know as accidental counts and can be estimated as $C_{acc} = S_A S_B \Delta t$, where S_A and S_B are the single count rates from each detector and Δt is the gating time.

2.3 Experimental setup

I will describe the general concept of our setup using collinear down-conversion. However, we also utilise the non-collinear geometry in some of our earlier experimental work.

2.3.1 Back-projection mode

There has been a great deal of interest in mathematically determining a method to predict quantum correlations in particular reference to quantum communication and imaging [70; 71; 72; 73]. The measurable correlation of the entangled photons in a typical SPDC experiment depends on the quality of state generation (e.g. the range of OAM states that SPDC actually produces) and the state detection (e.g. the range of the OAM states that can be detected by the measurement scheme). It is useful to isolate the effect of generation from detection, and vice versa. We are interested in investigating the quality of our detection system, and so to this end, we first perform a back-projection experiment inspired by the advanced-wave representation of Klyshko [74].

The Klyshko picture is useful in assessing the conditional probability of detecting a photon at detector B given that another photon is detected at detector A. Klyshko considered the field detected in arm A as propagating in reverse back to the crystal plane where it reflects off the crystal to propagate forward through the system to detector B. Using this picture and geometrical optics arguments, the two-photon correlations measured in SPDC can be

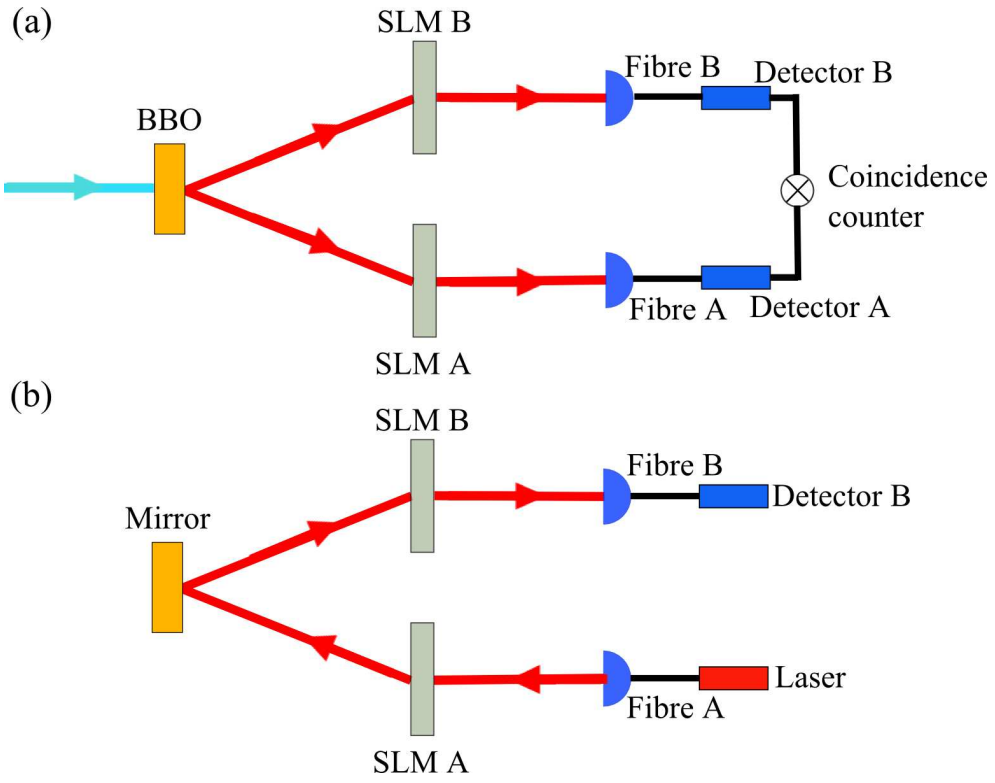

Figure 2.7: (a) Schematic of an entanglement setup. The entangled photon pairs were generated by the nonlinear crystal, the combination of the spatial light modulators (SLMs) and detectors projected the photon pair into a particular state and the detection of the pairs was measured with a coincidence counter. (b) Back-projection schematic, where the nonlinear crystal is replaced with a mirror such that SLM A is imaged onto SLM B (the imaging details are given in Sec. 2.3.2). Light from a 710 nm diode laser was coupled into fibre A, where after it was imaged to SLM A followed by SLM B and then re-coupled into fibre B.

predicted, as in the ghost imaging and two-photon optics experiments in [70; 75]. More than a theoretical tool, the Klyshko picture can also be applied experimentally. One of the detectors can be replaced with a classical light source and propagated through one arm back onto the crystal plane, where a mirror has been placed (this corresponds to the wave propagating in reverse). At the crystal, this back-projected beam was reflected and propagated forward onto the components of the other arm and onto the other detector. The number of photons registered by this detector can be optimised to ensure the stringent alignment required by the system, and more importantly, can be used to predict the expected behaviour of the two-photon correlation. With these in mind, we implemented a back-projection experiment. Figure 2.7(a) shows a simple schematic of an entanglement setup. The entangled state is generated at the non-linear crystal then projected into a particular spatial mode using

SLMs and finally detected by single photon detectors.

Figure. 2.7(b) illustrates the changes made to Fig. 2.7(a) in order to perform back-projection measurements. A 710 nm diode laser with a Gaussian profile replaced detector A and was connected to fibre A. The output was imaged through the system to SLM A, which was then imaged onto a mirror at the plane of the crystal (all imaging systems are specified in Sec. 2.3.2). From here, the light was imaged onto SLM B, and SLM B was in turn imaged onto the facet of single-mode fibre B. The fibre was coupled to detector B which registered the single photon count rate. Figure 2.7(b) shows only a schematic of the back-projection experiment, however, the full details, including lenses and apertures, are given in Sec. 2.3.2. In order to have significant single photon counts, in the context of the spatial modes, which we are trying to measure, maximum coupling of the light from fibre A to fibre B occurs when the transmission functions encoded on the SLMs are phase-conjugates of each other. These patterns should ensure the fundamental mode from fibre A is coupled into fibre B. To illustrate this, if a positive lens function with focal length f_1 is encoded onto SLM A, a negative lens function with focal length f_2 must be encoded onto SLM B to produce a Gaussian mode which can only then be coupled into fibre B. When $f_1 = -f_2$ the transverse and angular positions of the initial and final beam remain the same. However, identical focal lengths result in a change in the angular position, producing a divergent beam at fibre B and thus reducing the coupling efficiency.

2.3.2 Down-conversion mode

Both fibres were connected to their respective detectors and the mirror in the back-projection mode was replaced with a non-linear crystal to begin our down-conversion experiment, as shown in Fig. 2.8. In our experiment a mode-locked ultraviolet pump source with a wavelength of 355 nm and average power of 350 mW was used. The laser produces pulses at 80 MHz, each pulse is made up of 10^9 photons. The pump source was used to pump a 3-mm-thick type I barium borate (BBO) crystal to produce collinear, degenerate entangled photon pairs via SPDC. On average, 1 photon pair in every 10^5 pulses is produced in the SPDC process. This relates to an efficiency of 10^{-12}. The SPDC process requires a balance between generating sufficient photon pairs for reasonable counting times, and errors introduced when many photon pairs are produced within the same time window. The balance

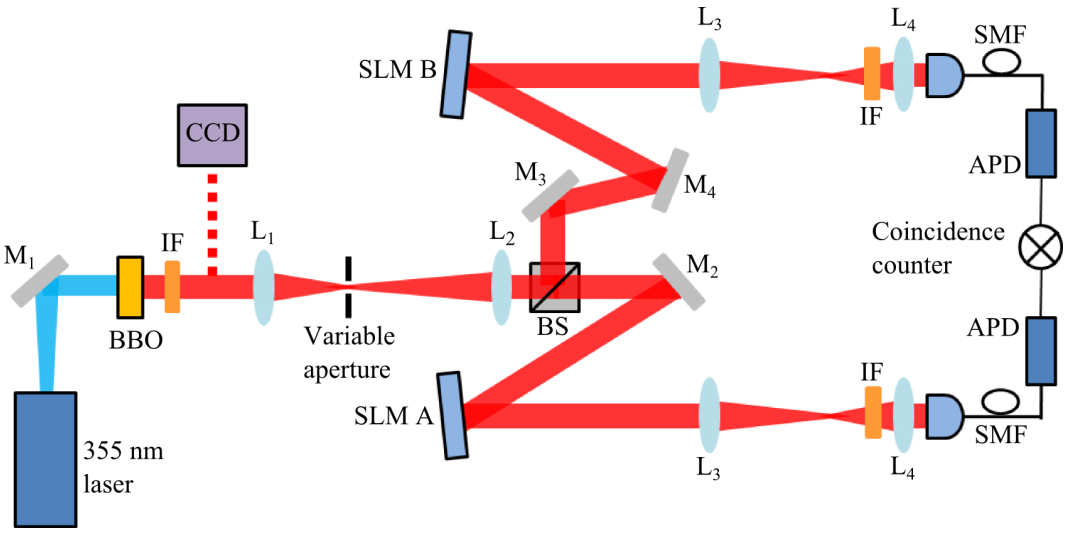

Figure 2.8: Experimental setup used to detect the orbital angular momentum eigenstate after spontaneous parametric down-conversion. The plane of the crystal was relay imaged onto two separate spatial light modulators (SLMs) using lenses, L_1 and L_2 ($f_1 = 200$ mm and $f_2 = 400$ mm), where the helical modes were selected. Lenses L_3 and L_4 ($f_3 = 500$ mm and $f_4 = 2$ mm) were used to relay image the SLM planes through 10 nm band-width interference filters (IF) to the inputs of the single-mode fibres (SMF). Each SMF was connected to an avalanche photo-diode (APD), which were connected to a common coincidence counter to measure the simultaneous arrival of a photon in each arm.

between these parameters is largely determined by the energy and the repetition rate of the pump source. Increasing the energy of the pulse would also increase the pair production rate through an improved efficiency of the SPDC process. Unfortunately this also increases the error in the system by way of multiple pair generation. The length of the non-linear crystal also has an effect on the SPDC efficiency, where a thicker crystal will produce more photon pairs per pulse. However, this must be weighed up against the generated bandwidth (the number of entangled OAM modes produced from the crystal), which is also dependent upon crystal length. An interference filter was placed after the crystal to reflect the pump beam and transmit only the 710 nm down-converted light. The front plane of the crystal was then imaged ($f_1 = 200$ mm, $f_2 = 400$ mm) onto two separate HoloEye PLUTO phase-only SLMs. The reflective LCD screen had a resolution of 1920×1080 pixels with an 8 μm pixel pitch and operated with a frame rate of 60 Hz. Just as polarisers were used to "select" a particular polarisation state, the SLMs allow a specific state to be chosen into which the photon will be projected. The OAM states can be measured by any orthogonal basis set, but we chose the helical modes, which are commonly used to measure OAM entanglement.

The SLM planes were then re-imaged ($f_3 = 500$ mm, $f_4 = 2$ mm) and coupled into SMFs (mode-field diameter = 4.6 μm) so as to extract only the Gaussian modal components. Interference filters centred at 710 nm were placed in front of each fibre coupler to prevent any scattered pump light to enter the fibres. The fibres connected to Perkin Elmer APDs allowed the arrival of a photon pair to be registered using a HydraHarp 400 coincidence counter. The time between photon pairs in turn dictates the time window of the detection system (gating time). Since the pulses arrived at intervals of 12.5 nanoseconds, we selected a gating time of 12.5 nanoseconds to minimise the error of multiple photon pairs arriving at the same time.

The measured coincidence count rate can be numerically determined by calculating the overlap integral of the back-projected signal, idler beams with the pump field at the crystal plane. The coincidence rate is proportional to the overlap intergal [76], that is,

$$C \propto \frac{|\int \psi_s^* \psi_i^* \psi_p dA|^2}{\sqrt{|\int \psi_s^* \psi_p|^2 dA \, |\int \psi_i^* \psi_p|^2 dA}}, \tag{2.3.1}$$

where ψ_s, ψ_i and ψ_p are the modes of the signal, idler and pump beams, respectively. The ratio of the pump waist w_p with the signal (idler) waist $w_{s,i}$ is given as [66]:

$$\gamma_{s,i} = \frac{w_p}{w_{s,i}}. \tag{2.3.2}$$

In terms of the imaging systems shown in Fig. 2.8, we calculated our ratio to be $\gamma = 2$. This appears to be a fair ratio when finding a balance between efficiency and the spiral bandwidth. Miatto *et al*. investigated three different ratios; 0.5, 2 and 4 with regard to helical modes and showed that although the spiral bandwidth does increase with γ, the count rate begins to decrease almost to the accidental count rate.

2.4 Quantum measurements

The collinear setup was used to demonstrate some fundamental properties of the entangled state. The following section describes different experimental techniques used to investigate and characterise OAM entanglement.

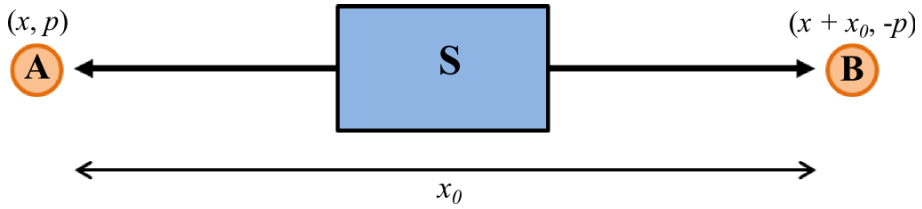

Figure 2.9: The original Einstein-Podolsky-Rosen paradox, where particles A and B move away from a source, S. A position measurement (x) on A, predicts the position of B from their relative positions and a momentum measurement (p) on A predicts the momentum of B from the conservation of momentum.

2.4.1 EPR paradox

The 1935 Einstein, Podolsky and Rosen (EPR) thought experiment concluded that quantum mechanics was incomplete by highlighting the uncertainty principle of quantum mechanics, where the knowledge of one conjugate quantity precludes the knowledge of the other [1]. They used the continuous conjugate quantities, position and momentum, to argue that either quantum mechanics was incomplete or that the measurements of two spatially separated particles were independent of each other. They highlighted their argument with a specific example using position, x and momentum, p. They considered two particles, A and B, moving away from a source, S (shown in Fig. 2.9). If a measurement is performed on A to give its position as x, then according to quantum mechanics the position of B can be predicted to be $x + x_0$. Similarly, if the momentum of A is found to be p, then from conservation of momentum, the momentum of B must be $-p$. Both predictions are made without disturbing particle B and both correspond to elements of reality. However, quantum mechanics also states that we cannot know, simultaneously, the position and momentum of a particle with absolute certainty.

At the time, the idea that a measurement of a property on one particle could immediately determine the corresponding property of the other particle seemed impossible, and thus the manuscript concluded that quantum mechanics was likely to be an incomplete theory.

Bohm later presented a modified version of the EPR paradox with discrete variables by considering the spin components of two spin-1/2 particles [77]. However, Reid proposed an experiment that would return to the original EPR paradox between continuous variables [78], which was followed by an experimental demonstration by Ou *et al.* in 1992 using quadrature-phase amplitudes [79]. Using position and momentum-entangled photons,

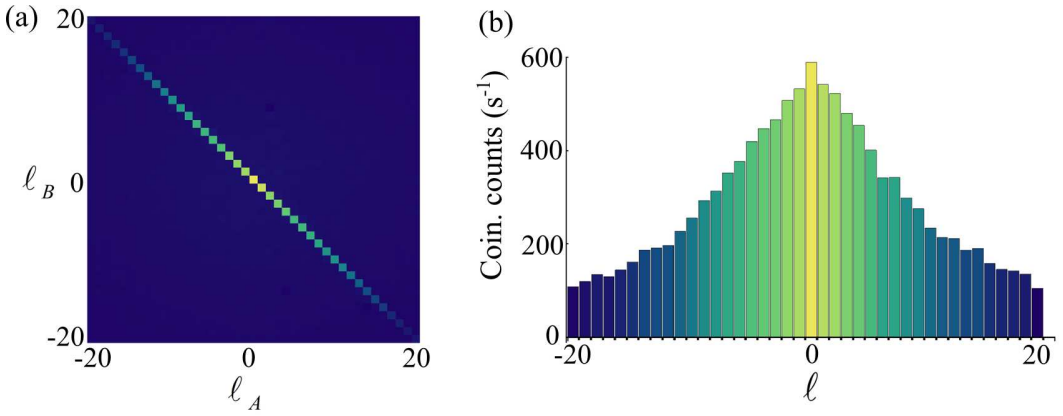

Figure 2.10: Experimental results showing (a) a density plot of the coincidence counts per second as a function of the azimuthal index ℓ of the holograms and (b) the non-zero diagonal elements representing a spiral bandwidth plot. The full-width-half-maximum of the spiral bandwidth is approximately 15.

the EPR paradox was demonstrated by Howell *et al.* [61], where an uncertainty value of $(\Delta x_i)^2(\Delta p_i)^2 = 0.004\hbar^2 \leq \hbar^2/4$ was shown. The paradox was extended to OAM and its conjugate variable angular position [80] by using an uncertainty principle for angular position and angular momentum $(\Delta\ell)^2(\Delta\phi)^2 \geq 1/4$ [81]. The experimental implementation was performed by Leach *et al.* where they demonstrated an uncertainty value of 0.024 ± 0.004, an order of magnitude less than the lower bound of the inequality [82]. We follow the method presented in [82] and show a strong demonstration of the EPR paradox.

Making use of the experimental setup in Fig. 2.8, each SLM was encoded with forked-holograms ranging in ℓ from -20 to 20, one after another. That is, the hologram on SLM A was fixed, while the SLM B displayed a sequence of forked-holograms from $\ell = -20$ to $\ell = 20$, after which the hologram on SLM A was changed and the process was continued. Each hologram on SLM B was displayed for 10 seconds, such that the accumulated coincidence rate could be measured for a 10 s integration time, thereby obtaining a statistically accurate coincidence measurement. Figure 2.10(a) shows the measured coincidence counts, while Fig. 2.10(b) only shows the diagonal elements of (a), which is commonly known as the measured spiral bandwidth.

The anti-correlated diagonal is consistent with OAM conservation, that is $m = \ell_s + \ell_i$. While the coefficients in the OAM spectrum demonstrate a decreasing trend from $\ell = 0$, the size of the mode is another contributing factor as the mode increases with the azimuthal

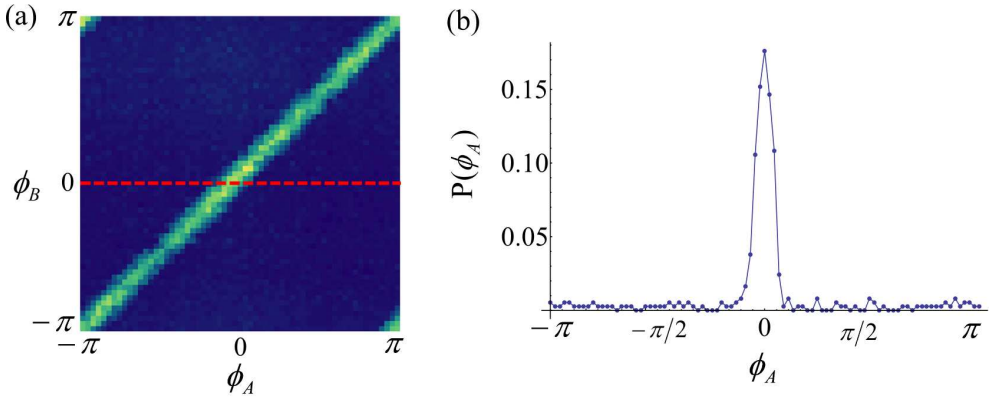

Figure 2.11: Experimental measurements showing (a) a density plot of the coincidence counts per second as a function of the orientation of the angular holograms. The holograms on each spatial light modulator were rotated through 2π. (b) Probability distribution of the angular position ϕ_A for $\phi_B = 0$, taken along the red dotted line in (a).

index, which results in a loss of efficiency, resulting in a decreasing trend from $\ell = 0$. Another important feature obtained from Fig. 2.10(a) is the values of the off diagonal elements. Theoretically these should be zero, but experimentally this is often impossible to achieve as the spiral bandwidth is highly sensitive to misalignment. We measured the off-diagonal elements to be less than 5% of their corresponding diagonal element. From Fig. 2.10(b) we measured the full-width-half-maximum (FWHM) value to be 15 and the Schmidt number $K = 23.2$.

A similar procedure was undertaken to measure the angular position correlations. An angular slit hologram was encoded onto each SLM; one hologram fixed at a particular orientation ϕ_A while the other hologram rotated in small increments through 2π. In a ghost imaging experiment, an aperture is placed in one arm, while the detector in the other arm is scanned through its transverse position, resulting in the reconstruction of the aperture shape. Similarly, the width of the angular hologram can be determined from the measured coincidence counts. A sharp coincidence peak was recorded when the holograms were both orientated at the same angle, see Fig. 2.11, where the width of the peak gives the width of the angular slit.

From the data recorded for both the spiral and angular bandwidths, we calculated the uncertainty relationship between the two. A profile from the centre of each spectrum was plotted and fitted with a Gaussian distribution (Fig. 2.12), which gave the following widths

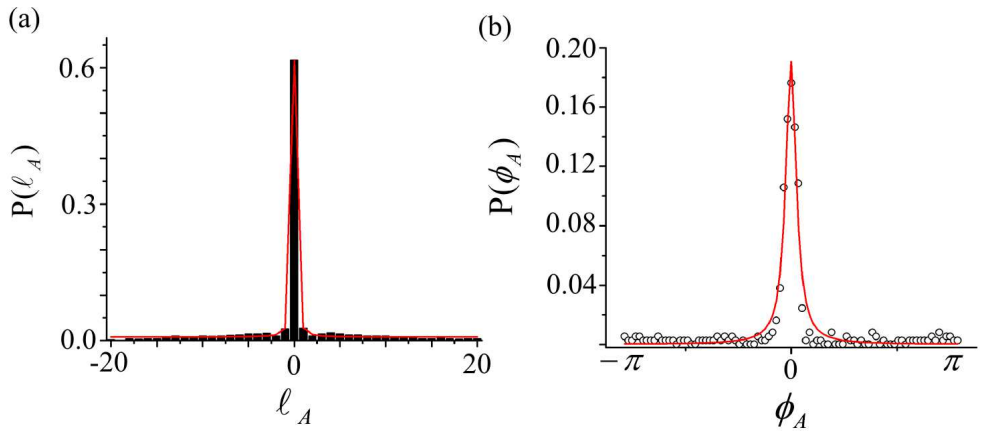

Figure 2.12: Probability distributions for (a) the orbital angular momentum ℓ_A for $\ell_B = 0$ and (b) the angular position ϕ_A for $\phi_B = 0$. A Gaussian distribution has been fitted to both to determine the widths of each plot, which were used to demonstrate the EPR-Reid criterion.

$(\Delta\ell)^2 = 0.128 \pm 0.023$ and $(\Delta\phi)^2 = 0.056 \pm 0.006$. Therefore, by taking the product of the two $(\Delta\ell)^2(\Delta\phi)^2 = 0.007 \pm 0.001$, the EPR-Reid criterion is satisfied as the product is clearly smaller than the uncertainty relation of 0.25 in Eq. (10).

2.4.2 CHSH-Bell Inequality

The EPR paradox does not eliminate the possibility of hidden variables. In 1964, Bell proposed a theorem in which a limit is placed on the correlations achievable by any local hidden-variable theory [83; 84]. This provided a means to test for local hidden variables. Bell's theorem, as presented by Clauser, Horne, Shimony and Holt (CHSH) [2], is described as follows. The hidden variables are denoted by λ and for any hidden variable theory, the hidden variable distribution is given by $\rho(\lambda) \geqslant 0$, where

$$\int \rho(\lambda) d\lambda = 1. \tag{2.4.1}$$

It is assumed that a measurement of the signal photon is dependent on the hidden variable λ and the measurement angle α (e.g. the orientation of a polariser). This measurement outcome is given by $A(\lambda, \alpha)$ such that $A(\lambda, \alpha) = 1$ for the detection of V_α and $A(\lambda, \alpha) = -1$ for the detection of H_α, where V_α (H_α) is the polarisation detected at α degrees from the vertical (horizontal). Similarly for the idler photon, the outcomes are given by $B(\lambda, \beta) = \pm 1$.

Let us now consider four different polariser angles $\mathbf{a}, \mathbf{a}', \mathbf{b}, \mathbf{b}'$. The polarisation correlation between a pair of photons is defined as:

$$\begin{aligned} s &= A(\lambda,\mathbf{a})B(\lambda,\mathbf{b}) - A(\lambda,\mathbf{a})B(\lambda,\mathbf{b}') + A(\lambda,\mathbf{a}')B(\lambda,\mathbf{b}) + A(\lambda,\mathbf{a}')B(\lambda,\mathbf{b}') \\ &= A(\lambda,\mathbf{a})\left[B(\lambda,\mathbf{b}) - B(\lambda,\mathbf{b}')\right] + A(\lambda,\mathbf{a}')\left[B(\lambda,\mathbf{b}) + B(\lambda,\mathbf{b}')\right]. \end{aligned} \tag{2.4.2}$$

The limits on A and B (± 1) force $s = \pm 2$. The ensemble average of s is then

$$\langle s \rangle = \int s(\lambda,\mathbf{a},\mathbf{a}',\mathbf{b},\mathbf{b}')\rho(\lambda)d\lambda, \tag{2.4.3}$$

which also lies between ± 2. We define a correlation function E,

$$E(\mathbf{a},\mathbf{b}) = \int A(\lambda,\mathbf{a})B(\lambda,\mathbf{b})\rho(\lambda)d\lambda. \tag{2.4.4}$$

By writing Eq. 2.4.2 in terms of Eq. 2.4.4, allows us to describe $\langle s \rangle$ as:

$$\begin{aligned} \langle s \rangle &= E(\mathbf{a},\mathbf{b}) - E(\mathbf{a},\mathbf{b}') + E(\mathbf{a}',\mathbf{b}) + E(\mathbf{a}',\mathbf{b}') \\ &= S(\mathbf{a},\mathbf{a}',\mathbf{b},\mathbf{b}'), \end{aligned} \tag{2.4.5}$$

where S is known as the Bell parameter and $|S| \leqslant 2$ for any hidden variable theory. However, quantum mechanics violates this inequality for particular polariser settings with a maximum value of $S = 2\sqrt{2}$.

We now wish to demonstrate such a violation with OAM modes. I mentioned in Sec. 1.2.2 that we can use the Bloch sphere to show an analogy between polarisation and OAM. As polarisation is a two state system, we chose two orthogonal OAM modes (an OAM subspace) and their superpositions in which to perform the Bell measurements. In a polarisation-based experiment, a polariser is rotated to vary from vertical to horizontal polarisation, allowing access to the superposition states along the equator of the Poincaré sphere for both the signal and idler photons. Similarly, holograms are used to access the superpositions sates of an OAM subspace and are subsequently rotated. The first demonstration of a violation of a Bell inequality in the OAM basis was shown by Leach *et al.* in 2009 [36]. We follow their methodology in demonstrating a violation of Bell's inequality for our entangled system.

The holograms used to measure the superposition states are described by:

$$|\psi\rangle = \frac{1}{\sqrt{2}}\left(|\ell\rangle + \exp(i\ell\theta)\,|-\ell\rangle\right). \tag{2.4.6}$$

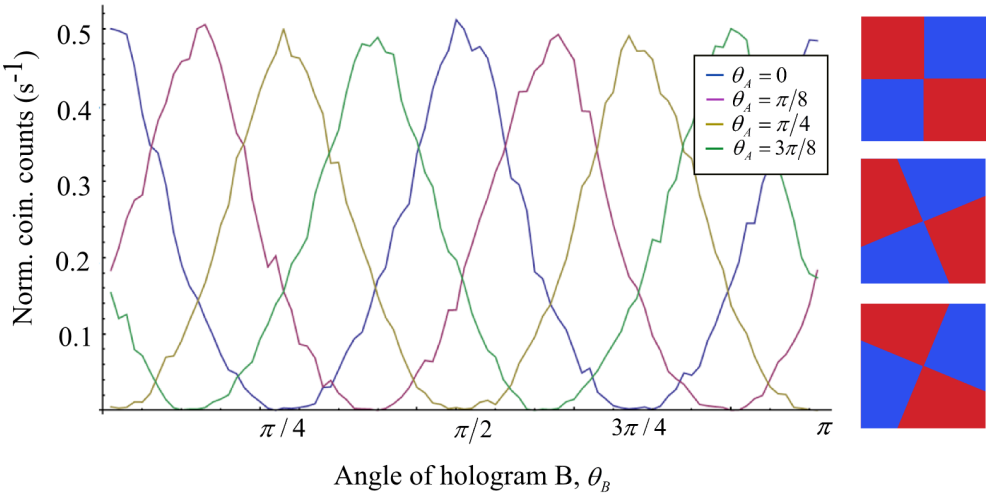

Figure 2.13: The normalised coincidence counts as a function of the orientation of the holograms on each spatial light modulator (SLM). The orientation of the hologram on SLM A was fixed while those on SLM B were rotated from 0 to π.

Here θ denotes the degree of rotation. By choosing a particular value for ℓ, we generated superposition holograms for a range of angles. The holograms were varied on both SLMs, by fixing one at orientation θ_A and rotating the other θ_B, and the coincidence count rates were measured. Figure 2.13 shows the normalised coincidence count rate as a function of the hologram orientation.

The correlation function can be rewritten more practically as:

$$E(\theta_A,\theta_B)=\frac{C(\theta_A,\theta_B)+C(\theta_A+\frac{\pi}{2\ell},\theta_B+\frac{\pi}{2\ell})-C(\theta_A+\frac{\pi}{2\ell},\theta_B)-C(\theta_A,\theta_B+\frac{\pi}{2\ell})}{C(\theta_A,\theta_B)+C(\theta_A+\frac{\pi}{2\ell},\theta_B+\frac{\pi}{2\ell})+C(\theta_A+\frac{\pi}{2\ell},\theta_B)+C(\theta_A,\theta_B+\frac{\pi}{2\ell})}, \quad (2.4.7)$$

with $C(\theta_A,\theta_B)$ being the coincidence count rate for the particular orientation of each hologram. Adapting Eq. 2.4.5, we can write the Bell parameter as:

$$S(\theta_A,\theta_B)=E(\theta_A,\theta_B)-E(\theta_A,\theta'_B)+E(\theta'_A,\theta_B)-E(\theta'_A,\theta'_B). \quad (2.4.8)$$

For the OAM subspace $|\ell|=2$, we observed a violation of the inequality by 26 standard deviations, $S=2.78\pm0.03$, thereby validating the observation of quantum correlations rather than classical correlations with hidden variables.

2.4.3 Full state tomography

Lastly, it is important to form a characterisation of the entangled states by measuring the degree of entanglement. We previously introduced the concept of a density matrix, $\rho=$

$|\psi\rangle\langle\psi|$, used to describe the statistical state of a quantum system, where the state can be represented in a complete OAM basis of vectors $|\ell\rangle$ as:

$$|\psi\rangle = \sum_{\ell} c_{\ell} |\ell\rangle. \tag{2.4.9}$$

However, constructing the density matrix from $|\psi\rangle$ requires knowledge of the complex coefficients c_{ℓ}, which in general cannot be measured directly. This expression also precludes a mixed state, which cannot be expressed with a state vector. Thus we must use a different approach, such as tomographic reconstruction.

Quantum state reconstruction or quantum tomography is the process in which precise knowledge of an unknown quantum state is established [85]. As any measurement on a quantum system will alter the state, the tomographic process requires measurements to be performed on identical copies of the initial state. After a set of measurements is performed, which must form a complete basis in the chosen Hilbert space, the density matrix or quantum state can be uniquely recovered.

The process of reconstruction of a quantum state was proposed by Fano in 1957 [86]. Since then, many experiments have been reported, and quantum tomography is an established field of research [13; 37; 85; 87; 88; 89; 90; 91; 92; 93]. An extensive analysis of qubit systems was presented by James *et al.* in 2001 [89], where they focused on polarisation entangled qubits. These techniques were then extended to the spatial components of light, where a full state tomography was demonstrated for OAM modes up to $|\ell| = 20$.

Quantum state tomography consists of reconstructing a density matrix ρ by making multiple measurements on identical copies of the relevant quantum state. The set of measured probabilities p_i for known observables A_i is given by:

$$p_i = \mathrm{Tr}[\rho A_i]. \tag{2.4.10}$$

Here A_i is a Hermitian operator with real eigenvalues, which in this case is a projection operator composed of the mode that we want to detect. The density matrix is then constructed from a complete set of such measurements. The density matrix must have non-negative eigenvalues and a trace equal to unity in order to describe a real physical system. It is possible to formulate the calculation of ρ as an inverse problem, where one must invert the matrix A whose rows are composed of the detector states A_i in the basis of the Laguerre-Gauss modes. However, the calculation of ρ using matrix inversion does not always ensure

the above conditions due to experimental noise, and different approaches are required to reconstruct physically real quantum states. The method that we use consists of using linear combinations of generalised Gell-Mann matrices, which form a complete basis set in which to build matrices for any given dimension [90].

In the case of a qubit, a single photon in a two-dimensional state space, the density matrix can be represented as a linear combination of the Pauli matrices [89]:

$$\rho = \frac{1}{4}\sigma_0 \otimes \sigma_0 + \sum_{mn} \rho_{mn}\sigma_m \otimes \sigma_n \tag{2.4.11}$$

where σ_x represents the Pauli matrices for $x = 1,2,3$.

From the Bloch sphere, we focused on the equator states $\theta = 0, \pi/4, \pi/2, 3\pi/4$ together with the pure states $|\ell\rangle$ and $|-\ell\rangle$.

For a qubit system, the state vector has a length of 4 and thus a density matrix of 4×4. We require at least 15 measurements to match the number of matrix elements [89; 90]. A sufficient set would be given by the pure states $|\ell\rangle$ and two superposition states ($\theta = 0, \pi/2$) from Eq. (2.4.6) in each of the signal and idler modes of the experiment. However, if an over-complete set of measurements is chosen, additional information is available to compensate for measurement errors due to natural photon number fluctuations [13]. In matrix form, the qubit density matrix is written as:

$$\rho = \begin{pmatrix} a_{11} & a_{12}e^{i\phi_{12}} & a_{13}e^{i\phi_{13}} & a_{14}e^{i\phi_{14}} \\ a_{21}e^{i\phi_{21}} & a_{22} & a_{23}e^{i\phi_{23}} & a_{24}e^{i\phi_{24}} \\ a_{31}e^{i\phi_{31}} & a_{32}e^{i\phi_{32}} & a_{33} & a_{34}e^{i\phi_{34}} \\ a_{41}e^{i\phi_{41}} & a_{42}e^{i\phi_{42}} & a_{43}e^{i\phi_{43}} & a_{44} \end{pmatrix}. \tag{2.4.12}$$

Here a_{ij} and ϕ_{ij} are the amplitudes and phases of the density matrix elements, respectively. The probability to detect one photon in state $|\ell\rangle$ and the other in state $|-\ell\rangle$ is expressed by the diagonal terms. The off-diagonal terms are determined from measurements in the superposition states.

We generated six different states on each SLM, resulting in a total of 36 coincidence measurements. Therefore for a two-dimensional state, we use an over-complete set of measurements (36) to determine the 16 density matrix elements. We used a least squares fitting program to calculate the best density matrix according to our measurements. We followed the procedure in Jack *et al.* [37] where the 10 amplitudes and 6 phases from the density

matrix in Eq. 2.4.12 are chosen such that the following equation is minimised [37; 94]:

$$\chi^2 = \sum_{i=1}^{N^2} \frac{\left(p_i^{(M)} - p_i^{(P)}\right)^2}{p_i^{(P)}}. \tag{2.4.13}$$

Here, $p_i^{(M)}$ are the measured probabilities from the experiment, and $p_i^{(P)}$ are the predicted probabilities calculated from the guessed density matrix ρ_d, together with the known measurement states A_i; see Eq. (2.4.10). The reconstruction of a density matrix does not necessarily have positive eigenvalues and can therefore represent a non-physical quantum state. Due to the presence of experimental noise, it is in fact likely that such a case occurs. We therefore take an approach to the quantum state reconstruction which ensures that our state has all the required properties. In order to construct the guessed density matrix ρ_d in Eq. 2.4.13, we first construct a matrix G from a linear combination of the identity matrix and Gell-Mann matrices for d^2 dimensions. As these matrices form a basis for any matrix in d^2 dimensions, we ensure a minimum number of coefficients required in the minimisation process. The guessed density matrix is then constructed using the following equation, which ensures that all the eigenvalues of ρ_d are positive:

$$\rho_d = \frac{G^\dagger G}{\mathrm{Tr}(G^\dagger G)}. \tag{2.4.14}$$

Thus the density matrix is, by construction, Hermitian and positive semi-definite with unit trace [89]. By choosing the appropriate coefficients of the Gell-Mann matrices, we can minimise χ^2, thus producing the closest physical density matrix that represents the high-dimensionally entangled quantum state. In matrix form, the two-dimensional reconstructed density matrix was calculated to be

$$\rho = \begin{pmatrix} 0.011 & -0.001 & 0 & -0.002 \\ -0.001 & 0.48 & 0.48 & 0.036 \\ 0 & 0.48 & 0.49 & 0.036 \\ -0.002 & 0.036 & 0.036 & 0.012 \end{pmatrix} + i \begin{pmatrix} 0 & 0.043 & 0.048 & 0.003 \\ -0.043 & 0 & -0.039 & 0.042 \\ -0.048 & 0.039 & 0 & 0.048 \\ -0.003 & -0.042 & -0.048 & 0 \end{pmatrix} \tag{2.4.15}$$

This is visually represented in Fig. 2.14.

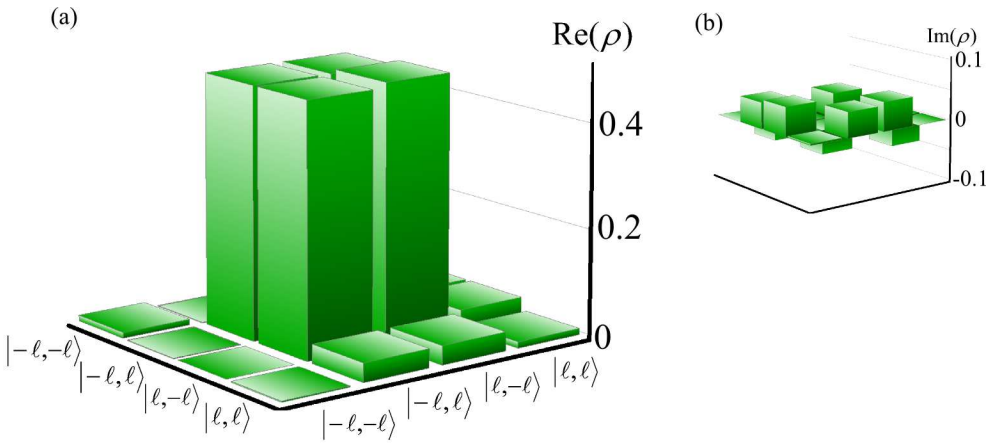

Figure 2.14: Graphical representation of the (a) real and (b) imaginary parts of the two-dimensional density matrix.

2.4.4 High-dimensional entanglement

We can now generalise this two-dimensional tomographic reconstruction to d - dimensional state spaces. High-dimensional entanglement has been reported up to dimension $d = 12$ [10], demonstrated through violations of Bell-type inequalities. Recently, high-dimensional entanglement has been imaging using an electron-multiplying charge-coupled device to observe entanglement of approximately 2500 spatial states [95]. The state of hyper-entangled photons, which are entangled in several degrees of freedom, has been characterised via quantum state tomography [96]. Tomography of entangled states up to dimension $d = 3$ has also been reported [13]. However, higher-dimensionally entangled states were only characterised in 2011 [97] due to the inherent time demands for the large sets of measurements required.

The state of a single qu$d$it, which exists in a d-dimensional state space, can be expressed as a linear combination of the generalised Gell-Mann matrices:

$$\rho = \frac{1}{d}\tau_0 + \sum_{n=1}^{d^2-1} b_n \tau_n. \tag{2.4.16}$$

Here τ_0 is the d-dimensional identity matrix and τ_n are the generalised Gell-Mann matrices in d dimensions, with corresponding complex coefficients b_n.

This state can also be represented as a superposition of the OAM states of light as:

$$|\Psi\rangle = \sum_{\ell=-[d/2]}^{[d/2]} c_\ell |\ell\rangle, \tag{2.4.17}$$

where [x] is the integer part of x. We consider only states with radial mode index $p = 0$. The squares of the coefficients must sum to unity for normalization, and $c_{\ell=0}$ must equal zero for even d.

The density matrix of the OAM state of light of Eq. (2.4.17) can then be represented by linear combinations of the high-dimensional Gell-Mann matrices as in Eq. (2.4.16). The coefficients of these matrices are determined by a set of measurements that must be tomographically complete. One such simple set consists of measurements of the pure OAM states:

$$|\Psi\rangle_\ell = |\ell\rangle\,, \tag{2.4.18}$$

and superpositions of just two of these states:

$$|\Psi\rangle_{\alpha,\ell_1,\ell_2} = \frac{1}{\sqrt{2}}\left(|\ell_1\rangle + e^{i\theta}\,|\ell_2\rangle\right), \tag{2.4.19}$$

where $\ell, \ell_1, \ell_2 = -[d/2], ..., [d/2]$ and $\ell_1 < \ell_2$.

The two-photon state is then the tensor product of two single qu$d$it states from Eq. (2.4.17), with opposite OAMs:

$$|\Psi\rangle = \sum_{\ell=-[d/2]}^{[d/2]} c_\ell\,|\ell\rangle_s \otimes |-\ell\rangle_i\,. \tag{2.4.20}$$

Here, $|c_\ell|^2$ gives the probability of finding a signal photon in state $|\ell\rangle_s$ and idler photon in state $|-\ell\rangle_i$. The range of ℓ over which $|c_\ell|^2$ is appreciable is known as the spiral bandwidth, and detailed analysis of the properties that affect it can be found in Ref. [39; 42; 98].

In analogy to using Eq. (2.4.16) to represent the single qu$d$it state of Eq. (2.4.17), the density matrix of a two-photon qu$d$it state [Eq. (2.4.20)] can be expressed as

$$\rho = \sum_{m,n} b_{m,n}\,\tau_m \otimes \tau_n, \tag{2.4.21}$$

where $b_{0,0} = 1/d^2$ for normalization. Since we have two qu$d$its, each in a d-dimensional space, we have a state vector of length d^2, resulting in a $d^2 \times d^2$ density matrix. In order to determine the density matrix, we require a number of measurements at least equal to the number of elements in the matrix, which is d^4 [13; 89]. The number of possibilities where $\ell_1 < \ell_2$ is equal to the binomial coefficient $\binom{d}{2}$ so that the total number of measurement states for the signal or idler mode is:

$$N = 4\binom{d}{2} + d. \tag{2.4.22}$$

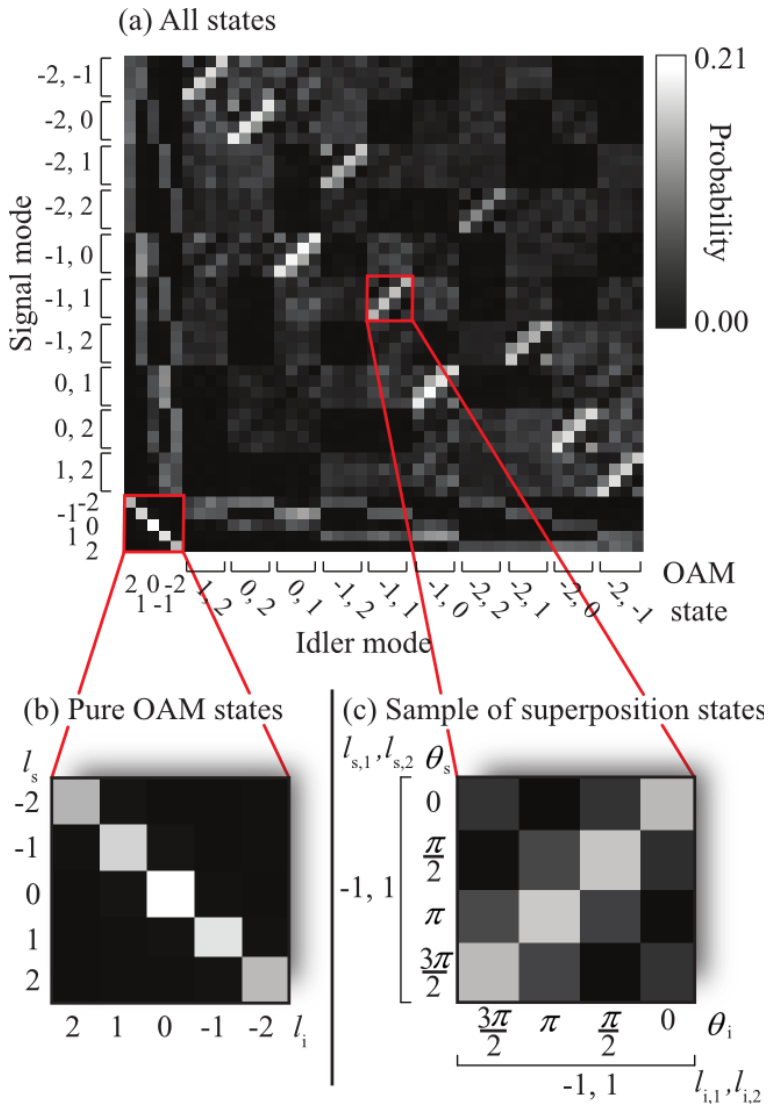

Figure 2.15: (a) The complete set of measured probabilities for dimension 5. (b) The pure orbital angular momentum (OAM) states. (c) A sample of the superposition states. Here, θ_i denotes the phase difference in the idler arm, from Eq. (2.4.19), and θ_s denotes the same in the signal arm. The OAM states separated by a comma denote ℓ_1, ℓ_2 as in Eq. (2.4.19), while the single states denote ℓ as in Eq. (2.4.18).

We measure the coincidence count rates for every combination of these states for both the signal and idler photons, thus resulting in a total number of measurements of N^2. This number increases very quickly with dimension, requiring 225 measurements for $d = 3$ and 4356 measurements for $d = 6$. We reconstructed the density matrix of the entangled quantum states for dimensions ranging from $d = 2$ to $d = 6$. The probabilities measured for $d = 5$ are shown in Fig. 2.15.

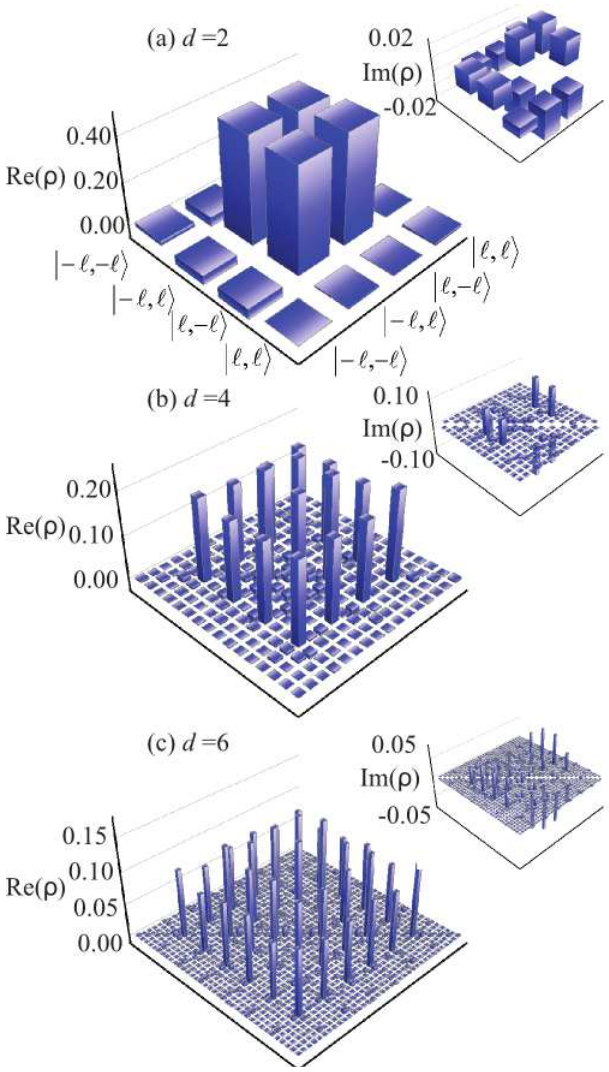

Figure 2.16: The density matrices for even dimensions 2 through 6. The axes for dimension 2 are labelled, and the higher dimensions follow the same convention. For example, the labels for the $d = 4$ case would read $\langle 2,2|, \langle 2,1|, \langle 2,-1|, \ldots$ and $|-2,-2\rangle, |-2,-1\rangle, |-2,1\rangle$, etc., where we use the convention $|\ell_s, \ell_i\rangle$ to be equivalent to $|\ell\rangle_s |\ell\rangle_i$.

The reconstructed density matrices for even dimensions are shown in Fig. 2.16. In each case, the eigenvector with the highest eigenvalue corresponds very closely to the appropriate entangled state given in Eq. (2.4.20). The imaginary components of the density matrices arise because of coefficients in the entangled states that have a small but measurable phase shift between them. This phase shift occurs because some modes have a larger Gouy phase than others. In our experiment, this phase is detected because the facets of the optical fibres that detect the signal and idler modes may not be in the same optical plane and thus do not image the exact same plane of the non-linear crystal.

The density matrix completely characterises the quantum state; thus once it has been determined, it is possible to make predictions with regards to quantum information protocols. For example, it is possible to determine the degree of entanglement and test whether the states reach the criteria required for violation of the generalised Bell inequalities [10; 99].

Firstly, the linear entropy $S_L = 4/3\left[1-\mathrm{Tr}(\rho)^2\right]$ defines the purity of the system [13], where the linear entropy of a pure entangled state is zero [37]. We find the linear entropy is low for lower dimensions ($S_2 = 0.02 \pm 0.01$), indicating close to pure states. The linear entropy increases with dimension ($S_6 = 0.40 \pm 0.01$), indicating increasingly mixed states [see Fig. 2.17(a)]. The fidelity is a measure of how close our reconstructed state is to the target state, which is the (pure) maximally entangled state in this case. The fidelity is given by:

$$F = \left[\mathrm{Tr}(\sqrt{\sqrt{\rho_T}\rho_d\sqrt{\rho_T}})\right]^2. \tag{2.4.23}$$

Here, $\rho_T = |\psi_T\rangle\langle\psi_T|$ is the target state with $|\psi_T\rangle = 2^{-1/2}(|\ell\rangle_A|-\ell\rangle_B + |-\ell\rangle_A|\ell\rangle_B)$ and ρ_d is our measured reconstructed state [100]. For low dimensions, we find good fidelity $F_2 = 0.98 \pm 0.01$; however, the fidelity decreases with dimension and becomes as low as $F_6 = 0.67 \pm 0.01$ [see Fig. 2.17(b)]. The average error for both the entropy and the fidelity is ± 0.01, which is calculated by generating additional data sets by adding $\sqrt{C_i^M}$ fluctuations to the measured coincidence counts C_i^M and then repeating the calculations described above.

The generalised Bell inequalities [10; 99] test whether or not the observed correlations, which are predicted by quantum mechanics, can be explained by local hidden variable theories. The quantum state at the threshold of the high-dimensional Bell inequality can be denoted as [99]:

$$\rho_B = p_d^{\min}|\psi\rangle\langle\psi| + (1-p_d^{\min})\frac{\mathbb{I}}{d^2}. \tag{2.4.24}$$

Here, $\mathbb{I}$ denotes the identity matrix of dimension d^2, and $p_d^{\min}$ is the probability above which the Bell inequality is violated. The linear entropy and fidelity of the state ρ_B for dimensions $d = 2$ through $d = 6$ are shown in Fig. 2.17(a) and (b). A state with a linear entropy below that of ρ_B or a fidelity above that of ρ_B will violate the high-dimensional Bell inequality, and all of our measured states satisfy these conditions.

In theory, the quantum state produced by the parametric down-conversion process is pure [39; 42]. Thus the increase in linear entropy with dimension is almost certainly due to errors in the coincidence count rates, which are unavoidable in the detection process. As the

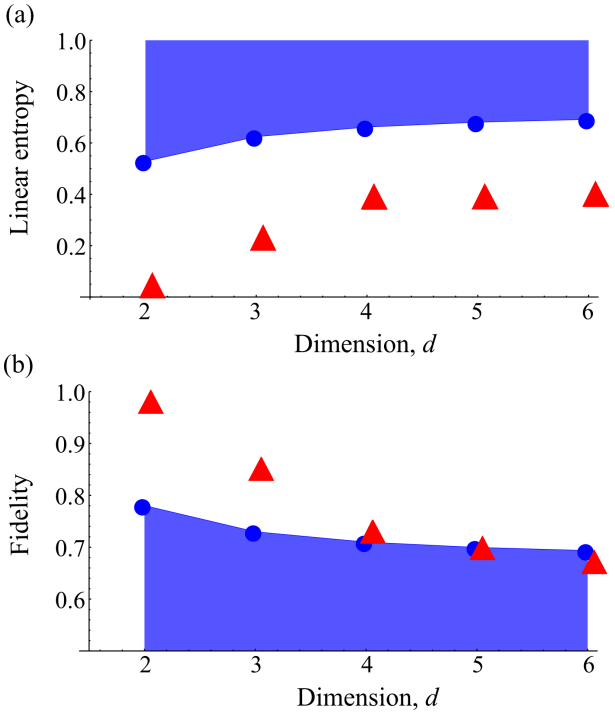

Figure 2.17: (a) Linear entropy and (b) fidelity as a function of dimension. The error for both of these measurements is ± 0.01, which is too small to be seen clearly on the graphs. In each case, the blue points represent the measured data, while the red shaded area represents the states that will not violate the appropriate high-dimensional Bell inequality.

required number of measurements increases significantly with the dimension size, so does the possibility for measurement error. The precise origin of the unwanted counts is not clear, although it is recognized that these can arise from accidental coincidences and alignment errors, leading to cross-talk between the modes. As far as the fidelity is concerned, since we compare our measured state to the maximally entangled state of Eq.(2.4.20) with $c_\ell = 1/\sqrt{d}$, we would expect the measured decrease due to the finite number of entangled modes, which is set by the spiral bandwidth.

2.5 Conclusion

In this chapter, we have introduced the techniques and equipment required to demonstrate quantum entanglement in the OAM basis. We make use of SPDC to generate our entangled photon pairs and illustrated how the tilt of the non-linear crystal allows us to move from non-collinear to collinear down-conversion. We then used SLMs encoded with specific "forked" holograms together with SMFs to measure the OAM states of each photon and

found that OAM is conserved in the down-conversion process.

The alignment of single photons is made easier using the method of back-projection, such that classical light is passed through the setup from one fibre to the other. We used this technique to simulate the expected behaviour of the two-photon correlations by measuring the OAM spectrum. We saw, after returning to down-conversion mode, that the classical prediction matches very well with the coincidence correlations.

We tested our entanglement setup by performing typical quantum experiments. The first was to demonstrate the EPR paradox using OAM and angle correlations. We calculated the uncertainty relationship between the two variables to be 0.007 ± 0.001 and found that the EPR-Reid criterion was indeed violated. This initial result lead us to attempt a CHSH-Bell inequality experiment, allowing to test for local hidden variables. Using superpositions states of OAM, we calculated a Bell-parameter of $S = 2.78 \pm 0.03$, which violates the inequality by 26 standard deviations. This result provides confirmation that our measured coincidence counts are quantum correlations and cannot be described by any local hidden-variable theory.

Lastly, we have demonstrated the tomographic reconstruction of the high - dimensional quantum states of photon pairs entangled in the OAM basis. We obtained the density matrix of two entangled qu*d*its in dimensions from $d = 2$ up to $d = 6$. Recording the density matrix of entangled quantum states in higher dimensions is possible, although the required measurement times do not scale favourably with dimension size. Characterizing the states leads to fidelities ranging from $F_2 = 0.98 \pm 0.01$ to $F_6 = 0.67 \pm 0.01$ when compared with the maximally entangled state and linear entropies ranging from $S_2 = 0.02 \pm 0.01$ to $S_6 = 0.40 \pm 0.01$. These measurements and subsequent calculations are important for determining the upper bound on the dimension of an OAM space that is usable for secure quantum communications. It is measurement error that contributes to this increase in entropy and decrease in fidelity. Realising the extent to which such measurement errors corrupt the state is an important consideration when utilizing such high-dimensionally entangled states in other quantum information protocols. Of course, there are alternative methods to achieve high-dimensional entanglement, such as the use of multi-sector phase plates that maximise the Shannon dimensionality [101]. It has also been shown that Ince-Gaussian modes can also achieve high-dimensional entanglement based on a three-dimensional entanglement

witness [102].

These experimental results are crucial for building upon the fundamental techniques of quantum entanglement measurements. We are now in a position to explore OAM entanglement and optimise its potential for quantum applications such as quantum communication. This includes understanding how the OAM states can be engineered for particular applications by either altering the generation or measurement procedures.

Chapter 3

Shaping the pump beam

We report orbital angular momentum (OAM) and angle correlations between signal and idler photons observed when the non-linear crystal used in spontaneous parametric down-conversion is illuminated by a non-fundamental Gaussian pump beam. We introduce a π-phase step to the transverse profile of the pump, before it impinges on the crystal to create a phase-flipped Gaussian mode, which is a close approximation to an HG_{10} Hermite-Gaussian-like beam. The correlations in OAM and angular position are then measured holographically using two separate spatial light modulators in the signal and idler arms. We show the transfer of the OAM spectrum of the pump to the down-converted fields, manifested as a redistribution in the OAM correlations consistent with OAM conservation. This corresponds to a modulation of the angular position correlations consistent with the Fourier relationship between the OAM and angle.

3.1 Introduction

Thus far I have introduced the fundamental principles of orbital angular momentum (OAM) entanglement. In particular, the manner in which OAM and angle correlations are measured has formed a substantial part of Chap. 2. Similar to polarisers used in polarisation-entangled schemes, suitably designed holograms provide a simple and effective method in which to manipulate the OAM of light. The combination of the hologram, single-mode fibre and single photon detector acts as a mode analyser for the signal and idler photons. As we have seen, this has been used ubiquitously in most quantum experiments involving OAM [9; 36; 103]. As such, exploring the higher dimensions afforded by OAM then generally meant the design of holograms that would measure superpositions of different OAM states [13; 104; 105].

One can also explore the high-dimensional OAM state space by engineering the pump. Shaping the pump with more complex modes has been proposed to prepare high-dimensional entangled OAM states [65; 106], although these have not been implemented experimentally. Torres et al [65] demonstrated theoretically that using SPDC, arbitrary engineered entangled states in any d-dimensional Hilbert space can be prepared such that the topological information contained in a pump beam can be translated into the amplitudes of the generated entangled quantum states. This chapter is a step in that direction. We employ a non-fundamental Gaussian pump beam for spontaneous parametric down-conversion (SPDC) and analyse how the OAM and angle correlations change as a result.

3.2 Pump shape and SPDC

Within SPDC, a pump beam is usually approximated as a plane wave incident on a nonlinear crystal, which results in the emission of two correlated photons in definite directions. The bulk of the studies in SPDC has concentrated on manipulating these two outgoing photons by letting them pass through polarisers, slits, holograms, and other optical components, to observe various desired quantum effects such as OAM conservation [9], Bell inequalities [36] and full state tomography measurements [103].

Manipulating the pump field is also an interesting enterprise, as the fields generated in SPDC are strongly related to the pump field; this has been investigated theoretically and

experimentally [9; 98; 107]. The ratio of the pump waist to the signal (idler) waist has been shown to have a significant effect on the measured spiral bandwidth, where a larger ratio produced a wider bandwidth but with reduced coefficient amplitudes (for a Gaussian pump mode) [98]. A similar effect has also been observed in the radial components of Laguerre-Gaussian modes [42].

Phase matching allows the amplitude and phase structure of the pump to be transferred to the two-photon field, and fourth-order images (coincidence measurements from two-photon interference, typically observed in a Hong-Ou-Mandel interferometer [108]) related to the aperture in front of the pump can be formed by the down-converted beams [107]. Focusing the pump beam in front of the crystal leads to two-photon geometric optics effects wherein the crystal acts like a spherical mirror in the formation of the fourth-order images [70]. The shape of the pump is of consequence to correlations in the OAM and the conjugate variable, angular position, in both the signal and idler fields. The transfer of the plane-wave spectrum of the pump to the two-photon field leads to conservation of OAM in both stimulated and spontaneous parametric down-conversion [109; 110; 111; 112]. Thus, for near-collinear SPDC [112], the following selection rule,

$$m = \ell_s + \ell_i, \tag{3.2.1}$$

holds, where $m\hbar$ is the OAM per photon of the pump beam and $\ell_s\hbar$ and $\ell_i\hbar$ are the OAM of the modes into which the signal and idler photons are projected [112; 113; 114]. This has been supported by coincidence measurements in SPDC, wherein the crystal is pumped with Laguerre-Gaussian (LG) beams of varying OAM [9; 112]. The entangled two-photon state generated in this case is

$$|\Psi\rangle = \sum_{\ell=-\infty}^{+\infty} c_\ell |m-\ell\rangle|\ell\rangle. \tag{3.2.2}$$

It is possible to generate other states, such as maximally entangled states with only four modes (in contrast to the infinite OAM spectrum of equation (3.2.2)), by pumping the crystal with a suitable superposition of OAM modes [65], containing a number of phase singularities. This entails the modulation of both the phase and intensity of the pump, and has yet to be achieved experimentally. The first step towards the implementation of such schemes is to have an element which will efficiently convert the fundamental mode of a pump laser to the desired mode for SPDC. Several experiments [9; 112] have performed this mode con-

version with cylindrical lenses or holograms. The latter, when encoded in a spatial light modulators (SLM) are flexible and make possible complicated pump shapes, but they are less efficient than other converters, with an efficiency of about 40%-50% [115]. Simple pump shapes could instead be implemented with simple mode converters. For instance, HG modes can be created by placing one to two wires inside a laser cavity [116]. We do not have access to the laser cavity of our pump laser, so instead we use a cover slip that introduces a π-phase shift to half of the area of the usual Gaussian output of a laser beam. Pump modes have been converted to HG modes using cover slips to generate a two-photon singlet beam (where both photons propagate in the same beam) [117] and to demonstrate non-Gaussian entanglement [118]. The π-phase shift introduces a phase-flip to one half of the beam, hence the name "flipped mode" [119]. Following [119], the flipped mode $u_{f,0}$ is the fundamental Gaussian mode with a phase flip at $x = 0$. This can be expressed as an infinite sum of odd Hermite-Gauss (HG) modes $u_{2n+1}(x)$,

$$u_{f,0} = \sum_{n=0}^{\infty} c_{2n+1} u_{2n+1}(x) \tag{3.2.3}$$

where

$$c_{2n+1} = \frac{(-1)^n (2n)!}{n!\sqrt{\pi 2^{2n-1}(2n+1)!}}, \tag{3.2.4}$$

giving $\sqrt{2/\pi} \approx 0.80$ as the contribution of the first-order HG_{10} mode. Since the LG modes form a convenient basis for OAM-carrying beams, it is instructive to express $u_{f,0}$ in terms of Laguerre polynomials L_k^j [120; 121],

$$\begin{aligned} u_{f,0} \quad = \quad & \sum_{n=0}^{\infty} \sum_{p=0}^{n} a_{np} \exp\left(-\left(\frac{r}{\omega}\right)^2\right) \left(\frac{\sqrt{2}r}{\omega}\right)^{|2(n-p)+1|} \\ & \times L_p^{2(n-p)+1}\left(2\left(\frac{r}{\omega}\right)\right) \left(\exp\left(i(2(n-p)+1)\right) + \exp\left(-i(2(n-p)+1)\right)\right) \end{aligned} \tag{3.2.5}$$

where $a_{n,p}$ is

$$a_{n,p} = (-1)^{n+p} \sqrt{\frac{8}{\pi}} \frac{(2n)!}{(2n+1)!} \frac{(n+1/2)!}{2p!} \frac{2p!}{\pi(p+(2(n-p)+1))!}$$

Hence, only the odd LG modes contribute. A table of the decomposition in terms of the $\mathrm{LG}^{\ell p}$ modes for $p = 0$ is given below,

Table 3.1: Decomposition of the flipped-mode in terms of the $LG^{\ell p}$ modes.

ℓ	$\langle LG^{\ell,0}\|u_{f,0}\rangle$
±5	$\frac{1}{8}\sqrt{\frac{3}{10\pi}} = 0.0386$
±3	$\frac{-1}{2}\sqrt{\frac{1}{6\pi}} = -0.1151$
±1	$\sqrt{\frac{1}{\pi}} = 0.5642$
0	0

The flipped mode has been used in SPDC to produce singlet states [117] and for demonstrating multimode Hong-Ou-Mandel interference and in the generalisation of genuine non-Gaussian entanglement [118; 122]. Since the combination of OAM states $|1\rangle$ and $|-1\rangle$ make the most significant contributions to the flipped mode, in contrast to the usual Gaussian pump which is in the OAM state $|0\rangle$ [24], we expect different OAM and angle correlations from that in [82]. Specifically, we expect coincidences when $\ell_s + \ell_i$ is odd with the strongest correlations occurring when $\ell_s + \ell_i = \pm 1$.

Just as there is a Fourier relationship between position and linear momentum, there also exists a Fourier relationship between OAM and angle [33]. This allows us to determine the correlations in the angular position basis given that we have knowledge of the OAM components of the entangled photons.

3.3 Experiment and results

Our SPDC setup (Fig. 3.1) consisted of a mode-locked ultraviolet (UV) pump source at 355 nm with 100 MHz repetition rate. A cover slip was attached to a tip-tilt mount to control the phase introduced to the pump and placed on a translation stage positioned such that it covered half of the UV beam. The output of the laser was collimated by a telescope onto a 5 mm long barium borate (BBO) crystal, cut for degenerate type- 1, collinear SPDC. The front plane of the crystal was imaged (L1=200 mm, L2=400 mm) onto two separate SLMs, which specify the state into which the photon will be projected. Both SLMs were re-imaged (L3=600 mm, L4=3.2 mm), through 10-nm wide interference filters(IF) to the input facets of single mode optical fibres coupled to single-photon avalanche photodiodes. The coincidence was monitored from the output of the photodiodes by a coincidence counting card with a gate time of 10 ns.

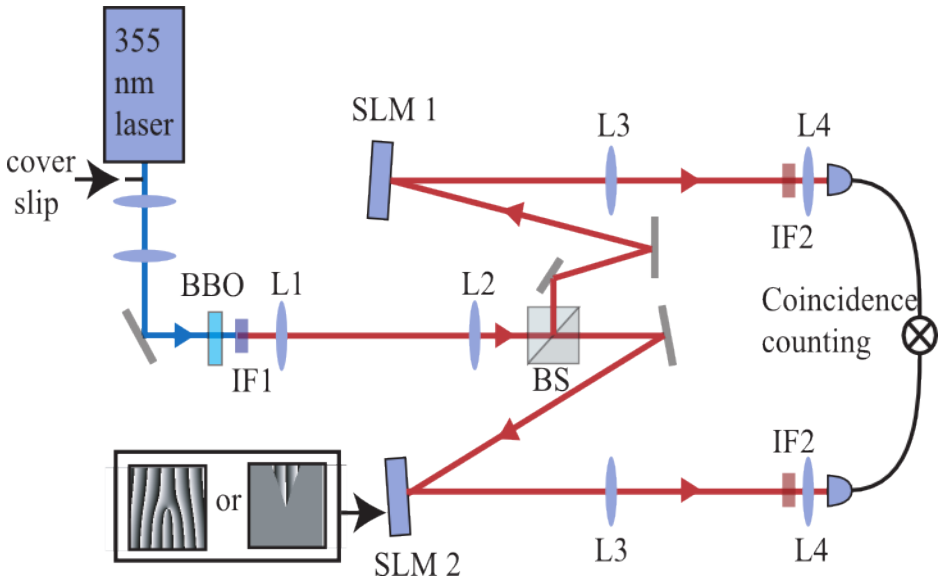

Figure 3.1: Experimental setup for spontaneous parametric down-conversion. The pump is shaped by a cover slip thereby introducing a π-phase shift to half of the outputted Gaussian beam. The orbital angular momentum or angular position of signal and idler photons are measured by programming the spatial light modulator with either a forked diffraction grating or an angular slit respectively.

To measure OAM, each SLM displayed a hologram with a fork dislocation of order ℓ_s and ℓ_i corresponding to the OAM states $|\ell_s\rangle$ and $|\ell_i\rangle$. The pump beam consisted of superpositions of odd-valued OAM states, with $|1\rangle$ and $|-1\rangle$ making the largest contribution [24]. Hence following the selection rule (3.2.1) , we expected high coincidences when the sum of ℓ_s and ℓ_i was ± 1, as shown in Fig. 3.2 (a). We expected two diagonals symmetric about the main diagonal, in contrast to SPDC with a fundamental Gaussian pump wherein there is only one main diagonal [82]. Figure 3.2 (b) shows the coincidences, as a function ℓ_s and ℓ_i, that we obtained from the experiment. Apart from a uniform background (we did not do any background subtraction in our results), and residual on-axis coincidences (due to the imperfect conversion of the pump laser output to a "flipped mode" there is good qualitative agreement between Fig. 3.2 (a) and (b), showing the transfer of the pump OAM spectrum to the entangled photons.

To measure angular position, we employ angular slits of width $\Delta\theta$ which are oriented at positions ϕ_s and ϕ_i in the signal and idler SLMs respectively (see Fig. 3.2 (b)). We can get the expected angular position correlations from the Fourier relationship, by performing a Fourier transform on Fig. 3.2 (a), we obtain Fig. 3.2 (b). Because the SLMs are on the

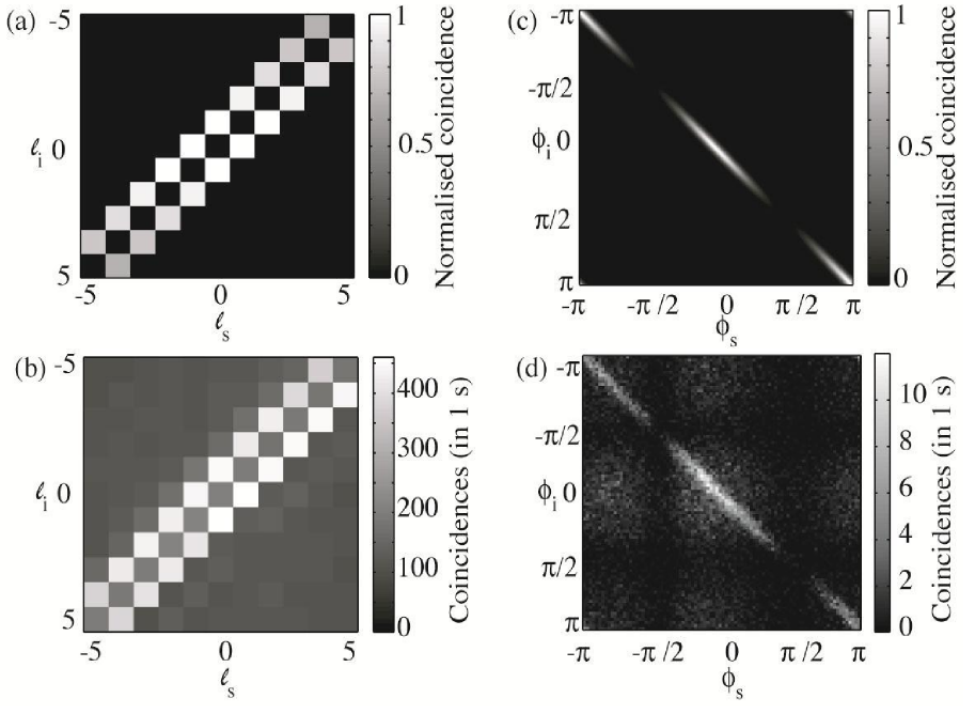

Figure 3.2: Orbital angular momentum (OAM) and angular position correlations. Since the pump is in a superposition of odd OAM states, with $|1\rangle$ and $|-1\rangle$ making the largest contribution, from theory, we expect the coincidences to be high when $\ell_s + \ell_i = \pm 1$ (a). Apart from an almost uniform background (there is no background subtraction in this result), this is supported by the OAM correlations we obtain from our experiment (b). The angular position correlations also reflect the shape of the pump, and in theory can be obtained via the Fourier relationship between OAM and angular position. From the OAM correlations in (a), we expect the modulated coincidence in (c). Coincidence is high along the diagonal when $\phi_s = \phi_i$, but with minima corresponding to the position of the phase discontinuity in the pump. Apart from some background counts, our experiment results support this (d).

image plane of the crystal, we expect the coincidences to be high for $\phi_s = \phi_i$. In addition, due to the shape of the pump, we see a modulation wherein there are coincidence minima corresponding to the case when the slit is aligned with the phase discontinuity in the pump. Figure 3.2 (d) shows the coincidence count as a function of the angular positions ϕ_s and ϕ_i. There is good qualitative agreement between Fig. 3.2 (c) and (d), apart from an almost uniform background (we did not do any background subtraction).

We focused on a simple pump shape, but more complicated modes are possible with combinations of cover slips (for HG pump modes), specially fabricated components or programmable spatial light modulators.

3.4 Conclusion

We have shown the effect of the pump shape on OAM and angle correlations exhibited by photon pairs from spontaneous parametric down-conversion. We focused on a particularly simple OAM superposition state, but more complicated pump shapes such as the vortex pancakes suggested in [65] can be used for tailored entangled states. The correlations that arise result from the transfer of the OAM spectrum of the pump to the down-converted photon pairs, as manifested in the OAM correlation matrix. We have shown a modulation in the angular position correlation which is consistent with the Fourier relationship between OAM and angle. The spatial structure of down-converted light is a rich playground to observe correlations in a variety of spatial modes, not just OAM. If efficiency is not a priority, spatial light modulators can be introduced not just in the measurement, but also in the generation of entangled photons. With the flexibility afforded by spatial light modulators, different pump modes can be used to prepare the entangled states, and in addition to current developments in sorting OAM states [123] and gates with OAM [124], this will certainly be a step forward to fully exploring a d-dimensional space for quantum information.

Chapter 4

Bessel-Gaussian entanglement

In this chapter we consider geometrical two-photon optics of Bessel-Gaussian (BG) modes generated in spontaneous parametric down-conversion of a Gaussian pump beam. We provide a general theoretical expression for the orbital angular momentum (OAM) spectrum and Schmidt number in this basis and show how this may be varied by control over the radial degree of freedom, a continuous parameter in BG modes. As a test we first implement a back-projection technique to classically predict, by experiment, the quantum correlations for BG modes produced by three holographic masks, a blazed axicon, a binary axicon and a binary Bessel function. We then proceed to test the theory on the down-converted photons using the binary Bessel mask. We experimentally quantify the number of usable OAM modes and confirm the theoretical prediction of a flattening in the OAM spectrum and a concomitant increase in the OAM bandwidth. We demonstrate OAM entanglement in the BG basis by performing a Bell-type experiment and showing a violation of the Clauser-Horne-Shimony-Holt inequality for the $\ell = \pm 1$ subspace. In addition, we use quantum state tomography to indicate higher-dimensional entanglement in terms of BG modes.

4.1 Introduction

The spontaneous parametric down-conversion (SPDC) process has been shown to conserve orbital angular momentum (OAM) when pumped with either a fundamental Gaussian mode [9] or a non-fundamental mode [41]. The implication thereof is that a pair of down-converted photons are naturally entangled in terms of the OAM eigenstates. The Laguerre-Gaussian (LG) modes are often approximated to include only the azimuthal phase term, hence they are also called helical modes. The radial components of the LG modes are often ignored as they require complex amplitude modulation (intensity masking) [44; 125]. That is, a phase-only spatial light modulator (SLM) is used to modulate both the phase and amplitude of the incident beam by first numerically calculating the required intensity distribution and adding it to the required phase distribution [44].

By approximating the phase matching condition with a Gaussian function, it was shown [34] that the Schmidt basis for the quantum state produced in SPDC is the LG modes, that is, the Schmidt basis is a basis of OAM eigenstates. Without this approximation, the LG modes are still close to being the Schmidt basis[34; 42]. Thus, the LG modes are not only entangled in the azimuthal index, but also in terms of the radial index [43].

High-dimensional entanglement is dependent on the number of usable OAM modes in the state [65]. The need for increased information capacity per photon in most quantum information processes has caused researchers to focus their efforts into increasing the number of accessible OAM modes (spiral bandwidth) in quantum entanglement [39; 40; 42; 105]. One technique focuses on the width of the pump beam and the length of the non-linear crystal [39], where it was theoretically shown that the spiral bandwidth could be increased by either decreasing the length of the crystal or by increasing the size of the pump mode. A similar conclusion was made by Miatto *et al.* [42], where they provided a complete characterisation of the spiral bandwidth measured in the Laguerre-Gaussian basis. The beam widths of the pump, signal and idler were set as free parameters as well as the azimuthal ℓ and radial indices p. One can also use the phase-matching condition to widen and flatten the OAM spectrum [105]. Altering the tilt of the crystal, causes a phase mismatch such that a variation of approximately 1/20 of a degree doubled the experimentally measured spiral bandwidth [105]. In each of these techniques, the OAM spectrum was investigated in the LG basis, with the experimental studies using only the helical modes. The experimental

parameters (e.g. mode size of single-mode fibre) involved in the detection of the spectrum of helical modes place restrictions on the control one has over the bandwidth of OAM components in the entangled state.

Although the connection between the spatial modal profile of an optical beam and OAM was initially made with specific reference to LG beams [23], the same property applies to any optical beam with a rotationally symmetric intensity profile. Higher-order Bessel beams [126; 127] and Bessel-Gaussian (BG) beams [128] also have helical wavefronts and carry OAM. In 2001, transparent, spherical particles were made to rotate around the central axis within the inner ring of a BG beam, a clear demonstration of the mechanical transfer of OAM [28].

In this chapter we outline experimentally and theoretically how the BG modes may be used to increase the dimensionality of entangled states. To do so we provide a thorough description of the two-photon 'geometric optics' [75] of BG modes entangled in the OAM basis. The radial index associated with LG modes is replaced by a continuous scaling parameter for the radial part of the BG modes. We use classical back-projection as an experimental tool to study BG projective measurements, and show that we are able to predict the strength of the coincidence correlations in the entanglement experiment. We quantify the number of measurable OAM modes by calculating the Schmidt number, and demonstrate a clear dependence of the dimensionality on the radial component, in agreement with theory. We also compare the high-dimensional density matrices measured in the BG basis to those measured in the helical basis. Our results indicate that under the correct experimental conditions, the generation and measurement of high-dimensional entanglement in the BG basis is advantageous compared to the helical basis.

4.2 Theory

4.2.1 Bessel-Gaussian Modes

The electric field of a BG mode is given by

$$E_\ell^{\mathrm{BG}}(r,\phi,z) = \sqrt{\frac{2}{\pi}}\mathrm{J}_\ell\left(\frac{z_R k_r r}{z_R - iz}\right)\exp(i\ell\phi - ik_z z)\exp\left(\frac{k_r^2 z w_0^2 - 2kr^2}{4(z_R - iz)}\right) \tag{4.2.1}$$

where ℓ is the azimuthal (mode) index (a signed integer); $\mathrm{J}_\ell(\cdot)$ is the Bessel function of the first kind; k_r and k_z are the transverse and longitudinal wave numbers, respectively. The

initial radius of the Gaussian profile is w_0 and the Rayleigh range is $z_R = \pi w_0^2/\lambda$. It is clear from Eq. (4.2.1) that the radial component of the mode can be scaled by altering k_r.

The quantum state for the photon pairs produced in SPDC can be written in terms of BG modes,

$$|\Psi\rangle = \sum_{\ell} \int\int a_\ell(k_{r1}, k_{r2}) \, |\ell, k_{r1}\rangle_s \, |-\ell, k_{r2}\rangle_i \, \mathrm{d}k_{r1} \mathrm{d}k_{r2}, \tag{4.2.2}$$

where $|a_\ell(k_{r1}, k_{r2})|^2$ denotes the probability for measuring a signal photon in state $|\ell, k_{r1}\rangle_s$ and an idler photon in state $|-\ell, k_{r2}\rangle_i$. In an experiment the radial scaling parameters k_{r1} and k_{r2} in Eq. (4.2.2) can be selected and adjusted in a continuous manner (see 4.3) to optimize the bandwidth of the OAM spectrum.

If instead of integrating over k_{r1} and k_{r2} we select particular values, then the two-photon state for d dimensions can be written as

$$|\Psi(k_{r1}, k_{r2})\rangle = \sum_{\ell} c_\ell \, |\ell\rangle_s \, |-\ell\rangle_i \, , \tag{4.2.3}$$

where ℓ ranges over d different values and c_ℓ represents the expansion coefficients. The sets of ℓ-values for different dimensions d are chosen as before in Sec. 2.4.3 [97]. Note that while the state after the SPDC process is anticorrelated in ℓ and thus spans d dimensions, the full state space has d^2 dimensions, because it also contains products of differing ℓ-values.

We recall the density matrix of a two-photon qu*d*it quantum state as,

$$\rho = \sum_{m,n=0}^{d^2-1} b_{m,n} \tau_m \otimes \tau_n, \tag{4.2.4}$$

where $b_{m,n}$ are complex coefficients with $b_{0,0} = 1/d^2$ for normalisation; τ_p are the d-dimensional generalised Gell-Mann matrices for $p = 1 \ldots (d^2 - 1)$; τ_0 is the d-dimensional identity matrix. These coefficients are determined by performing a tomographically complete set of measurements. As in the LG case in Sec. 2.4.3, we choose an over-complete set of measurements to compensate for measurement errors due to natural photon number fluctuations. An example of an over-complete set consists of the pure BG states $|\ell, k_r\rangle$ together with the superpositions of two BG states

$$|\theta\rangle = \frac{1}{\sqrt{2}} \left[|\ell_1, k_r\rangle + \exp(i\theta) |\ell_2, k_r\rangle \right]. \tag{4.2.5}$$

Here, θ is the phase between the modes of the superposition states and k_r is chosen as a fixed value for all basis states.

4.2.2 Schmidt number

The probability for the biphoton quantum state after the SPDC process to contain a particular measurement state $\rho_{\mathrm{m}} = |\Psi_s\rangle |\Psi_i\rangle \langle\Psi_s| \langle\Psi_i|$, is given by the trace $\mathrm{Tr}\{\rho\rho_{\mathrm{m}}\} = |\mathscr{M}|^2$, where $\mathscr{M}$ is the scattering amplitude. For monochromatic paraxial pump, signal and idler beams in a degenerate collinear SPDC process with type I phase matching, the scattering amplitude is given by [42]

$$\mathscr{M} = \Omega_0 \int M_s^*(\mathbf{K}_1) M_i^*(\mathbf{K}_2) M_p(\mathbf{K}_1 + \mathbf{K}_2) P(\Delta k_z) \frac{\mathrm{d}^2 k_1}{(2\pi)^2} \frac{\mathrm{d}^2 k_2}{(2\pi)^2}, \tag{4.2.6}$$

where $M_s(\mathbf{K})$, $M_i(\mathbf{K})$ and $M_p(\mathbf{K})$ are the Fourier spectra of the two-dimensional mode profiles for the signal, idler and pump beams, respectively; $\mathbf{K}$ represents the coordinate vector in the two-dimensional transverse Fourier domain; Ω_0 is a constant that determines the overall conversion efficiency; and $P(\Delta k_z)$ is a function that represents the phase matching condition.

The phase matching condition is given in terms of a sinc-function

$$P(\Delta k_z) = \mathrm{sinc}\left(\frac{\Delta k_z L}{2\pi}\right) = \mathrm{sinc}\left(\zeta |\mathbf{K}_1 - \mathbf{K}_2|^2\right), \tag{4.2.7}$$

where

$$\zeta = \frac{n_o \lambda_p L}{8\pi^2}, \tag{4.2.8}$$

with n_o being the ordinary refractive index of the non-linear crystal, λ_p being the wavelength of the pump and L being the crystal length. Assuming the pump wavelength is much smaller than any of the other dimension parameters, the width of the sinc-function in Eq. (4.2.8), as determined by $\zeta^{-1/2}$, is much larger than the widths of the angular spectra of the pump, signal or idler beams [65]. Hence, one can approximate $P = 1$ and the Fourier integral in Eq. (4.2.6) can be transformed into a spatial domain given by

$$\mathscr{M} = \Omega_0 \int m_s^*(\mathbf{x}) m_i^*(\mathbf{x}) m_p(\mathbf{x}) \mathrm{d}^2 x, \tag{4.2.9}$$

where $m_s(\mathbf{x})$, $m_i(\mathbf{x})$ and $m_p(\mathbf{x})$ are the two-dimensional mode profile functions for the signal, idler and pump beams, respectively. The pump beam has a mode profile described by a Gaussian function, which is expressed as

$$m_p = \frac{1}{\omega_0} \sqrt{\frac{2}{\pi}} \exp\left[-\frac{(x^2 + y^2)}{\omega_0^2}\right], \tag{4.2.10}$$

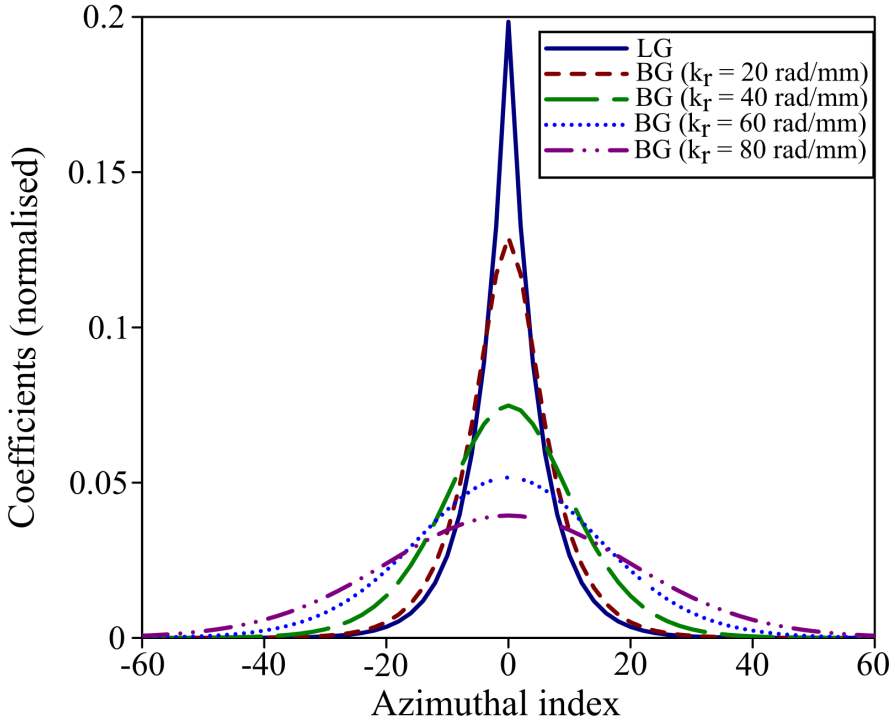

Figure 4.1: Comparison of the orbital angular momentum (OAM) spectra for the helical modes ($k_r = 0$) and Bessel-Gaussian modes ($k_r = 20, 40, 60, 80$ rad/mm) using Eqs. (4.2.14) and (4.2.13), respectively, with $\omega_0 = 0.5$ mm and $\omega_1 = 0.23$ mm. The number of usable OAM modes increases with the radial wavevector k_r.

where the radius of the mode profile of the pump beam is given by ω_0. We consider the case where the signal and idler beams are BG modes with azimuthal indices ℓ and $-\ell$, respectively, and with scaling parameters k_{r1} and k_{r2}, respectively. For simplicity we assume that $k_{r1} = k_{r2} = k_r$. A BG mode with a specific ℓ-value is produced by evaluating the following integral,

$$M_\ell^{\mathrm{BG}} = \frac{1}{2\pi}\int_0^{2\pi} \mathscr{G}\exp(-i\ell\beta)\,\mathrm{d}\beta. \tag{4.2.11}$$

The generating function, $\mathscr{G}$ for BG modes at $z = 0$ is then given by

$$\mathscr{G} = \sqrt{\frac{2}{\pi}}\frac{1}{\omega_1}\exp\{ik_r[y\cos(\beta) - x\sin(\beta)]\}\exp\left[-\frac{(x^2+y^2)}{\omega_1^2}\right], \tag{4.2.12}$$

where the radius of the Gaussian envelope of the mode is ω_1 and β is an angular generating parameter.

The coefficients for any given value of the azimuthal index ℓ (with opposite signs for the signal and idler beams, respectively) can be extracted by substituting Eq. (4.2.10) and Eq. (4.2.12) into Eq. (4.2.9), and solving the integral. The OAM spectrum, represented

by these coefficients, is given by

$$C_\ell = (-1)^\ell \sqrt{\frac{2}{\pi}} \frac{2\Omega_0 \omega_0^2}{2\omega_0^2 + \omega_1^2} \times \exp\left[\frac{-k_r^2 \omega_1^4}{4(2\omega_0^2 + \omega_1^2)}\right] \frac{I_\ell\left[\frac{k_r^2 \omega_0^2 \omega_1^2}{2(2\omega_0^2 + \omega_1^2)}\right]}{I_\ell\left[\frac{k_r^2 \omega_1^2}{4}\right]}, \tag{4.2.13}$$

where $I_\ell(\cdot)$ is the modified Bessel function of the first kind [121]. The equivalent coefficients in the helical basis, for zero radial index, are given by

$$C_\ell = \Omega_0 \sqrt{\frac{2}{\pi}} \left(\frac{2\omega_0^2}{2\omega_0^2 + \omega_1^2}\right)^{|\ell|+1}. \tag{4.2.14}$$

An estimate of the OAM bandwidth of this spectrum can be calculated by computing the azimuthal Schmidt number [34] given by

$$K = \frac{\left(\sum_\ell C_\ell^2\right)^2}{\sum_\ell C_\ell^4}. \tag{4.2.15}$$

In the case where the OAM spectrum is computed in terms of the BG modes, one cannot obtain a closed form expression for the azimuthal Schmidt number. However, one can compute the azimuthal Schmidt number numerically from the analytical result in Eq. (4.2.13) for any given value of k_r. Figure. 4.1 shows the OAM spectra for the helical and BG modes. In the case where Eq. (4.2.7) is not approximated as 1, the OAM spectra are partly determined by the length of the non-linear crystal [66].

4.3 Back-projection results

Using the Klyshko picture introduced in Sec. 2.3.1, we initially used the method of back-projection to study three different methods of generating BG modes. We consider blazed axicons, which have been well documented for producing Bessel-Gauss beams, binary axicons and binary Bessel functions.

OAM entanglement is typically measured in the LG basis by encoding only the azimuthal phase term onto an SLM, described by the transmission function:

$$T(\phi) = \exp(i\ell\phi), \tag{4.3.1}$$

where ϕ is the azimuthal angle. Depending on the azimuthal index ℓ an incoming Gaussian mode is transformed into an approximated LG mode carrying OAM of $\ell\hbar$ per photon. This

is only an approximation as the radial dependence of the LG function has been neglected in favour of efficiency [42; 43]. By selecting the BG basis in which to measure OAM entanglement, we have access to a continuous scaling parameter for the radial component of the BG modes.

4.3.1 Blazed axicon

The first phase pattern investigated was that of an axicon described by a blazed (kinoform element) function, first described by Turunen *et al.* [129]. The conversion from Gaussian to BG mode was performed using the phase-only hologram of an axicon described by the transmission function

$$T_1(r,\phi) = \exp(ik_r r)\exp(i\ell\phi), \tag{4.3.2}$$

where k_r is the radial wavevector and ℓ is the azimuthal index. The number of rings of the BG beam increases with k_r. A blazed grating is added to separate the diffraction orders so that this kinoform diffracts approximately 100% of the incoming light into the first diffraction order. Figure 4.2(a) shows an example of such a phase pattern for $k_r = 21$ rad/mm and $\ell = 1$. By placing a CCD camera (aligned to the first diffraction order) in the plane of the crystal, we were able to view the mode at this plane, corresponding to the detected mode. The shape of the beam imaged from the SLM (blazed axicon) for $k_r = 21$ rad/mm and $\ell = 1$ is shown in Fig. 4.2(b). Figure 4.2(c) shows the experimental measurements of the single counts measured at detector B. The counts recorded show a strong correlation along the diagonal corresponding to values of k_r of equal magnitude but opposite sign. The single counts level was significant only when the system consisted of a positive radial wavevector k_r on one SLM with the corresponding negative radial wavevector $-k_r$ on the other (although the radial wavevector is a positive entity, we assign a negative value to k_r to represent the conjugate phase). This translates to a positive axicon imaged onto a negative axicon, to produce a Gaussian beam, which is analogous to the lens functions discussed in Sec. 2.3.1. As k_r is a continuous variable, we expected a gradual decrease in the count rate moving away from the diagonal elements. The OAM correlations for a particular blazed axicon function are shown in Fig. 4.2(d). We note that the recorded mode [Fig. 4.2(b)] does not exhibit a well-defined BG beam, since this is only fully formed (maximum number of rings) at a distance z_0 after the SLM (blazed axicon). This is more clearly illustrated in

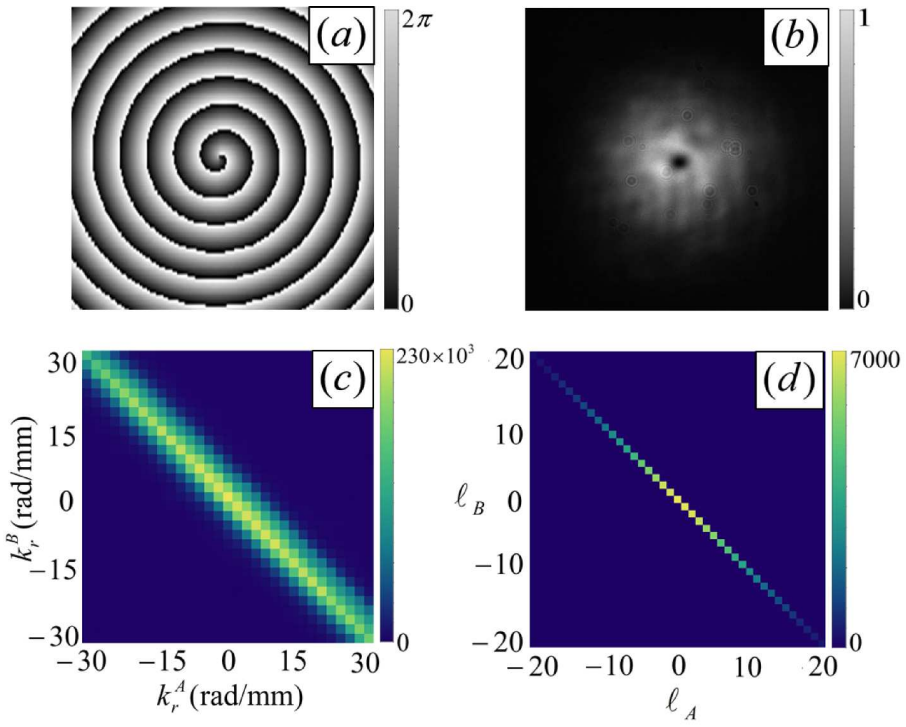

Figure 4.2: (a) Phase pattern used to define an axicon of $k_r = 21$ rad/mm and $\ell = 1$. (b) CCD image of a Bessel-Gaussian beam generated from a blazed axicon function of $k_r = 21$ rad/mm and $\ell = 1$ at the plane of the crystal. (c) Density plot of the single count rates measured in back-projection for different blazed axicon phase patterns; varying k_r with $\ell = 0$. (d) Density plot of the single count rates measured in back-projection for a particular blazed axicon; $k_r = 21$ rad/mm and varying ℓ.

Fig. 4.3(a), where we depict an axicon illuminated with a Gaussian beam, analogous to the back projected light from the fibre (Gaussian source) illuminating the SLM (axicon). Immediately after the axicon the conical waves have not sufficiently overlapped to create a Bessel beam, so plane (1) is a Gaussian-like beam. If a spiral phase is added to the axicon, then one observes a Gaussian-like beam with a central null, as shown in the adjacent inset. Only at plane (2), where the interfering conical waves overlap completely would a BG beam with a maximum number of rings be generated. However this is some distance from the axicon. The implication is that when the SLM is programmed with a blazed axicon, and this plane is imaged to the crystal, one can never detect true BG modes.

4.3.2 Binary axicon

One can question whether the OAM modes are truly measured in the BG basis with a blazed axicon, as the image at the crystal plane did not resemble a Bessel beam. This issue can

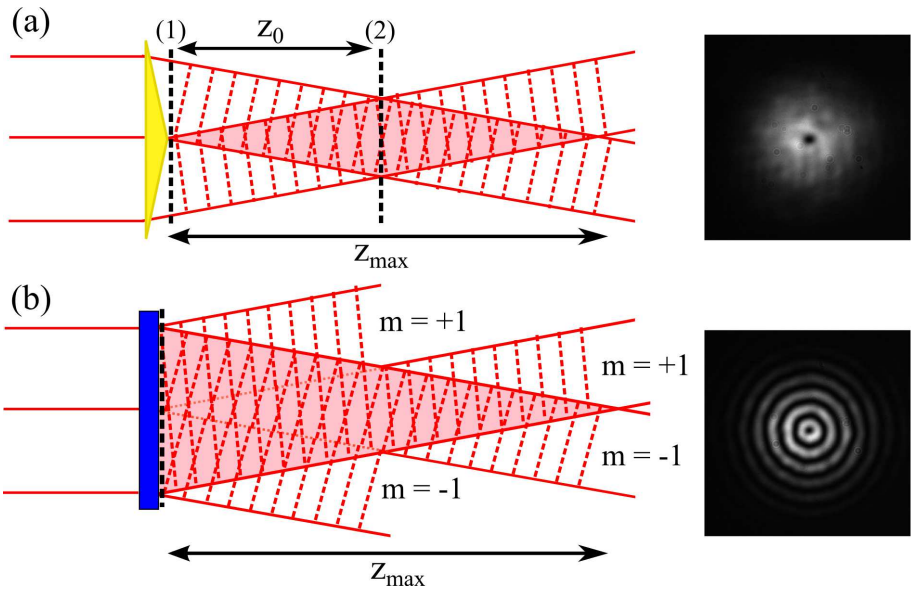

Figure 4.3: (a) Formation of a Bessel-Gaussian (BG) beam by directing a Gaussian beam on a standard axicon. No rings are seen in the plane of the dotted line (1) (corresponding to the plane immediately after the spatial light modulator (SLM)) as the BG beam has not yet formed. At plane (2) the interfering plane waves produce a well-defined BG beam after propagating a distance z_0. (b) Formation of a Bessel-Gaussian mode by directing a Gaussian beam on a binary axicon. A BG-like beam is observed immediately after the SLM due to the interference of the diffraction orders, $m = \pm 1$, of the binary hologram.

be remedied by using a different approximation to an axicon function. That is, the second phase pattern studied also incorporated the axicon function, but as a binary function:

$$T_2(r,\phi) = \text{sign}\{\exp(ik_r r)\}\exp(i\ell\phi), \tag{4.3.3}$$

where $\text{sign}\{z\} = z/|z|$. The kinoform used to approximate an axicon in the previous subsection was replaced with a two-level binary approximation. The efficiency of a kinoform DOE into the first diffraction order is almost 100%, while the efficiency of a binary function is about half that; 42% in both the $m = \pm 1$ diffraction orders. This effect has an advantage in that a Bessel-like beam forms immediately after the SLM. Figure 4.3(b) illustrates a Gaussian beam incident on an SLM encoded with the binary axicon function described in Eq. (4.3.3). The binary axicon hologram deflects both diffraction orders symmetrically such that the plane waves interfere with each other and produce a Bessel-like region immediately after the SLM, i.e. at $z_0 = 0$. This results in a well-defined BG mode directly after the SLM, shown in the inset of Fig. 4.3(b). By filtering the higher diffraction orders using a variable aperture (see experimental setup in Sec. 4.4), a clear image of a BG mode was recorded at

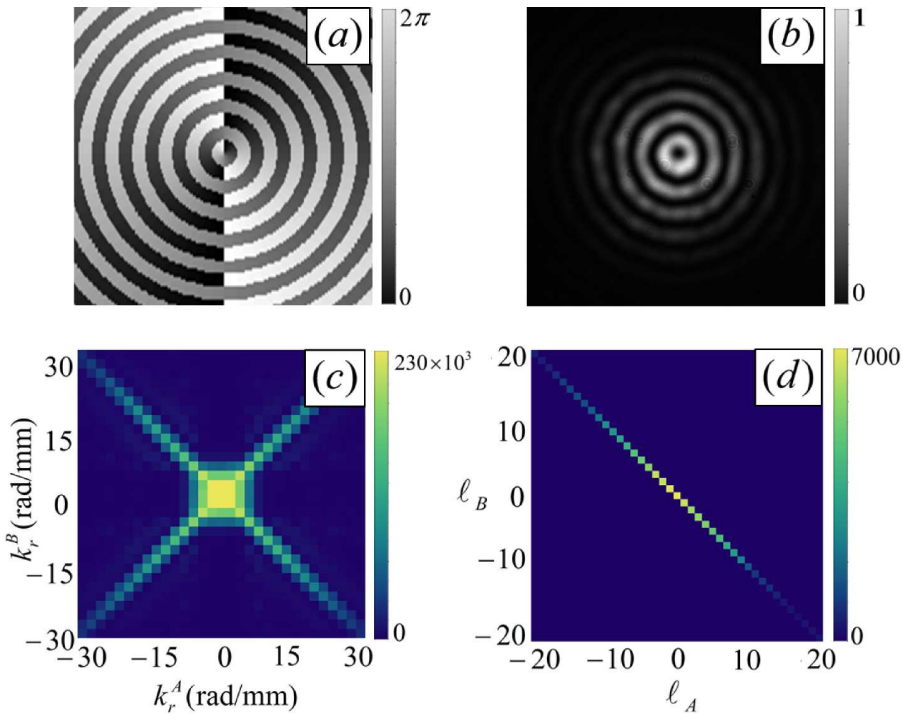

Figure 4.4: (a) Phase pattern at the plane of the spatial light modulator (SLM) to define a binary axicon of $k_r = 21$ rad/mm and $\ell = 1$. (b) Bessel-Gaussian (BG) beam formed at the plane of the mirror (crystal) by a binary axicon function of $k_r = 21$ rad/mm and $\ell = 1$ with a Gaussian input. (c) Density plot of the single count rates measured in back-projection for different binary axicon phase patterns; varying k_r with $\ell = 0$. The photons from SLM A assume a value of either positive or negative k_r from the binary function. SLM B was encoded with the same function, which allowed BG modes of either positive or negative radial wavevectors to be converted to a Gaussian mode. (d) Density plot of the single count rates measured in back-projection for a particular binary axicon; $k_r = 21$ rad/mm and varying ℓ.

the crystal plane, see Fig. 4.4(b).

Similar to the previous case, an incoming Gaussian beam can be converted into a mode with a radial wavevector of either k_r or $-k_r$. The recorded single count rate shown in Fig. 4.4(c) illustrates a distinct difference between the blazed and binary axicon functions. The binary function on SLM A transforms the incoming Gaussian mode into a BG mode with radial wavevector of either k_r or $-k_r$, such that there is an equal probability of generating a photon with a positive or negative k_r value. Subsequently SLM B, encoded with the same function, is also able to convert both BG modes (with wavevector components k_r and $-k_r$) into a Gaussian mode. As a result, single count rates were observed for $k_r^A = k_r^B$ and $k_r^A = -k_r^B$. The OAM correlations for a particular binary axicon function are shown in Fig. 4.4(d).

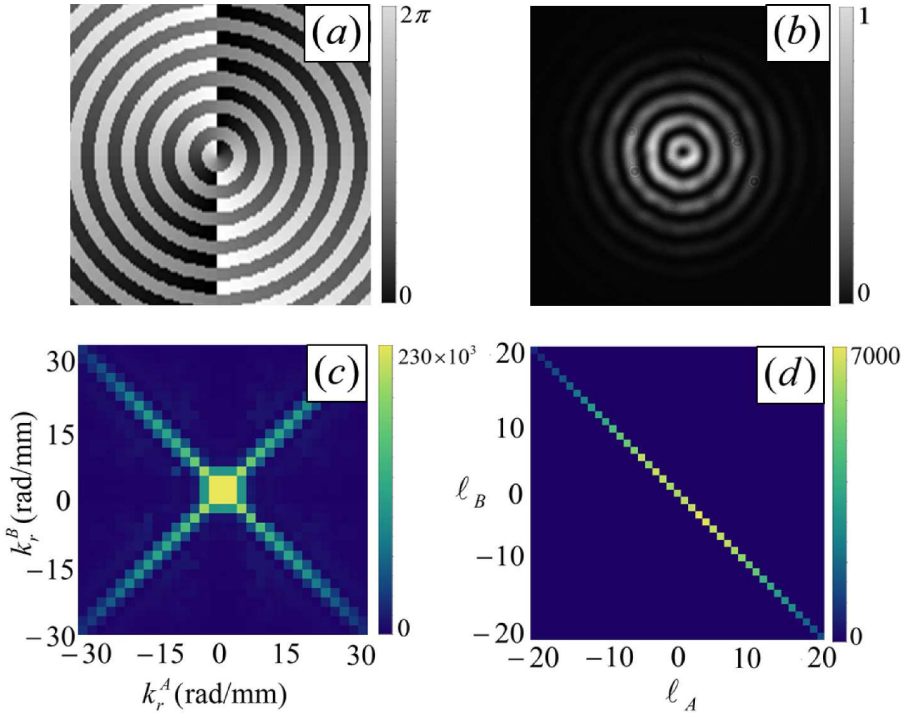

Figure 4.5: (a) Phase pattern at the plane of the spatial light modulator to define a binary Bessel function of $k_r = 21$ rad/mm and $\ell = 1$. (b) Bessel-Gaussian beam formed at the plane of the mirror (crystal) by a binary Bessel function of $k_r = 21$ rad/mm and $\ell = 1$ with a Gaussian input. (c) Density plot of the single count rates measured in back-projection for different binary Bessel phase patterns; varying k_r with $\ell = 0$. (d) Density plot of the single count rates measured in back-projection for a particular binary Bessel function; $k_r = 21$ rad/mm and varying ℓ.

4.3.3 Binary Bessel function

The implementation of the binary axicon function confirmed that we indeed measured BG modes. However, the axicon function acts only as an approximation to the Bessel function. Therefore, the final phase pattern considered was that of a binary Bessel function:

$$T_3(r,\phi) = \text{sign}\{\mathrm{J}_\ell(k_r r)\}\exp(i\ell\phi). \tag{4.3.4}$$

Here $\mathrm{J}_\ell(\cdot)$ is the Bessel function of the first kind. Although very similar to the binary axicon function, Eq. (4.3.4) provides a more accurate description of an ideal Bessel beam. The spacing between the rings of a Bessel beam generated from an axicon remain constant with radial position, while the spaces of a theoretical Bessel beam vary in size as we move radially outward from the centre, and subsequently depend on k_r. The phase pattern and CCD image of a binary Bessel function are shown in Fig. 4.5.

A measurable count rate is again obtained along the diagonal where $k_r^A = \pm k_r^B$. How-

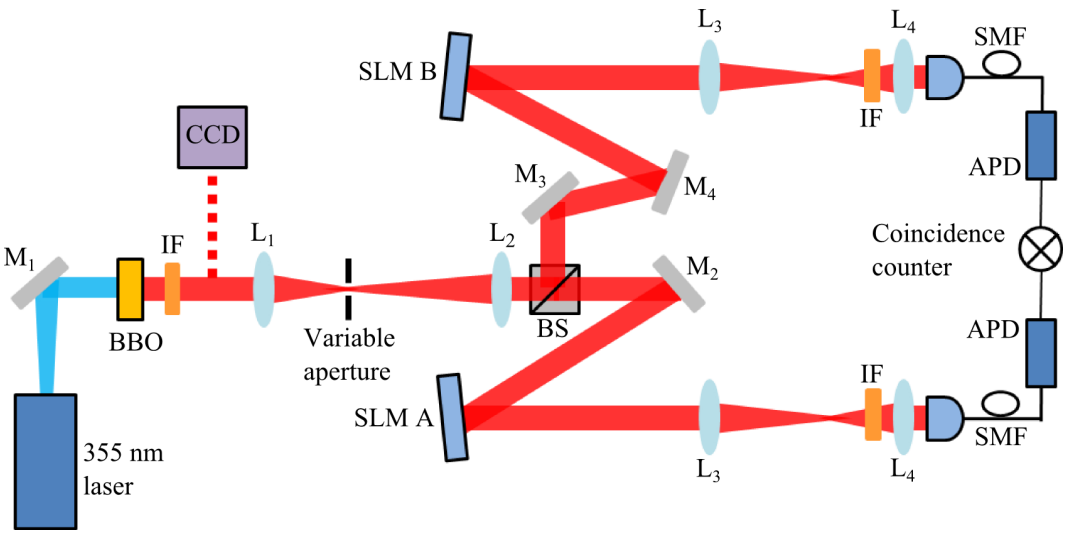

Figure 4.6: Experimental setup used to detect the orbital angular momentum eigenstate after spontaneous parametric down-conversion. The plane of the crystal was relay imaged onto two separate spatial light modulators (SLMs) using lenses, L_1 and L_2 ($f_1 = 200$ mm and $f_2 = 400$ mm), where the Bessel-Gaussian modes were selected. Lenses L_3 and L_4 ($f_3 = 500$ mm and $f_4 = 2$ mm) were used to relay image the SLM planes through 10 nm bandwidth interference filters (IF) to the inputs of the single-mode fibres (SMF).

ever, the off-diagonal crosstalk is now less prominent, when compared with Fig. 4.4(c), particularly surrounding $k_r^{A,B} = 0$. We have generated a BG mode with a better radial approximation, thus creating less overlap between the different radial wavevectors. The OAM correlations for a particular binary Bessel function are shown in Fig. 4.5(d).

4.4 Down-conversion experiment and results

In spontaneous parametric down-conversion (SPDC), a nonlinear crystal pumped with a laser beam generates pairs of entangled photons, which are then separately detected. Our SPDC setup is shown in Fig. 4.6. A mode-locked laser source (Gaussian mode) with a wavelength of 355 nm and an average power of 350 mW was used to pump a 3-mm-thick type I BBO crystal to produce collinear, degenerate entangled photon pairs via SPDC. Using a $4f$ telescope, the plane of the crystal was imaged ($2\times$) onto two separate SLMs which are encoded with the BG transmission functions. The SLM planes were re-imaged ($0.4\times$) by a $4f$ telescope and coupled into single-mode fibres, which support only the fundamental Gaussian mode. The fibres were connected to avalanche photodiodes, the outputs of which were connected to a circuit that gives the coincidence count rate. A comparison was made

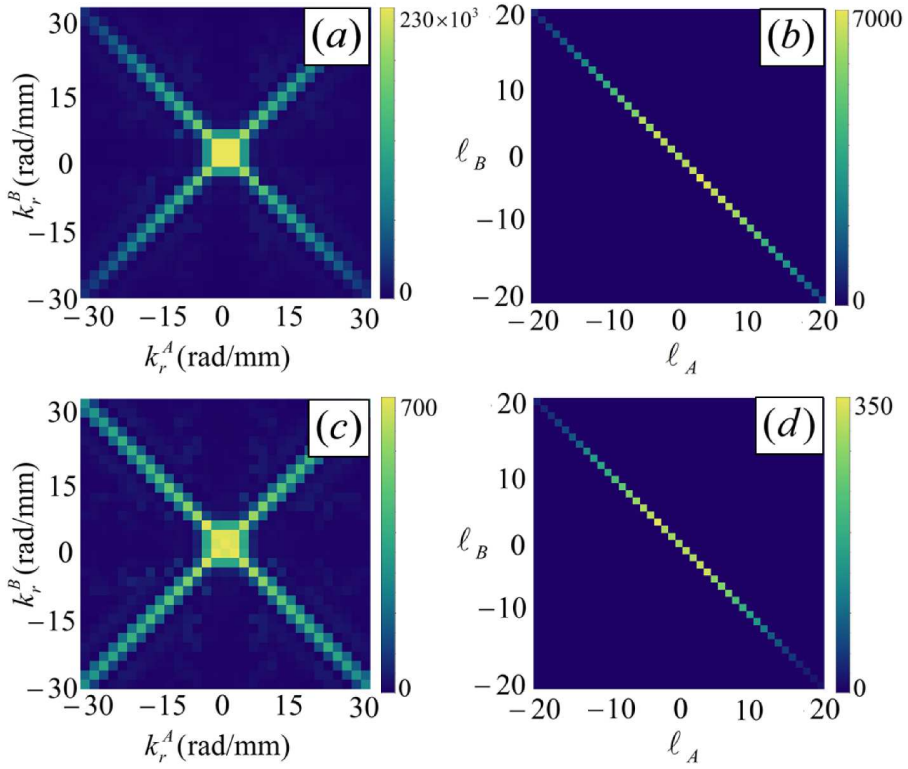

Figure 4.7: Comparison of the measurements recorded in back-projection, (a) & (b), with those taken in down-conversion mode, (c) & (d). Density plots (a) and (c) both illustrate similar patterns for the measurements taken with $\ell = 0$ and varying k_r. The orbital angular momentum correlations are displayed in (b) & (d) for $k_r = 21$ rad/mm.

between the back-projected and down-converted measurements, where we observe that the two methods produce almost identical results for both the radial and azimuthal correlations, see Fig. 4.7. Thus, back-projection provides an effective method in which to qualitatively predict the down-conversion measurements. Ideally, back-projection could be used as a simple technique to fully align the down-conversion system by reflecting the back-projected light off the crystal. However, typically the non-linear crystal is cut in such a way that requires a slight additional vertical tilt to achieve the phase matching conditions for collinear down-conversion [41]. This minute change to the crystal orientation is significant enough to misalign the back-projected beam (i.e. the reflected light does not couple into the other fibre). Thus while we achieved good agreement between the back-projected and down-converted results, we are unable to provide a full quantitative comparison.

The OAM bandwidth (also referred to as the spiral bandwidth) was measured as a function of the different BG phase patterns, and compared with the spiral bandwidth measured

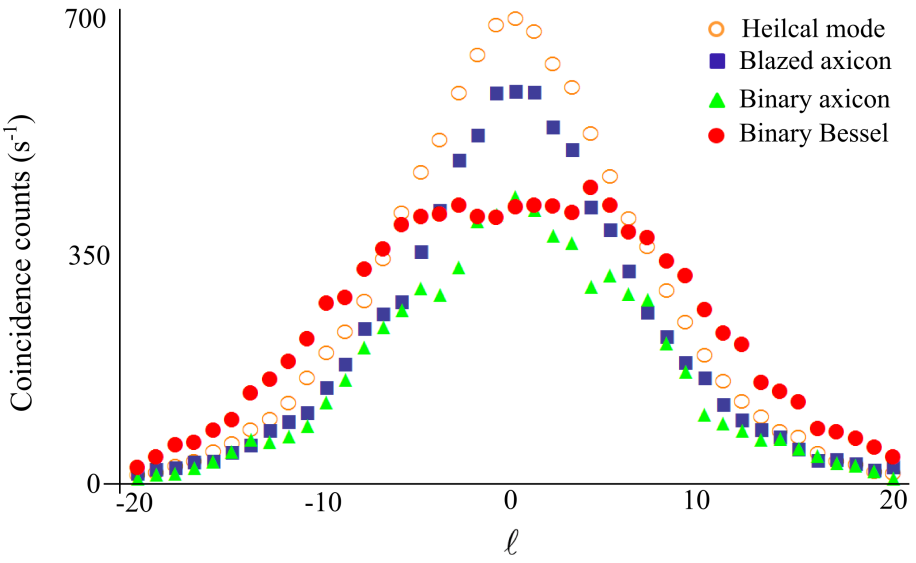

Figure 4.8: Graph of the measured coincidence count rate as a function of orbital angular momentum for four different measurement schemes. The Bessel-Gaussian measurements were all measured for $k_r = 21$ rad/mm. The empty orange circles represent the measurements recorded for helical modes. The blue squares represent the measurements recorded using a blazed axicon function. The binary axicon function is represented by the green triangles and the measurements from the binary Bessel function are illustrated by red circles.

in the helical basis. Due to conservation of angular momentum [9], a coincidence can only be observed for $\ell_A + \ell_B = 0$, where ℓ_A and ℓ_B are the azimuthal indices of the functions encoded in SLM A and B, respectively. These results are shown in Fig. 4.8.

The inefficiency of the binary phase pattern results in a decrease in the count rate for both binary phase patterns. Our results show that the binary Bessel phase pattern produces the largest full-width-half-maximum (FWHM) value of 21. The binary axicon function gave a FWHM value of 17, while both the blazed axicon and vortex functions produced OAM spectra with FWHM values of 15. These graphs were all measured for a particular value of $k_r = 21$ rad/mm.

In investigating the effect of the radial wavevector on the bandwidth, we focused only on the binary Bessel function. Figure 4.9 illustrates the flattening of the OAM spectra when measured in the BG basis. We note that the broadening of the OAM spectrum is at the expense of reducing the coincidence counts at low ℓ values. This in turn decreases the heralding efficiency, which has an effect on the security of quantum key distributions. We found, due to the spatial resolution of the SLMs, that there was a maximum limit for which k_r could be chosen. We therefore varied the radial wavevector from 0 to 35 rad/mm. We compare

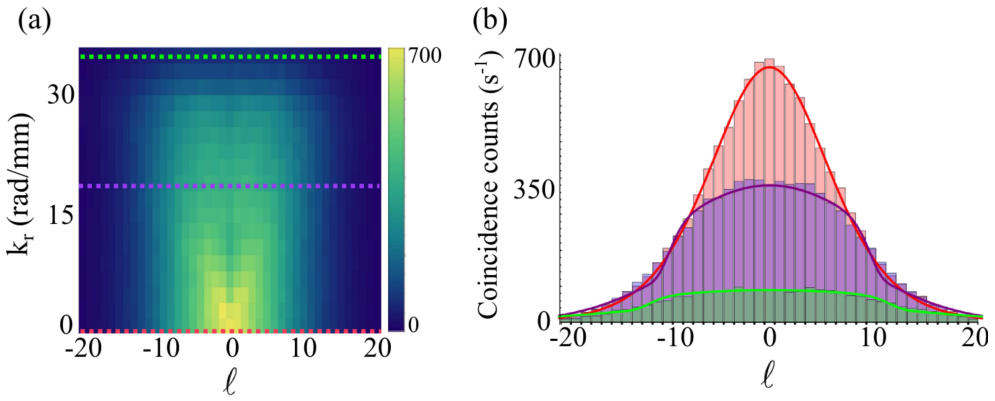

Figure 4.9: (a) Density plot of the modal spectrum in the Bessel-Gaussian basis for k_r and ℓ. The efficiency of the coincidence count rate decreases as k_r, however the full-width-half-maximum of the bandwidth increases with k_r, seen more clearly in (b). The coloured dashed lines in (a) correspond to the profiles plotted in (b) for $k_r = 0$ rad/mm (red), $k_r = 21$ rad/mm (purple) and $k_r = 35$ rad/mm (green).

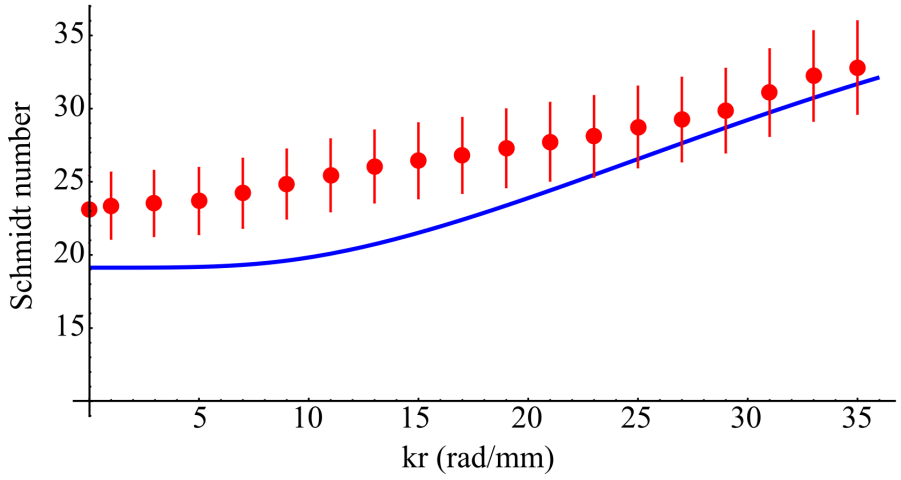

Figure 4.10: Effect of the radial wavevector on the Schmidt number. For $k_r = 0$, the transmission function corresponds to that of a vortex mode. An increase in the number of available orbital angular momentum modes is observed as the radial component is increased. The experimental measurements (red dots) together with a theoretical prediction (solid blue line) are plotted for $\omega_0 = 0.5$ mm and $\omega_l = 0.23$ mm.

the data in Fig. 4.9 to the theoretical Schmidt number of Eq. (4.2.13). In the case of BG modes, the azimuthal Schmidt number is dependent on the value of the radial wavevector, as seen in Fig. 4.10. The experimental results are plotted together with a theoretical prediction based on Eq. (4.2.13) and Eq. (4.2.15) for a collinear SPDC setup ($\omega_0 = 0.50$ mm, $\omega_l = 0.23$ mm). It is clear that as the value of the radial wavevector increases, so too, does the Schmidt number. These results are reminiscent of entanglement concentra-

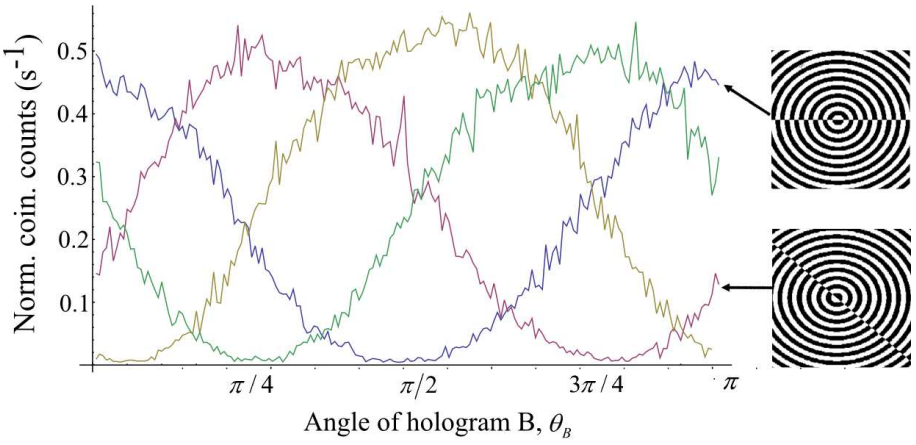

Figure 4.11: Sinusoidal behaviour of the normalised coincidence counts as a function of the angular position of the holograms, for $\ell = \pm 1$ subspace at positions $\theta_A = 0$ rad (blue), $\pi/4$ rad (pink), $\pi/2$ rad (green) and $3\pi/4$ rad (yellow). The insets show the holograms used for $\theta_A = 0$ rad and $\theta_A = \pi/4$ rad, where the phase varies from 0 (black) to π (white).

tion, where maximally entangled states are extracted from non-maximally entangled pure states [14]. The increase in accessible OAM modes is advantageous for high-dimensional entanglement, hence offering realisable applications in quantum information processing.

To verify that the quantum state produced in the SPDC process is entangled, we use it to test a Bell-type inequality. The method described in Sec. 2.4.2 was applied here, where the only difference arises from the displayed holograms. We fixed θ_A from Eq. (4.2.5) at four different angles: $\theta_A = 0, \pi/4, \pi/2, 3\pi/4$ radians, allowing θ_B to vary continuously from 0 to π radians. We remind ourselves of the Bell parameter, as defined in Ref. [36], given by

$$S(\theta_A, \theta_B) = E(\theta_A, \theta_B) - E(\theta_A, \theta_B') + E(\theta_A', \theta_B) - E(\theta_A', \theta_B'), \tag{4.4.1}$$

where $E(\theta_A, \theta_B)$ is determined from the measured coincidence counts at specific orientations of each hologram. The Bell curves are shown in Fig. 4.11 for BG modes with $k_r = 21$ rad/mm. For the two-dimensional BG subspace of $\ell = 1$, we find the Bell parameter in the CHSH inequality to be $S = 2.78 \pm 0.05 > 2$, which violates the inequality by 15 standard deviations.

We also reconstructed the (two-dimensional) two-photon density matrix, as shown in Fig. 4.12(a), in the BG basis for $k_r = 21$ rad/mm and $\ell = \pm 1$, using a full quantum state tomography [37]. The purity of the state $\mathrm{Tr}(\rho^2)$ was calculated as 0.981, where its closeness to 1 indicates that the observed quantum state is close to a pure state. To quantify the mixture of the measured state we calculate the linear entropy [130] $S_L = 4/3[1 - \mathrm{Tr}(\rho^2)]$. We find

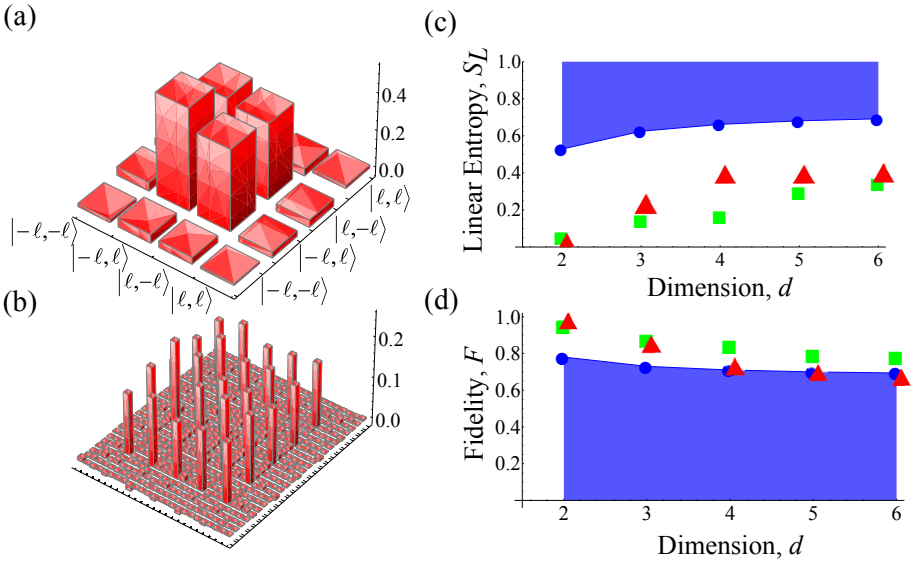

Figure 4.12: Results from a full quantum state tomography of a Bessel-Gaussian (BG) mode with $k_r = 21$ rad/mm. (a) & (b) Graphical representation of the real part of the density matrix for dimension $d = 2$ and $d = 5$, respectively. (c) Linear entropy and (d) fidelity as a function of dimension. The red triangles represent the measured data for the azimuthal modes, the green squares represent the measured data for the BG modes and the blue circles represent the threshold states in Eq. (13).

the linear entropy of our quantum state to be $S_{L2} = 0.06 \pm 0.01$, indicating that our state is close to a pure state (the linear entropy for a pure state is zero, whereas a completely mixed state is charaterised by a linear entropy of one). The fidelity of the entangled BG modes was also calculated, which is a measure of how close our reconstructed state ρ_d is to the target state $\rho_T = |\psi_T\rangle\langle\psi_T|$. In our case the target state is the (pure) maximally entangled state, $|\psi_T\rangle = 2^{-1/2}(|\ell\rangle_s|-\ell\rangle_i + |-\ell\rangle_s|\ell\rangle_i)$. We find a fidelity of $F = 0.96 \pm 0.01$. These results are indicative of entanglement of our BG modes.

Satisfied that the BG basis can be used to measure OAM entangled photon pairs, we then performed high-dimensional state tomography measurements [97] from $d = 2$ to $d = 6$. For $d = 2$ we use the OAM basis states $|\ell\rangle = \pm 1$ to measure the probabilities for each pure state (Eq. 4.2.3) and the superpositions (Eq. 4.2.5) thereof. The superposition states are rotated by and angle of $\theta = \pi/2$ such that the phase between the modes assumes values of $\{0, \pi/2, \pi, 3\pi/2\}$. Similarly for $d = 3$ we include the states $|\ell\rangle = \{-1, 0, 1\}$, up to $d = 6$ with the states $|\ell\rangle = \{-3, -2, -1, 1, 2, 3\}$. Using the measurement probabilities we calculated a higher-dimensional density matrix (real part) for $d = 5$ in Fig. 4.12(b). The constructed density matrices were used to compute the linear entropy and fidelity, with the

results shown in Figs. 4.12(c) and (d), respectively. We found that the higher-dimensional quantum states in terms of the BG modes for a particular k_r have more entanglement (high fidelity) than the quantum states in terms of azimuthal modes, while remaining relatively pure (low linear entropy), as shown in Fig. 4.12(c) and (d). These measurements are compared with the threshold states, introduced in Sec. 2.4.3. The fidelity values ranged from $F_2 = 0.96 \pm 0.01$ to $F_6 = 0.79 \pm 0.01$ for the BG modes, while the values for linear entropy were found to be $S_{L2} = 0.06 \pm 0.01$ and $S_{L6} = 0.35 \pm 0.01$.

4.5 Conclusion

We have used back-projection as an aid in designing a measurement scheme for probing OAM correlations. By propagating a classical beam from one of the detectors onto the plane of the crystal, we were able to examine three transmission functions for generating and measuring modes with both helical and radial structures. We investigated the efficacy of a blazed axicon, a binary axicon and a binary Bessel function in generating BG modes. Only the binary Bessel function, resulted into Bessel-Gauss modes at the plane of the crystal. OAM correlations in photons generated via SPDC were then measured using these three transmission functions. The OAM bandwidth obtained from the use of both the blazed and binary axicon transmission functions were similar to the OAM bandwidth obtained when using spiral phase masks, which measure helical modes. However, using the binary Bessel transmission function to measure BG modes, leads to a larger OAM bandwidth and more usable OAM modes. The number of modes were shown to increase in a tunable manner, with the minimum set by the LG case. We have successfully demonstrated that BG modes are entangled in the high-dimensional OAM degree of freedom. The resulting high-dimensionally entangled states are closer to the appropriate maximally entangled state compared to azimuthal modes. Such control of the experimental conditions results in a higher information capacity per photon pair and allows for more states to be utilized in quantum information processes. The only cost of the increased spiral spectrum of the recorded modes is a lower coincidence count rate. Due to the particular interference properties of BG modes, entangled modes in this basis may offer increased robustness when propagating through turbulent media. The finite space-bandwidth product of the SLMs limits the achievable spectrum of the BG modes; however, alternative methods may offer

further improvements in OAM entanglement with BG modes. This is useful for quantum information and communication applications requiring entanglement in higher dimensions.

Chapter 5

Self-healing of quantum entanglement

Quantum entanglement between photon pairs is fragile and can easily be masked by losses in transmission path and noise in the detection system. When observing the quantum entanglement between the spatial states of photon pairs produced by parametric down conversion, the presence of an obstruction introduces losses that can mask the correlations associated with the entanglement. In this chapter, we show that by measuring in the Bessel basis we can overcome these losses, thus once again revealing the entanglement after propagation beyond the obstruction. We confirm that, for the entanglement of orbital angular momentum, measurement in the Bessel basis is more robust to these losses than measuring in the usually employed Laguerre-Gaussian basis. Our results show that appropriate choice of measurement basis can overcome some limitations of the transmission path, perhaps offering advantages in free-space quantum communication or quantum processing systems.

5.1 Introduction

Quantum entanglement of the orbital angular momentum (OAM) modes has been demonstrated by measuring in both the Laguerre-Gaussian (LG) [9] and Bessel-Gaussian (BG) bases [131; 132]. Chapter 4 illustrated an increase in the number of accessible OAM modes when measured in the BG basis, which lead to higher-dimensional entanglement. An increase in dimension leads to improved security in quantum key distribution as well as increased information capacity in quantum communication protocols [133; 134].

Unfortunately while photons are weakly interacting, their entanglement is nevertheless fragile to the environment [135]. There have been a number of efforts in mitigating the decoherence in quantum computers and information processes based on ion traps, nuclear magnetic resonance and hyper-entanglement [136; 137; 138]. There have also been theoretical suggestions to recover lost entanglement [139], however it is yet to be demonstrated experimentally. In the context of OAM modes the decay of entanglement has been both predicted [47] and measured [140] for atmospheric turbulence as an environment, with some success in diminishing these effects [141; 142; 143].

Here we investigate the ability of OAM modes to recover the measured degree of entanglement of the quantum state after encountering an obstruction. It is well known that BG beams have the ability to self-heal after encountering an obstruction [144; 145]. An obstruction placed in the path of one of the down-converted photons introduces an optical loss such that the OAM entanglement, as witnessed by the Clauser Horne Shimony Holt (CHSH) inequality, is obscured. We then show that by measuring in the BG basis the classical self-healing of the Bessel profile gives a higher signal and the OAM entanglement is once again revealed. We demonstrate a dependence of the calculated concurrence of the quantum state on the location of the obstruction within the propagation path, and find that this is in agreement with the classical self-healing distance of BG beams. We thus find that even when applied to single photons, this self-healing property of the Bessel beam allows us to overcome the losses associated with the obstruction such that the spatial correlations can be measured with sufficient fidelity to reveal the quantum entanglement of the photon pairs.

5.2 Bessel beams

In the previous chapter, we introduced Bessel beams as a class of nominally propagation invariant solutions to the Helmholtz equation [126]. A laboratory approximation to these fields, Bessel-Gaussian beams, have similar properties over finite distances [128], including their ability to reconstruct both in amplitude and phase after encountering an obstruction [144; 145]. Although this property has been studied using classical light and single photons [146], it may also be applicable in quantum processes.

Higher-order Bessel and BG beams have helical wavefronts and carry OAM [127]. We demonstrated in the previous chapter that entanglement of the OAM modes in the BG basis offers a wider spiral spectrum as compared with the LG basis [131]. We described these beams as a superposition of plane waves with wave vectors that lie on a cone [128]. The electric field of a scalar BG mode of order ℓ is given by

$$E_\ell^{\mathrm{BG}}(r,\phi,z) = \sqrt{\frac{2}{\pi}}\mathrm{J}_\ell\left(\frac{z_R k_r r}{z_R - iz}\right)\exp(i\ell\phi - ik_z z)\exp\left(\frac{k_r^2 z w_0^2 - 2kr^2}{4(z_R - iz)}\right), \tag{5.2.1}$$

where ℓ is the azimuthal (mode) index (a signed integer); $\mathrm{J}_\ell(\cdot)$ is the Bessel function of the first kind; k_r and k_z are the radial and longitudinal wave vectors, respectively. The initial radius of the Gaussian profile is w_0 and the Rayleigh range is $z_\mathrm{R} = \pi w_0^2/\lambda$, where λ is the wavelength of the BG mode. A BG beam has a finite propagation distance, $z_{\max}$, over which it is said to be nominally non-diffracting, shown as the shaded diamond-like region in Fig. 5.1 [147]. In this region the incoming plane waves are refracted through an axicon (conical lens) and interfere to form the BG beam. The resulting wave vectors lie on a cone of angle $\theta = \arcsin(k_r/k)$. Using simple geometric arguments, the maximum propagation distance is defined as $z_{\max} = 2\pi w_0/\lambda k_r$, where $\sin(\theta) \approx \theta$ for small θ. If an obstruction of radius R is placed in the BG field, a shadow region is formed (see Fig. 5.1). However, those plane waves that bypass the obstruction will again interfere to form a BG beam [144; 145]. The distance after which the field will recover is given by

$$z_{\min} \approx \frac{R}{\theta} \approx \frac{2\pi R}{k_r \lambda}, \tag{5.2.2}$$

and is determined from purely geometric arguments [148]. The insets in Fig. 5.1 show the effect of an obstruction on expected BG field at different planes.

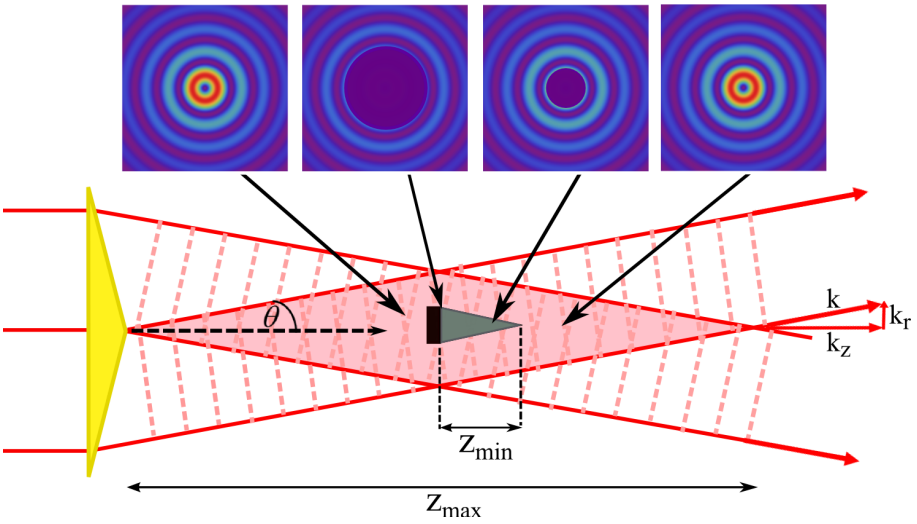

Figure 5.1: Self-healing property of Bessel-Gaussian (BG) beams. The BG beam is generated using a computer-generated hologram of an axicon (yellow triangle) and exists in a finite region, $z_{\max}$ (pink diamond). An obstacle placed in the centre of the BG region (black rectangle) obstructs the beam for a minimum distance, $z_{\min}$ (grey triangle), after which the BG field reforms. The insets display the expected image of the beam at four different planes.

5.3 Setup

We generated the BG modes by encoding a phase-only hologram onto a spatial light modulator (SLM) [129; 149], using the same transmission function as in Sec. 4.3.3, written as

$$T(r,\phi) = \mathrm{sgn}\{\mathrm{J}_\ell(k_r r)\}\exp(i\ell\phi), \tag{5.3.1}$$

where $\mathrm{sgn}\{\cdot\}$ denotes the sign-function. In the following experimental results, we generated a BG mode with $k_r = 30$ rad mm^{-1}.

Our experimental setup, shown in Fig. 5.2, consisted of identical components described throughout this thesis, but with one addition. A glass plate with a circular obstruction with a 200 μm radius was placed after the crystal in the path of the down-converted light and mounted on a z-axis translation stage. The coincidence count rate was measured as before; SLMs projected the photon into a particular state, where after single-mode fibres (SMFs) together with avalanche photo-diodes (APDs) delivered a signal to a coincidence counter.

The experimental setup in Fig. 5.2 was first aligned in back-projection mode, where a classical laser source was connected to one of the SMFs to allow light to propagate through the system in reverse. In Sec. 2.3.1, this method was shown to be useful in examining

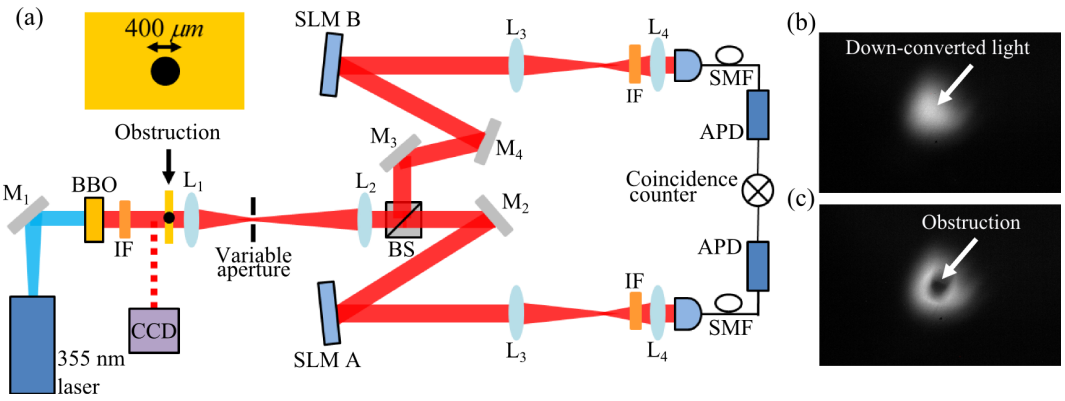

Figure 5.2: Experimental setup. The setup shown was used to measure the effect of an obstruction in the path of the down-converted light. (a) A UV laser source pumped a type-I barium borate (BBO) crystal to produce pairs of entangled photons via spontaneous parametric down-conversion. The crystal plane was imaged onto two separate spatial light modulators (SLMs) using lenses L_1 ($f_1 = 200$ mm) and L_2 ($f_2 = 400$ mm). Each SLM plane was again imaged to the input of a single-mode fibre using lenses L_3 ($f_3 = 500$ mm) and L_4 ($f_4 = 2$ mm). (b) Down-converted beam at the plane of the crystal. (c) A circular obstruction (radius = 200 μm) was placed between the crystal and lens L_1, in the path of the down-converted light.

the conditional probability distribution of the coincidence count rate [132]. Fibre A was disconnected from one of the APDs and reconnected it to a continuous light source at $\lambda = 710$ nm. The classical light was directed onto SLM A and imaged to the crystal plane via lenses L_1 and L_2. Images of the obstruction were recorded by placing a mirror between the crystal and obstruction and a CCD camera at the plane of the crystal. Classical images of the self-healing property are shown in Fig. 5.3 for both the BG (Fig. 5.3(a-d)) and LG (Fig.5.3(e-h)) modes, where the unobstructed BG and LG modes are shown in Fig. 5.3(a) and (e), respectively. We calculated the maximum propagation distance of the BG field as $z_{max} = 169.6$ mm. The obstruction was first placed at the plane of the crystal, which is clearly shown in both Fig. 5.3(b) and (f). It was then moved 20 mm away from the crystal plane, shown in Fig. 5.3(c) and (g). The final images, Fig. 5.3(d) and (h), were taken 50 mm away from the crystal. It is clear the BG mode has reformed at 50 mm, while the LG mode has not resumed it's original structure. In a typical self-healing experiment [145], the obstruction is placed at a fixed position in the path of the beam and the CCD camera is moved such that the subsequent planes behind the obstruction can be imaged. However, an identical effect is seen if the CCD camera remains fixed, imaging one particular plane, and the obstruction is moved away from that plane. This is illustrated in Fig. 5.4, where we consider back-projected light directed from the SLM to the crystal. The obstruction is

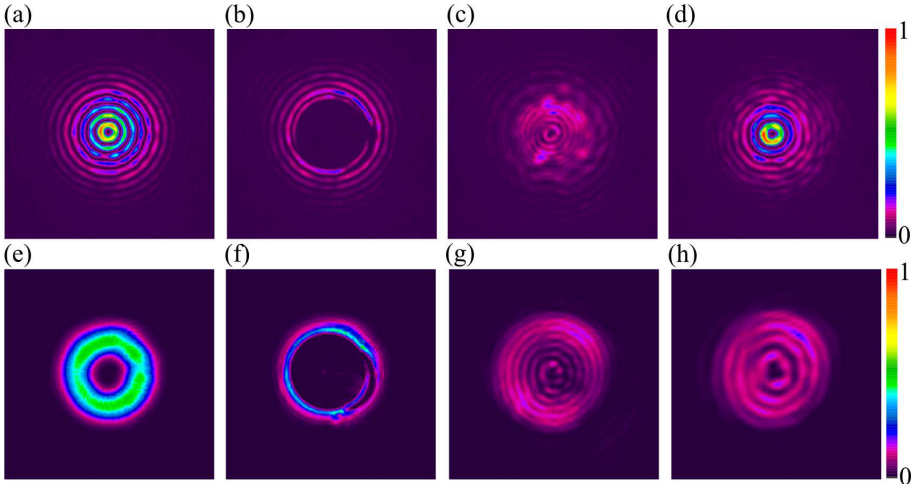

Figure 5.3: CCD images of the crystal plane for different on-axis obstruction positions. Images for a Bessel-Gaussian (BG) mode (a-d) and a Laguerre-Gaussian (LG) mode (e-h) with azimuthal index $\ell = 2$. The unobstructed modes are shown in (a) and (e). The obstruction was first placed at the plane of the crystal, which is clearly shown in both (b) and (f). It was then moved 20 mm away from the crystal plane, shown in (c) and (g). The final images, (d) and (h), were taken 50 mm away from the crystal. It is clear the BG mode has reformed at 50 mm, while the LG mode has not resumed it's original structure.

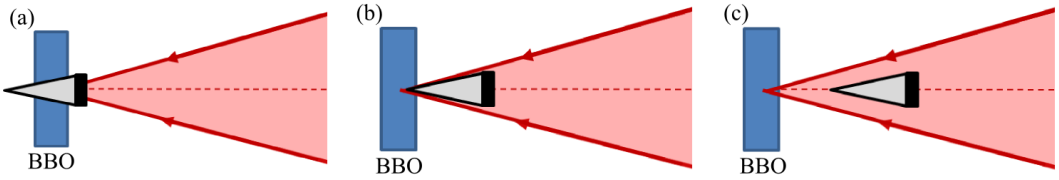

Figure 5.4: Movement of the obstruction within the Bessel-Gaussian (BG) region. Consider the back-projected beam reflecting off the spatial light modulator (SLM) onto the barium borate (BBO) crystal. The Bessel hologram on the SLM creates a beam with a particular cone angle. (a) The obstruction is at the closest position to the crystal, resulting in a clear shadow region falling on the crystal. (b) The obstruction is moved away from the crystal, reducing the shadow region. (c) The obstruction is moved further away such that the shadow region no longer falls on the crystal and a recovered BG image is seen (Fig. 5.3(d)).

moved away from the crystal toward lens L_1. As the obstruction moves, the shadow region falling on the crystal becomes less significant until finally it no longer falls on the crystal and the recovered mode is observed as shown in Fig. 5.3(d).

From equation. (5.2.2), we calculated a minimum self-healing distance of approximately 29 mm for $R = 200$ μm and $k_r = 30$ rad mm^{-1}. After a distance, the obstructed BG mode demonstrated a restored structure, while the LG mode showed no self-healing. The BG field reconstructed after z_{min} as expected.

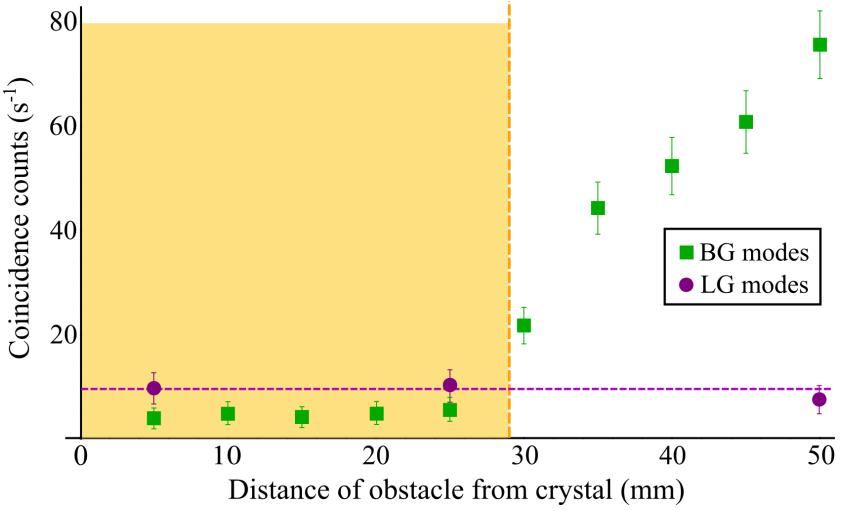

Figure 5.5: Effect of an obstacle on the coincidence count rate. Measured coincidence count rates as a function of the position of the obstruction after the barium borate crystal for a Bessel-Gaussian (BG) (green squares) and Laguerre-Gaussian (LG) (purple circles) mode for $|\ell = \pm 2\rangle$ subspace. The BG mode with $k_r = 30$ rad mm^{-1} is expected to reconstruct after an obstruction with radius, $R = 200$ μm, after a distance of approximately 29 mm (yellow dashed line). The coincidence count rate remains consistently low when measured in the LG basis (purple dashed line). The count rates were averaged over a set of 10 measurements, each taken over an integration period of 5s. Errors were estimated assuming Poisson statistics for the photon counts given as a standard deviation.

The setup was then returned to down-conversion mode (both SMFs were connected to their respective detectors) to investigate the effects of the obstruction on two-photon quantum correlations. As OAM is conserved in SPDC [9], we chose to first project the signal and idler photons into the $|\ell = \pm 2\rangle$ basis elements, respectively. The coincidence count rate of this BG state, unobstructed, was measured to be approximately 140 s^{-1}. The obstruction was initially inserted 5 mm after the BBO crystal, the closest it could be place due to the size of the crystal housing, and moved in subsequent intervals of 5 mm away from the crystal. Slight adjustments were made to the position of the obstruction until a minimum count rate was measured, causing the coincidence levels to be reduced to background levels. At each position coincidences were recorded; a comparison of the coincidence count rates for the BG and LG modes is shown in Fig. 5.5. The count rate for the BG mode increased significantly after a distance of 25 mm, which is consistent with our calculation of $z_{\text{min}} \approx 29$ mm. Conversely, the count rates for the LG mode showed no measurable change with distance, illustrating the unique self-healing property of BG modes. The coincidence count rate of the BG mode was not restored to the original, unobstructed rate, as there is a loss due to the obstacle. This is also consistent with the classical scenario where the self-healed

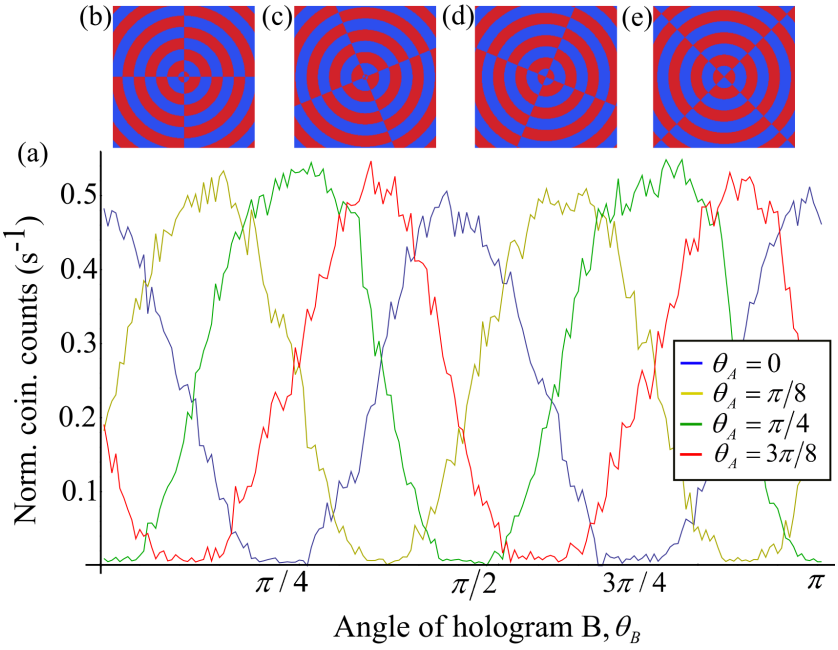

Figure 5.6: CHSH-Bell measurements. (a) Normalised coincidence count rate as a function of the orientation of the hologram on spatial light modulator B. Hologram A was oriented at 4 different angles: 0 rad (blue curve), $\pi/8$ rad (yellow curve), $\pi/4$ rad (green curve) and $3\pi/8$ rad (red curve). The measured count rates were normalized by the denominator in equation 2.4.7. The typical sinusoidal Bell-curve was measured with the obstruction placed in the propagation path at 45 mm from the crystal. Examples of the binary Bessel holograms ($|\ell = \pm 2\rangle$) used to perform a CHSH-inequality experiment are shown in the insets (b-e).

BG beam has proportionally less energy after the obstacle than before.

5.4 Measuring the degree of entanglement

The recovery of the BG coincidence count rate does not in itself give an indication of the effects the obstruction has on the degree of entanglement of the state. To investigate the measured degree of entanglement we first performed a Bell-type inequality experiment on the reformed state with the obstruction located 45 mm from the crystal to test for quantum correlations. The superposition of OAM states, also known as sector states, for $|\ell = \pm 2\rangle$ subspace were rotated on each SLM [36] and the corresponding coincidence count rates were recorded, shown in Fig. 5.6(a).

From the count rates we calculated the CHSH-Bell-parameter to be $S = 2.78 \pm 0.04$, which is a clear violation of the CHSH-Bell inequality [2]. This value of S can be compared with the unobstructed value of $S = 2.79 \pm 0.03$. The low coincidence count rate

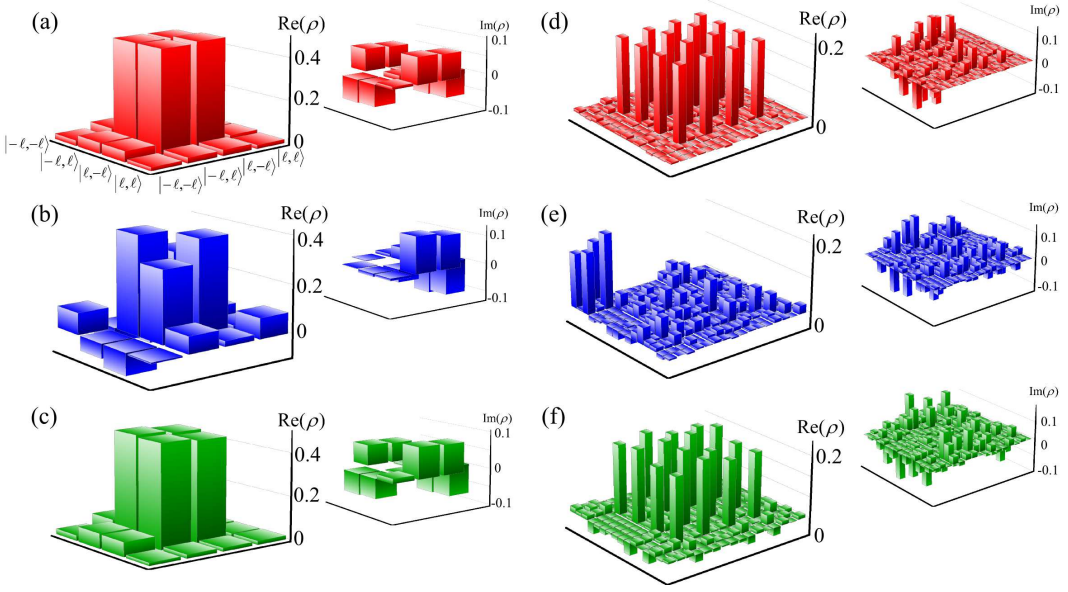

Figure 5.7: Reconstructed density matrices from full state tomography measurements. The density matrices are shown for dimensions $d = 2$ (a - c) and $d = 4$ (d - f). Real and imaginary parts of the reconstructed density matrices for (a) & (d) no obstruction, (b) & (e) obstruction placed 5 mm from the crystal and (c) & (f) obstruction placed 45 mm from the crystal. It is clear that the density matrix recovers to the original unobstructed form for a two-dimensional state as well as higher dimensional states. The density matrices were calculated by measuring an over-complete set of modes and applying a maximum likelihood estimation using a least squares fit to the measurements. This optimisation technique ensures a density matrix with non-negative eigenvalues and a trace of unity.

recorded when the obstruction was 5 mm from the crystal resulted in a low contrast Bell curve, from which the S-parameter could not be calculated. This prompted us to perform a full state tomography experiment [150] to determine the degree of entanglement of the state. Figure 5.7 shows the real and imaginary parts of the reconstructed density matrices for dimensions $d = 2$ for $|\ell = \pm 2\rangle$ and $d = 4$ for $|\ell = \{-2,-1,1,2\}\rangle$. The unobstructed density matrices for $d = 2$ and $d = 4$ are shown in Fig. 5.7(a) and (d), respectively. When the obstruction was placed near the crystal, the density matrices in both cases change significantly such that the inner dominant probabilities are reduced and the outer terms become non-zero, Fig. 5.7(b) and (e). However, once the obstruction was moved beyond the z_{min} distance, both density matrices return to their original form, Fig. 5.7(c) and (f).

From the density matrices, the concurrence of the state was calculated. Concurrence is a measure of entanglement, with a range from 0 (no entanglement) to 1 (maximally entangled) [151]. The concurrence can only be calculated for two-dimensional subspaces,

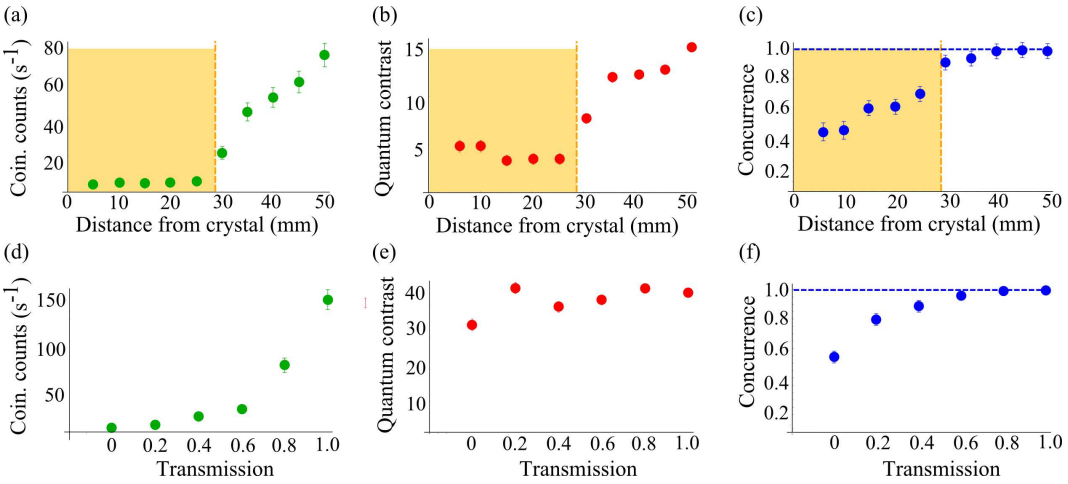

Figure 5.8: Comparison between an obstructed and attenuated beam. Measurements of the coincidence count rate, quantum contrast and concurrence of obstructed (a-c) and attenuated (d-f) entangled photons for $|\ell = \pm 2\rangle$. The obstruction was moved in 5 mm intervals along the propagation axis, at which the measurements were recorded. The dashed yellow line represents z_{min}, the calculated distance at which recovery is expected (recovery is not expected within the yellow shaded region). A polariser was rotated to attenuate the coincidence count rate and vary the degree of transmission from 0 (background levels) to 1 (unattenuated and unobstructed). The coincidence count rates and quantum contrast represent the average of 10 measurements. The average error for the concurrence is ± 0.01, which is calculated by generating additional data sets by adding $\sqrt{C_i}$ fluctuations to the measured coincidence counts C_i and then repeating the concurrence calculations described in the text. The unobstructed concurrence value is represented by the blue dashed lines.

so we considered two different OAM subspaces, $|\ell = \pm 2\rangle$ and $|\ell = \pm 4\rangle$, to demonstrate the self-healing property holds for higher OAM modes. The unobstructed BG mode for subspace $|\ell = \pm 2\rangle$ ($|\ell = \pm 4\rangle$) generated an average quantum contrast (see Methods) of $QC = 43.2 \pm 2.0$ ($QC = 41.7 \pm 2.0$) and a concurrence of $C = 0.95 \pm 0.02$ ($C = 0.94 \pm 0.02$). When the obstruction was placed 5 mm from the crystal, the concurrence dropped to $C = 0.40 \pm 0.02$ ($C = 0.43 \pm 0.02$), but recovered to a value of $C = 0.94 \pm 0.02$ ($C = 0.91 \pm 0.02$) at 50 mm from the crystal. The results for the coincidences, quantum contrast and concurrence of the $|\ell = \pm 2\rangle$ entangled photons are shown in Fig. 5.8(a) through (c), respectively. All three graphs display similar trends, where the values increase after a minimum distance represented by the yellow dashed line. As in the classical case, where energy is lost in the recovered field, the coincidence counts also do not fully recover to the original unobstructed rate. Consequently, the recovered quantum contrast does not return to the unobstructed value, as the accidental count rate remains fairly constant with the insertion of the obstruction.

From the high-dimensional density matrices in Fig. 5.7, we calculated the fidelity of the

states. Fidelity is a measure of how close the measured state is to a maximally entangled state, where a perfectly entangled state will have a fidelity of unity with the maximally entangled state. We have extended this demonstration to higher dimensions by reconstructing the density matrices for dimension $d = 4$ where $|\ell = \{-2, -1, 1, 2\}\rangle$. The reconstruction process via full state tomography is time consuming and thus only one high-dimensional state was chosen. The density matrices for different placements of the obstruction are shown in Fig. 5.7 (d - f). Table 5.1 shows the fidelity measurements recorded at different positions of the obstruction from the crystal.

Table 5.1: Measured fidelity at different obstacle positions from the crystal

Dimension	5 mm	15 mm	30 mm	50 mm	Unobstructed
2 ($\|\ell = \pm 2\rangle$)	0.24	0.59	0.79	0.96	0.97
4	0.20	0.45	0.68	0.75	0.79

The measured fidelities for both dimensions recover to their relative unobstructed values. Fidelity decreases as the state dimension increases, however the recovered fidelity for $d = 4$ lies above the threshold states, which are defined by the minimum probability for which a high-dimensional Bell inequality is violated [99].

We have therefore demonstrated that the self-healing property of Bessel beams, even when applied to single photons, can overcome the losses associated with an obstruction, allowing sufficient measurement of the spatial correlations to reveal the quantum entanglement of the photon pairs.

5.5 Discussion

Our results show that by making projective measurements in the BG basis, we were able to recover the reduction in the measured degree of entanglement resulting from the losses introduced by the obstruction. By comparison, when the LG measurement basis is chosen, the entanglement is not recovered. From the density matrices, we see that while the obstruction perturbs the system, when measured beyond the minimum self-healing distance the density matrix reverts to the original unobstructed form. Comparing the graphs of the coincidence count rates and concurrence in both experiments, we observe a similar trend:

the degree of entanglement is low for low coincidence count rates and then increases with the count rate. It appears that the off-axis obstruction does not destroy the entanglement by scattering a particular OAM state into many OAM states, as observed in turbulence related experiments [140], but rather decreases the measured degree of entanglement by reducing the two-photon count rates to background levels. For completeness, we also measured the response of an unobstructed BG mode in the presence of attenuation. By rotating a polariser in the path of the down-converted light, the transmission of the photons could be varied from background levels (≈ 0 transmission) to normal conditions (transmission of 1). The coincidence count rate, quantum contrast and concurrence for various transmission values are shown in Fig. 5.8(d) through (f), respectively. The quantum contrast (Fig. 5.8(b)) suggests that the obstacle blocks one of the entangled photons, thus diminishing the coincidence rate but maintaining a high single-photon count rate. However, the attenuated quantum contrast remains fairly constant unlike that of the obstructed beam. The attenuation reduced the count rates for both the single and coincidence counts proportionally, thereby maintaining a constant quantum contrast ratio. The obstruction on the other hand reduced only the coincidence count rate and in turn, the quantum contrast. The entanglement is therefore obscured by the noise. The correlations are recovered beyond the minimum distance after the obstacle because the mode itself recovers, thus increasing the signal at the detector because of an improved overlap between the hologram and the projected mode. Interestingly, the measurement choice is made after the photons have encountered the obstacle. By contrast, in a classical experiment, the mode is chosen or generated before interacting with the obstacle.

In conclusion, we have exploited the self-healing property of Bessel-Gaussian modes in a quantum entanglement experiment to recover the reduction in the measured degree of entanglement. We showed that the coincidence count rate is reduced in the presence of an obstacle, but that the count rate recovers after a particular distance due to the self-healing feature of BG modes. This trend was similarly reported for the degree of entanglement of the quantum state, where the concurrence of the obstructed mode returned to it's original, unobstructed value. These results may be useful for quantum key distribution and quantum communication systems, where preservation of entanglement over long distances and in the presence of an obstruction is crucial.

Chapter 6

Conclusion

The work in this thesis investigated the potential of orbital angular momentum (OAM) entanglement of photons in the realm of high-dimensional entanglement by tailoring both the generation and measurement parameters. The possibility of accessing an infinite number of modes provides OAM entanglement with a significant advantage over polarisation entanglement. In Chap. 2 we described and demonstrated, for the first time in South Africa, the experimental procedures involved in the generation and measurement of two-dimensional OAM entanglement. Further, we verified important quantum tests such as the Einstein, Podolsky and Rosen (EPR) paradox using OAM and angle correlations. We showed a violation of a Bell-type inequality and fully characterised our state by performing a quantum state tomography. High-dimensional entanglement is a requirement for most quantum information processes. We demonstrated how to tomographically reconstruct the density matrices for high-dimensional states. This process allows the quantum state to be fully characterised and as such allows the suitability of the state for specific applications to be precisely determined. Unfortunately, the number of accessible OAM modes are bounded by experimental techniques used to generate and measure OAM entanglement. In light of this, we aimed to investigate new methods in which to increase the spiral bandwidth of our generated quantum state.

We first demonstrated the effect of the pump shape on both OAM and angle correlations using an OAM superposition state. Our results suggest that more complicated pump modes may be used to engineer entangled OAM states for particular applications.

We noted that typical OAM entanglement schemes use helical modes, which ignore the

radial component of the Laguerre-Gaussian (LG) modes, as a measurement basis. This lead us to explore alternative modes with the ability to carry OAM. The Bessel-Gaussian (BG) basis not only carries OAM but has a continuous scalable radial component, which can be varied to optimise the measured spiral bandwidth. We demonstrated entanglement of BG modes for the first time and our results show that the spiral bandwidth can be made wider and flatter by simply changing the radial component. Consequently, we were able to show that BG modes can be entangled in higher dimensions than helical modes by calculating and comparing the linear entropy and fidelity for both modes. We also showed that quantum entanglement can be accurately simulated using classical light using back-projection. This experimental tool allows us to study projective measurements (helical or BG) and predict the strength of the coincidence correlations in an entanglement experiment. In particular, we used back-projection to examine different projective BG holograms before choosing the optimal hologram for our entanglement experiment.

Lastly, we combined the effect of a perturbation on OAM entanglement with BG projective measurements. Classically, BG beams are known to self-heal after encountering an obstruction. We therefore investigated this property in the single photon regime by placing an obstruction in the path of the down-converted photon pairs. The obstruction was placed at different positions relative to the non-linear crystal and a full state tomography was performed at each position to reconstruct the density matrix. We calculated the concurrence from each density matrix and showed that the concurrence increases from a mixed state to a highly entangled state when the obstruction is placed a particular distance away from the crystal. The distance at which the measured entanglement recovered is consistent with that observed in classical experiments.

In this thesis, we aimed to introduce OAM entanglement by examining the techniques used to generate, measure and detect entangled photons. This is a relatively young field in which there are a number of areas for improvement. We have sought to add to this field by demonstrating new measurement techniques and providing a quantified look at OAM entanglement robustness when perturbed.

6.1 Future Work

This thesis has investigated OAM entanglement in the BG basis. We would now like to apply this beneficial measurement basis to specific applications in the hope of improving upon existing results in the LG basis. In particular, we aim to implement the BG modes in two applications that we have recently demonstrated with LG modes. The first being an experimental study of high-dimensional quantum key distribution protocols based on mutually unbiased bases.

Mutually unbiased bases (MUBs) [152; 153; 154] have found many applications, for example in quantum state tomography [154; 155; 156; 157] and quantum error correction codes [158; 159] and also appear useful in QKD protocols. This is because projective measurements in one basis provides no knowledge of the state in any of the other bases [160; 161; 162]. Therefore if an eavesdropper measures in the incorrect basis he/she will obtain no meaningful information but instead introduce a disturbance in the system, resulting in its detection. The simplest example of MUBs of dimension $d = 2$ are the horizontal/vertical, diagonal/anti-diagonal, and left-/right-handed polarization bases as they are unbiased with respect to each other, forming a set of three MUBs. Although MUBs offer security against eavesdropping, encoding states in the polarization degree of freedom only allows a maximum of one bit of information transmitted per photon which results in a limited key generation rate. Since systems with higher-dimensional Hilbert space can store more information per carrier, the question arises whether QKD protocols using higher-dimensional MUBs also result in higher generation rates of secure key bits; indeed, such protocols can be expected to be more robust in terms of abstract noise measures [163; 164].

We continued our investigation into alternative projection bases by using high-dimensional MUBs in the OAM degree of freedom to study quantum key distribution protocols [165]. The choice of MUBs was obtained by assuming that the standard basis, $\{|0\rangle, |1\rangle, \cdots, |d-1\rangle\}$, is realised by single-photon states that correspond to an elementary excitation of Laguerre-Gaussian (LG) modes carrying an OAM value of $\ell\hbar$. The Shannon information for d = 2, 3, 4 and 5 is calculated to be I(A:B) = 0.9999, 1.313, 1.478 and 1.487, respectively (depicted by the green data points in Fig. 6.1), while the Shannon mutual information increases monotonically, it seems to level off for d = 4 and 5. On the other hand $r_{\min}$ first increases and then decreases for d = 5. This means that we have reached a finite limit on the dimension in

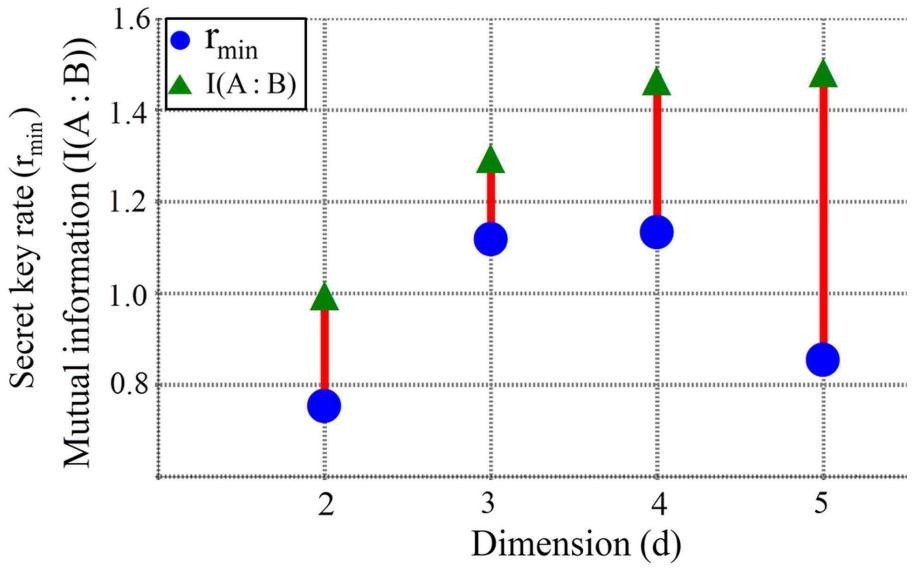

Figure 6.1: The Shannon mutual information I(A:B) *(green)* and the secret key rate $r_{\min}$ *(blue)* plotted as a function of the dimension.

which the protocol can encode, while still resulting in higher generation rates per photon. The difference between these two quantities (I(A:B) and $r_{\min}$) is the mutual information between Alice and Eve, in other words the information that is shared between Alice and Eve (denoted by the red lines in Fig. 6.1). By increasing the dimension, we achieved increased information capacity as well as higher key generation rates per photon, which is crucial in quantum communication protocols.

We plan to repeat our MUB experiment, using BG modes to generate the standard basis, in the hope of improving upon our previous results. In particular, we would like to minimise the mutual information between Alice and Eve (the sender and the eavesdropper), that is reduce the information passed onto an unwanted party.

The second application investigates the effects of atmospheric turbulence on an entangled state in the OAM basis. One of the biggest challenges that confronts the use of OAM photon states for quantum communication is the distortion of the modes during transmission over large distances. OAM encoding is incompatible with single mode optical fiber, because it only supports modes with zero OAM. An alternative is to use free-space communication. However, OAM modes suffer distortion due to the scintillation process that the photon pair experiences while propagating through the turbulent atmosphere, which negatively affects their entanglement. Moreover, in a practical communication system the

information would be encoded in terms of a finite number of OAM basis elements (say for example $\{|-1,-1\rangle;|-1,1\rangle;|1,-1\rangle;|1,1\rangle\}$ in the qubit case). As such the quantum information is restricted to a proper (finite dimensional) subspace of the complete OAM Hilbert space. Although the quantum state of the photon pair is initially prepared to lie completely within the information encoding subspace, scintillation generally causes the state of the photon pair to be partially transferred to the orthogonal compliment. The result is a loss of information in the photon field.

Previous theoretical studies of the effects of atmospheric turbulence on the OAM modes have considered the effect of turbulence on the detection probability of OAM modes [48; 49; 166], the attenuation and crosstalk among multiple OAM channels [167] and the decay of entanglement for bipartite qubits [53; 168]. These studies are all based on the Paterson model using a single phase screen [166]. We investigated numerically and experimentally the decay of OAM entanglement of photon pairs propagating in a turbulent atmosphere modelled with a single phase screen with particular focus on the effect of turbulence on different OAM modes [140]. We used the tomographic tool highlighted in Chap. 2 to reconstruct the density matrices of OAM qubit states propagated through turbulence. By using the expression of the Fried parameter [169], we find that the distance scale at which OAM entanglement decays as a function of ℓ is

$$L_{\text{dec}}(\ell) \approx \frac{0.06\lambda^2\ell^{5/6}}{\mathrm{w}_0^{5/3}C_n^2}, \tag{6.1.1}$$

where λ is the wavelength of the entangled photons, w_0 is the width of the beam and C_n^2 is the refractive-index structure constant. Thus for a practical free-space quantum communication system using OAM modes as qubits, the distance between repeaters should be shorter than $L_{\text{dec}}(\ell)$. For example, if one would send OAM entangled photons in a beam with $\mathrm{w}_0 = 10$ cm, a wavelength of $\lambda = 1550$ nm, on a horizontal path in moderate turbulence conditions ($C_n^2 = 10^{-15}\ m^{-2/3}$), the entanglement between the photons will decay around the distances shown in Table 6.1 for the different values of ℓ.

We notice in Table 6.1 that the distance scale at which entanglement decays is relatively short even in moderate turbulence. The implementation of BG modes may display an increased robustness through turbulence, thereby increasing the propagation distance of OAM entangled photons.

Table 6.1: Distance scale at which entanglement decays for OAM entangled photons in a beam with $w_0 = 10$ cm, a wavelength of $\lambda = 1550$ nm, on a horizontal path in moderate turbulence ($C_n^2 = 10^{-15}$ $m^{-2/3}$).

ℓ	1	3	5	7
L_{dec}(km)	6.7	16.7	25.6	33.7

Of course, a logical next step in understanding the effects of turbulence on entangled states, is to propagate the photons through a "real-world" thick turbulence cell. For example, a wind tunnel would provide a substantial distance in which the strength of the turbulence could be manually controlled without additional environmental factors such as humidity. Although we would expect to observe similar results obtained in the laboratory, one of the challenges would lie in the alignment of the entanglement setup over a distance of a few kilometres. Previous experiments have demonstrated quantum communication based on entanglement over 144 km of free-space [170]. However, polarisation-entangled photons were used, which are known to be more resilient against turbulence than those entangled in OAM. This experiment would be a step toward propagation between two external stations.

Bibliography

[1] Einstein, A., Podolsky, B. and Rosen, N.: Can quantum-mechanical description of physical reality be considered complete? *Phys. Rev.*, vol. 47, pp. 777–780, 1935.

[2] Clauser, J., Horne, M., Shimony, A. and Holt, R.: Proposed experiment to test local hidden-variable theories. *Phys. Rev. Lett.*, vol. 23, pp. 880–884, 1969.

[3] Freedman, S. and Clauser, J.: Experimental test of local hidden-variable theories. *Phys. Rev. Lett.*, vol. 28, pp. 938–941, 1972.

[4] Clauser, J.: Experimental investigation of a polarization correlation anomaly. *Phys. Rev. Lett.*, vol. 36, pp. 1223–1226, 1976.

[5] Aspect, A., Grangier, P. and Roger, G.: Experimental tests of realistic local theories via bell's theorem. *Phys. Rev. Lett.*, vol. 47, pp. 460–463, 1981.

[6] Aspect, A., Grangier, P. and Roger, G.: Experimental realization of einstein-podolsky-rosen-bohm gedankenexperiment: A new violation of bell's inequalities. *Phys. Rev. Lett.*, vol. 49, pp. 91–94, 1982.

[7] Shih, Y. and Alley, C.: New type of einstein-podolsky-rosen-bohm experiment using pairs of light quanta produced by optical parametric down conversion. *Phys. Rev. Lett.*, vol. 61, pp. 2921–2924, 1988.

[8] Gisin, N., Ribordy, G., Tittel, W. and Zbinden, H.: Quantum cryptograpy. *Rev. Mod. Phys.*, vol. 74, pp. 145–195, 2002.

[9] Mair, A., Vaziri, A., Weihs, G. and Zeilinger, A.: Entanglement of the orbital angular momentum states of photons. *Nature*, vol. 412, pp. 313–316, 2001.

[10] Dada, A., Leach, J., Buller, G., Padgett, M. and Andersson, E.: Experimental high-dimensional two-photon entanglement and violations of the generalized bell inequalities. *Nat. Phys.*, vol. 7, pp. 677–680, 2011.

[11] Bechmann-Pasquinucci, H. and Tittel, W.: Quantum cryptography using larger alphabets. *Phys. Rev. A*, vol. 61, no. 6, p. 62308, 2000.

[12] Walborn, S., Lemelle, D., Almeida, M. and Souto Ribeiro, P.: Quantum Key Distribution with Higher-Order Alphabets Using Spatially Encoded Qudits. *Phys. Rev. Lett.*, vol. 96, no. 9, p. 090501, 2006.

[13] Langford, N., Dalton, R., Harvey, M., O'Brien, J., Pryde, G., Gilchrist, A., Bartlett, S. and White, A.: Measuring entangled qutrits and their use for quantum bit commitment. *Phys. Rev. Lett.*, vol. 93, no. 5, p. 53601, 2004.

[14] Vaziri, A., Pan, J., Jennewein, T., Weihs, G. and Zeilinger, A.: Concentration of higher-dimensional entanglement: Qutrits of photon orbital angular momentum. *Phys. Rev. Lett.*, vol. 91, no. 22, p. 227902, 2003.

[15] Molina-Terriza, G., Vaziri, A., Ursin, R. and Zeilinger, A.: Experimental quantum coin tossing. *Phys. Rev. Lett.*, vol. 94, no. 4, p. 40501, 2005.

[16] Bennett, C., Brassard, G., Crépeau, C. Jozsa, R., Peres, A. and Wootters, W.: Teleporting an unknown quantum state via dual classical and einstein-podolsky-rosen channels. *Phys. Rev. Lett.*, vol. 70, no. 13, pp. 1895–1899, 1993.

[17] Bouwmeester, D., Pan, J., Mattle, K., Eibl, M., Weinfurter, H. and Zeilinger, A.: Experimental quantum teleportation. *Nature*, vol. 390, pp. 575–579, 1997.

[18] Khoury, A.Z. and Milman, P.: Quantum teleportation in the spin-orbit variables of photon pairs. *Phys. Rev. A*, vol. 83, no. 6, p. 060301, 2011.

[19] Maxwell, J.: A dynamical theory of the electromagnetic field. *Phil. Trans. R. Soc. Lond.*, vol. 155, pp. 459–512, 1865.

[20] Maxwell, J.: *A treatise on electricity and magnetism*. Dover Publications, New York, 1891.

[21] Poynting, J.: The wave motion of a revolving shaft, and a suggestion as to the angular momentum in a beam of circularly polarised light. *Proc. R. Soc. Lond. A Ser. A*, vol. 82, pp. 560–567, 1909.

[22] Beth, R.: Mechanical detection and measurement of the angular momentum of light. *Phys. Rev.*, vol. 50, pp. 115–125, 1936.

[23] Allen, L., Beijersbergen, M.W., Spreeuw, R.J.C. and Woerdman, J.P.: Orbital angular momentum of light and the transformation of Laguerre-Gaussian laser modes. *Phys. Rev. A*, vol. 45, pp. 8185–8189, 1992.

[24] Padgett, M. and Courtial, J.: Poincaré-sphere equivalent for light beams containing orbital angular momentum. *Opt. Lett.*, vol. 24, no. 7, pp. 430–432, 1999.

[25] He, H., Friese, M., Heckenberg, N. and Rubinsztein-Dunlop, H.: Direct observation of transfer of angular momentum to absorptive particles from a laser beam with a phase singularity. *Phys. Rev. Lett.*, vol. 75, pp. 826–829, 1995.

[26] Knöner, G., Parkin, S., Nieminen, T., Loke, V., Heckenberg, N. and Rubinsztein-Dunlop, H.: Integrated optomechanical microelements. *Opt. Express*, vol. 15, pp. 5521–5530, 2007.

[27] Allen, L. andPadjett, M. and Babiker, M.: The orbital angular momentum of light. *Prog. Opt.*, vol. 39, pp. 291–372, 1999.

[28] Volke-Sepulveda, K., Garcès-Chávez, V., Chávez-Cerda, S., Arlt, J. and Dholakia, K.: Orbital angular momentum of a high-order Bessel light beam. *J. Opt. B: Quantum Semiclass. Opt.*, vol. 4, pp. S82–S89, 2002.

[29] Bandres, M. and Gutiérrez-Vega, J.: Ince Gaussian beams. *Optics Lett.*, vol. 29, pp. 144–146, 2004.

[30] Barnett, S. and Pegg, D.: Quantum theory of rotation angles. *Phys. Rev. A*, vol. 41, pp. 3427–3435, 1990.

[31] Pegg, D. and Barnett, S.: Quantum optical phase. *J. Mod. Opt.*, vol. 44, pp. 225–264, 1997.

[32] Yao, E., Franke-Arnold, S., Courtial, J., Barnett, S. and Padgett, M.: Fourier relationship between angular position and optical orbital angular momentum. *Opt. Express*, vol. 14, pp. 9071–9076, 2006.

[33] Jha, A., Jack, B. andYao, E., Leach, J., Boyd, R., Buller, G., Barnett, S., Franke-Arnold, S., and Padgett, M.: Fourier relationship between the angle and angular momentum of entangled photons. *Phys. Rev. A*, vol. 78, p. 043810, 2008.

[34] Law, C. and Eberly, J.: Analysis and interpretation of high transverse entanglement in optical parametric down conversion. *Phys. Rev. Lett.*, vol. 92, no. 12, p. 127903, 2004.

[35] Kwiat, P., Mattle, K., Weinfurter, H., Zeilinger, A., Sergienko, A. and Shih, Y.: New high-intensity source of polarization-entangled photon pairs. *Phys. Rev. Lett.*, vol. 75, pp. 4337–4341, 1995.

[36] Leach, J., Jack, B., Ritsch-Marte, M., Boyd, R., Jha, A., Barnett, S., Franke-Arnold, S. and Padgett, M.: Violation of a bell inequality in two-dimensional orbital angular momentum state-spaces. *Opt. Express*, vol. 17, pp. 8287–8293, 2009.

[37] Jack, B., Leach, J., Ritsch, H., Barnett, S. and Padgett, M.: Precise quantum tomography of photon pairs with entangled orbital angular momentum. *New J. of Phys.*, vol. 811, p. 103024, 2009.

[38] Ekert, A.: Quantum cryptography based on bells theorem. *Phys. Rev. Lett.*, vol. 67, pp. 661–663, 1991.

[39] Torres, J.P., Alexandrescu, A. and Torner, L.: Quantum spiral bandwidth of entangled two-photon states. *Phys. Rev. A*, vol. 68, no. 5, p. 050301, Nov 2003.

[40] Di Lorenzo Pires, H., Florijn, H. and van Exter, M.: Measurement of the spiral spectrum of entangled two-photon states. *Phys. Rev. Lett.*, vol. 104, p. 020505, 2010.

[41] Romero, J., Giovannini, D., Franke-Arnold, S., Barnett, S.M. and Padgett, M.J.: Increasing the dimension in high-dimensional two-photon orbital angular momentum entanglement. *Phys. Rev. A*, vol. 86, p. 012334, 2012.

[42] Miatto, F.M., Yao, A.M. and Barnett, S.M.: Full characterization of the quantum spiral bandwidth of entangled biphotons. *Phys. Rev. A*, vol. 83, p. 033816, 2011.

[43] Salakhutdinov, V., Eliel, E. and Löffler, W.: Full-field quantum correlations of spatially entangled photons. *Phys. Rev. Lett.*, vol. 108, p. 173604, 2012.

[44] Arrizón, V., Ruiz, U., Carrada, R. and González, A.: Pixelated phase computer holograms for the accurate encoding of scalar complex fields. *J. Opt. Soc. Am. A*, vol. 24, pp. 3500–3507, 2007.

[45] Hübel, H., Vanner, M., Lederer, T., Blauensteiner, B., Lorünser, T., Poppe, A. and Zeilinger, A.: High-fidelity transmission of polarization encoded qubits from an entangled source over 100 km of fiber. *Opt. Express*, vol. 15, no. 12, pp. 7853–7862, 2007.

[46] Andrews, L. and Phillips, R.: *Laser Beam Propagation through random media*. SPIE, Bellingham, WA, 1998.

[47] Patterson, C.: Atmospheric turbulence and orbital angular momentum of single photons for optical communication. *Phys. Rev. Lett.*, vol. 94, p. 153901, 2005.

[48] Gopaul, C. and Andrews, R.: The effect of atmospheric turbulence on entangled orbital angular momentum states. *New J. Phys.*, vol. 9, p. 94, 2007.

[49] Tyler, G. and Boyd, R.: Influence of atmospheric turbulence on the propagation of quantum states of light carrying orbital angular momentum. *Opt. Lett.*, vol. 34, pp. 142–144, 2009.

[50] Malik, M., O'Sullivan, M., Rodenburg, B., Mirhosseini, M., Leach, J., Lavery, M., Padgett, M. and Boyd, R.: Influence of atmospheric turbulence on optical communications using orbital angular momentum for encoding. *Opt. Express*, vol. 20, pp. 13195–13200, 2012.

[51] Rodenburg, B., Lavery, M., Malik, M., O'Sullivan, M., Mirhosseini, M., Robertson, D., Padgett, M. and Boyd, R.: Influence of atmospheric turbulence on states of light carrying orbital angular momentum. *Opt. Lett.*, vol. 37, pp. 3735–3737, 2012.

[52] Pors, B., Monken, C., Eliel, E. and Woerdmann, J.: Transport of orbital-angular-momentum entanglement through a turbulent atmosphere. *Opt. Express*, vol. 19, pp. 6671–6683, 2011.

[53] Roux, F.: Infinitesimal-propagation equation for decoherence of an orbital-angular-momentum-entangled biphoton state in atmospheric turbulence. *Phys. Rev. A*, vol. 83, p. 053822, 2011.

[54] Harris, S., Oshman, M. and Byer, R.: Obsevation of tunable optical parametric fluorescence. *Phys. Rev. Lett.*, vol. 18, pp. 732–734, 1967.

[55] Kleinman, D.: Theory of optical parametric noise. *Phys. Rev.*, vol. 174, pp. 1027–1041, 1968.

[56] Burnham, D. and Weinberg, D.: Observation of simultaneity in parametric production of optical photon pairs. *Phys. Rev. Lett.*, vol. 25, pp. 84–87, 1970.

[57] Kocher, C. and Commins, E.: Polarization correlation of photons emitted in an atomic cascade. *Phys. Rev. Lett.*, vol. 18, pp. 575–577, 1967.

[58] Fry, E. and Thompson, R.: Experimental test of local hidden-variable theories. *Phys. Rev. Lett.*, vol. 37, pp. 465–468, 1976.

[59] Rarity, J. and Tapster, P.: Experimental violation of bell's inequality based on phase and momnetum. *Phys. Rev. Lett.*, vol. 64, pp. 2495–2498, 1990.

[60] Strekalov, D., Pittman, T., Sergienko, A., Shih, Y. and Kwiat, P.: Postselection-free energy-time entanglement. *Phys. Rev. A*, vol. 54, pp. R1–R4, 1996.

[61] Howell, J., Bennink, R., Bentley, S. and Boyd, R.: Postselection-free energy-time entanglement. *Phys. Rev. Lett.*, vol. 92, p. 210403, 2004.

[62] van Exter, M., Aiello, A., Oemrawsingh, S., Nienhuis, G. and Woerdman, J.: Effect of spatial filtering on the schmidt decomposition of entangled photons. *Phys. Rev. A*, vol. 74, p. 012309, 2006.

[63] Bechmann-Pasquinucci, H. and Peres, A.: Quantum cryptography with 3-state systems. *Phys. Rev. Lett.*, vol. 85, no. 15, pp. 3313–3316, 2000.

[64] Dixon, P.B., Howland, G.A., Schneeloch, J. and Howell, J.C.: Quantum mutual information capacity for high-dimensional entangled states. *Phys. Rev. Lett*, vol. 108, p. 143603, 2012.

[65] Torres, J., Deyanova, Y., Torner, L. and Molina-Terriza, G.: Preparation of engineered two-photon entangled states for multidimensional quantum information. *Phys. Rev. A*, vol. 67, p. 052313, 2003.

[66] Miatto, F.M., Giovannini, D., Romero, J., Franke-Arnold, S., Barnett, S. and Padgett, M.: Bounds and optimisation of orbital angular momentum bandwidths within parametric down-conversion systems. *Eur. Phys. J. D.*, vol. 66, p. 178, 2012.

[67] Ekert, A. and Knight, P.: Entangled quantum systems and the schimdt decomposition. *Am. J. Phys.*, vol. 63, pp. 415–423, 1995.

[68] van Exter, M., Lee, P., Doesburg, S. and Woerdman, J.: Mode counting in high-dimensional orbital angular momentum entanglement. *Opt. Express*, vol. 15, pp. 6431–6438, 2007.

[69] Beijersbergen, M., Coerwinkel, R., Kristensen, M. and Woerdmann, J.: Helical-wavefront laser beams produced with a spiral phaseplate. *Opt. Commun.*, vol. 112, pp. 321–327, 1994.

[70] Pittman, T.B., Strekalov, D.V., Klyshko, D.N., Rubin, M.H., Sergienko, A.V. and Shih, Y.H.: Two-photon geometric optics. *Phys. Rev. A*, vol. 53, pp. 2804–2815, 1996.

[71] Barnett, S.M., Pegg, D.T., Jeffers, J. and Jedrkiewicz, O.: Master equation for retrodiction of quantum communication signals. *Phys. Rev. Lett.*, vol. 86, pp. 2455–2458, 2001.

[72] Tan, E.K., Jeffers, J., Barnett, S.M. and Pegg, D.T.: Retrodictive states and two-photon quantum imaging. *Eur. Phys. J. D.*, vol. 22, pp. 495–499, 2003.

[73] Oemrawsingh, S.S.R., de Jong, J.A., Ma, X., Aiello, A., Eliel, E.R., 't Hooft, G.W. and Woerdman, J.P.: High-dimensional mode analyzers for spatial quantum entanglement. *Phys. Rev. A*, vol. 73, p. 032339, 2006.

[74] Klyshko, D.: A simple method of preparing pure states of an optical field, of implementing the einstein-podolsky-rosen experiment, and of demonstrating the complementarity principle. *Soviet Physics Uspekhi*, vol. 31, no. 74, pp. 74–85, 1988.

[75] Pittman, T., Shih, Y., Strekalov, D. and Sergienko, A.: Optical imaging by means of two-photon quantum entanglement. *Phys. Rev. A*, vol. 52, pp. R3429–R3432, 1995.

[76] Franke-Arnold, S., Barnett, S., Padgett, M. and Allen, L.: Two-photon entanglement of orbital angular momentum states. *Phys. Rev. A*, vol. 65, p. 033823, 2002.

[77] Bohm, D.: *Quantum theory*. Prentice-Hall, Engelwood Cliffs, NJ, 1951.

[78] Reid, M.: Demonstration of the einstein-podolsky-rosen paradox usng nondegenerate parametric amplification. *Phys. Rev. A*, vol. 40, pp. 913–923, 1989.

[79] Ou, Z., Pereira, S., Kimble, H. and Peng, K.: Realization of the einstein-podolsky-rosen paradox for continuous variables. *Phys. Rev. Lett.*, vol. 68, pp. 3663–3666, 1992.

[80] Götte, J., Franke-Arnold, S. and Barnett, S.: Angular epr paradox. *J. Mod. Opt.*, vol. 53, pp. 627–645, 2005.

[81] Franke-Arnold, S., Barnett, S., Yao, E., Leach, J., Courtial, J. and Padgett, M.: Uncertainty principle for angular position and angular momentum. *N. J. Phys.*, vol. 6, p. 103, 2004.

[82] Leach, J., Jack, B., Romero, J., Jha, A., Yao, A., Franke-Arnold, S., Ireland, D., Boyd, R., Barnett, S. and Padgett, M.: Quantum correlations in optical angle-orbital angular momentum variables. *Science*, vol. 329, p. 662, 2010.

[83] Bell, J.: On the einstein-rosen-podolsky paradox.

[84] Bell, J.: On the problem of hidden variables in quantum mechanics. *Rev. Mod. Phys.*, vol. 38, pp. 447–452, 1966.

[85] D'Ariano, G., Paris, M. and Sacchi, M.: Quantum tomography. *Adv. Imaging Electron Phys.*, vol. 128, p. 205, 2003.

[86] Fano, U.: Description of states in quantum mechanics by density matrix and operator techniques. *Rev. Mod. Phys.*, vol. 29, p. 74, 1957.

[87] Opatrný, T., Welsch, D.-G. and Vogel, W.: Least-squares inversion for density-matrix reconstruction. *Phys. Rev. A*, vol. 56, pp. 1788–1799, Sep 1997.

[88] Banaszek, K., D'Ariano, G.M., Paris, M.G.A. and Sacchi, M.F.: Maximum-likelihood estimation of the density matrix. *Phys. Rev. A*, vol. 61, p. 010304, Dec 1999.

[89] James, D., Kwiat, P., Munro, W. and White, A.: Measurement of qubits. *Phys. Rev. A*, vol. 64, p. 052312, 2001.

[90] Thew, R., Nemoto, K., White, A. and Munro, W.: Qudit quantum-state tomography. *Phys. Rev. A*, vol. 66, p. 012303, 2002.

[91] Molina-Terriza, G., Vaziri, A., Rehacek, J., Hradil, Z. and Zeilinger, A.: Triggered qutrits for quantum communication protocols. *Phys. Rev. Lett.*, vol. 92, no. 16, p. 167903, Apr 2004.

[92] Resch, K.J., Walther, P. and Zeilinger, A.: Full characterization of a three-photon greenberger-horne-zeilinger state using quantum state tomography. *Phys. Rev. Lett.*, vol. 94, no. 7, p. 070402, Feb 2005.

[93] Matsukevich, D.N., Maunz, P., Moehring, D.L., Olmschenk, S. and Monroe, C.: Bell inequality violation with two remote atomic qubits. *Phys. Rev. Lett.*, vol. 100, no. 15, p. 150404, Apr 2008.

[94] Press, W.H., Teukolsky, S.A., Vetterling, W.T. and Flannery, B.P.: *Numerical Recipes in C*. Cambridge University Press, 2002.

[95] Edgar, M., Tasca, D., Izdebski, F., Warburton, R., Leach, J., Agnew, M., Buller, G., Boyd, R. and Padgett, M.: Imaging high-dimensional spatial entanglement with a camera. *Nature Comm.*, vol. 3, p. 984, 2012.

[96] Barreiro, J.T., Langford, N.K., Peters, N.A. and Kwiat, P.G.: Generation of hyper-entangled photon pairs. *Phys. Rev. Lett.*, vol. 95, no. 26, p. 260501, Dec 2005.

[97] Agnew, M., Leach, J., McLaren, M., Roux, F. and Boyd, R.: Tomography of the quantum state of photons entangled in high dimensions. *Phys. Rev. A*, vol. 84, p. 062101, 2011.

[98] Yao, A.M.: Angular momentum decomposition of entangled photons with an arbitrary pump. *New. J. Phys*, vol. 13, no. 5, p. 053048, 2011.

[99] Collins, D., Gisin, N., Linden, N., Massar, S. and Popescu, S.: Bell inequalities for arbitrarily high-dimensional systems. *Phys. Rev. Lett.*, vol. 88, p. 040404, 2002.

[100] Jozsa, R.: Fidelity for mixed quantum states. *J. Mod. Opt.*, vol. 41, p. 2315, 1994.

[101] Pors, B., Miatto, F., Hooft, G., Eliel, E. and Woerdmann, J.: High-dimensional entanglement with orbital-angular-momentum states of light. *J. Opt.*, vol. 13, p. 064008, 2011.

[102] Krenn, M., Fickler, R., Huber, M., Lapkiewicz, R., Plick, W., Ramelow, S. and Zeilinger, A.: Entangled singularity patterns of photons in ince-gauss modes. *Phys. Rev. A*, vol. 87, p. 012326, 2013.

[103] Jack, B., Yao, A., Leach, J., Romero, J., Franke-Arnold, S., Ireland, D., Barnett, S. and Padgett, M.: Entanglement of arbitrary superpositions of modes within two-dimensional orbital angular momentum state spaces. *Phys. Rev. A*, vol. 81, no. 4, p. 43844, 2010.

[104] Vaziri, A., Weihs, G. and Zeilinger, A.: Experimental two-photon, three-dimensional entanglement for quantum communication. *Phys. Rev. Lett.*, vol. 89, no. 24, p. 240401, 2002.

[105] Romero, J., Leach, J., Jack, B., Dennis, M., Franke-Arnold, S., Barnett, S. and Padgett, M.: Entangled optical vortex links. *Phys. Rev. Lett.*, vol. 106, no. 10, p. 100407, 2011.

[106] Molina-Terriza, G., Torres, J. and Torner, L.: Management of the angular momentum of light: Preparation of photons in multidimensional vector states of angular momentum. *Phys. Rev. Lett.*, vol. 88, p. 013601, 2001.

[107] Monken, C., Ribeiro, P. and Pádua, S.: Transfer of angular spectrum and image formation in spontaneous parametric down-conversion. *Phys. Rev. A*, vol. 57, no. 4, pp. 3123–3126, 1998.

[108] C.K., H., Ou, Z. and Mandel, L.: Measurement of subpicosecond time intervals between two photons by interference. *Phys. Rev. Lett.*, vol. 59, pp. 2044–2046, 1987.

[109] Caetano, D.P., Almeida, M.P., Ribeiro, P.H.S., Huguenin, J.A.O., dos Santos, B.C. and Khoury, A.Z.: Conservation of orbital angular momentum in stimulated down-conversion. *Phys. Rev. A*, vol. 66, no. 4, p. 041801, 2002.

[110] Martinelli, M., Huguenin, J.O., Nussenzveig, P. and Khoury, A.Z.: Orbital angular momentum exchange in an optical parametric oscillator. *Phys. Rev. A*, vol. 70, no. 1, p. 013812, 2004.

[111] Dos Santos, B.C., Khoury, A.Z. and Huguenin, J.A.O.: Transfer of orbital angular momentum in a multimode parametric oscillator. *Opt. Lett.*, vol. 33, no. 23, pp. 2803–2805, 2008.

[112] Walborn, S., De Oliveira, A., Thebaldi, R. and Monken, C.: Entanglement and conservation of orbital angular momentum in spontaneous parametric down-conversion. *Phys. Rev. A*, vol. 69, no. 2, p. 23811, 2004.

[113] Osorio, C., Molina-Terriza, G. and Torres, J.: Correlations in orbital angular momentum of spatially entangled paired photons generated in parametric down-conversion. *Phys. Rev. A*, vol. 77, no. 1, p. 15810, 2008.

[114] Osorio, C., Molina-Terriza, G. and Torres, J.: Orbital angular momentum correlations of entangled paired photons. *J. of Opt. A*, vol. 11, p. 094013, 2009.

[115] Clifford, M., Arlt, J., Courtial, J. and Dholakia, K.: High-order Laguerre-Gaussian laser modes for studies of cold atoms. *Optics Comm.*, vol. 156, no. 4-6, pp. 300–306, 1998.

[116] Siegman, A.: *Lasers*. CA: University Science Books, 1986.

[117] Nogueira, W., Walborn, S., Pádua, S. and Monken, C.: Generation of a two-photon singlet beam. *Phys. Rev. Lett.*, vol. 92, no. 4, p. 43602, 2004.

[118] Gomes, R., Salles, A., Toscano, F., Souto Ribeiro, P. and Walborn, S.: Quantum entanglement beyond gaussian criteria. *Proc. Nat. Acad. Sci. USA*, vol. 106, p. 21517, 2012.

[119] Delaubert, V., Shaddock, D., Lam, P., Buchler, B., Bachor, H. and McClelland, D.: Generation of a phase-flipped gaussian mode for optical measurements. *J. Opt. A: Pure and Applied Optics*, vol. 4, p. 393, 2002.

[120] Kimel, I. and Elias, L.: Relations between hermite and laguerre gaussian modes. *IEEE J of Quantum Electron*, vol. 29, p. 00, 1993.

[121] Abramowitz, M. and Stegun, I.: *Handbook of mathematical functions*. Dover, 1972.

[122] Walborn, S., De Oliveira, A., Pádua, S. and Monken, C.: Multimode hong-ou-mandel interference. *Phys. Rev. Lett.*, vol. 90, no. 14, p. 143601, 2003.

[123] Berkhout, G., Lavery, M., Courtial, J., Beijersbergen, M. and Padgett, M.: Efficient sorting of orbital angular momentum states of light. *Phys. Rev. Lett.*, vol. 105, no. 15, p. 153601, 2010.

[124] Souza, C. and Khoury, A.: A michelson controlled-not gate with a single-lens astigmatic mode converter. *Opt. Express*, vol. 18, no. 9, pp. 9207–9212, 2010.

[125] Arrizon, V.: Optimum on-axis computer-generated hologram encoded into low-resolution phase- modulation devices. *Opt. Lett.*, vol. 28, pp. 2521–2523, 2003.

[126] Durnin, J.: Exact solutions for nondiffracting beams. i. the scalar theory. *J. of Opt. of America A*, vol. 4, pp. 651–654, 1987.

[127] Durnin, J., Miceli Jr., J. and Eberly, J.: Diffraction-free beams. *Phys. Rev. Lett.*, vol. 58, pp. 1499–1501, 1987.

[128] Gori, F., Guattari, G. and Padovani, C.: Bessel-gauss beams. *Opt. Commun.*, vol. 64, pp. 491–495, 1987.

[129] Turunen, J., Vasara, A. and Friber, A.: Holographic generation of diffraction-free beams. *App. Opt.*, vol. 27, pp. 3959–3962, 1988.

[130] Bose, S. and Vedral, V.: Mixedness and teleportation. *Phys. Rev. A*, vol. 61, p. 040101(R), 2000.

[131] McLaren, M., Agnew, M., Leach, J., Roux, F., Padgett, M., Boyd, R. and Forbes, A.: Entangled bessel-gaussian beams. *Opt. Express*, vol. 20, pp. 23589–23597, 2012.

[132] McLaren, M., Romero, J., Padgett, M., Roux, F. and Forbes, A.: Two-photon optics of bessel-gaussian modes. *Phys. Rev. A*, vol. 88, p. 033818, 2013.

[133] Scarani, V., Bechmann-Pasquinucci, H., Cerf, N., Dusek, M., Lütkenhaus, N. and Peev, M.: The security of practical quantum key distribution. *Rev. Mod. Phys.*, vol. 81, pp. 1301–1350, 2009.

[134] Nagali, E. and Sciarrino, F.: Generation of hybrid polarization-orbital angular momentum entangled states. *Opt. Express*, vol. 18, pp. 18243–18248, 2010.

[135] Yu, T. and Eberly, J.: Sudden death of entanglement. *Science Rev.*, vol. 323, pp. 598–601, 2009.

[136] Kielpinski, D., Meyer, V., Rowe, M., Sackett, C., Itano, W., Monroe, C. and Wineland, D.: A decoherence-free quantum memory using trapped ions. *Science*, vol. 291, pp. 1013–1015, 2001.

[137] Viola, L., Fortunato, E., Pravia, M., Knill, E., Laflamme, R. and Gory, D.: Experimental realization of noiseless subsystems for quantum information processing. *Science*, vol. 293, pp. 2059–2063, 2001.

[138] Giovannini, D., Nagali, E., Marrucci, L. and Sciarrino, F.: Resilience of orbital-angular-momentum photonic qubits and effects on hybrid entanglement. *Phys. Rev. A*, vol. 83, p. 042338, 2011.

[139] Morikoshi, F.: Recovery of entanglement lost in entanglement manipulation. *Phys. Rev. Lett.*, vol. 84, pp. 3189–3192, 2000.

[140] Hamadou Ibrahim, A., Roux, F., McLaren, M., Konrad, T. and Forbes, A.: Orbital-angular-momentum entanglement in turbulence. *Phys. Rev. A*, vol. 88, p. 012312, 2013.

[141] Zhao, S., Leach, J., Gong, L., Ding, J. and Zheng, B.: Aberration corrections for free-space optical communications in atmosphere turbulence using orbital angular momentum states. *Opt. Express*, vol. 20, pp. 452–461, 2011.

[142] Brünner, T. and Roux, F.: Robust entangled qutrit states in atmospheric turbulence. *New J. Phys.*, vol. 15, p. 063005, 2013.

[143] Rodenburg, B., Mirhosseini, M., Malik, M., Yanakas, M., Maher, L., Steinhoff, N., Tyler, G. and Boyd, R.: Simulating thick atmospheric turbulence in the lab with application to orbital angular momentum communication. *arXiv:1301.7454*, 2013.

[144] McGloin, D., Garcés-Chávez, V. and Dholakia, K.: Interfering bessel beams for optical micromanipulation. *Opt. Lett.*, vol. 28, pp. 657–659, 2003.

[145] Litvin, I., McLaren, M. and Forbes, A.: A conical wave approach to calculating bessel-gauss beam reconstruction after complex obstacles. *Opt. Commun.*, vol. 282, pp. 1078–1082, 2009.

[146] Cruz-Ramírez, H., Ramírez-Alarcón, R., Morelos, F.J., Quinto-Su, P.A., Gutiérrez-Vega, J.C. and Uŕen, A.B.: Observation of non-diffracting behavior at the single-photon level. *Opt. Express*, vol. 20, p. 29761, 2012.

[147] McGloin, D. and Dholokia, K.: Bessel beams: diffraction in a new light. *Contemporary Physics*, vol. 46, pp. 15–28, 2012.

[148] Bouchal, Z., Wagner, J. and Chlup, M.: Self-reconstruction of a distorted nondiffracting beam. *Opti. Commun.*, vol. 151, pp. 207–211, 1998.

[149] Cottrell, D., Craven, J. and Davis, J.: Nondiffracting random intensity patterns. *Opt. Lett.*, vol. 32, pp. 298–300, 2007.

[150] Jack, B., Leach, J., Ritsch, H., Barnett, S. and Padgett, M.: Precise quantum tomography of photon pairs with entangled orbital angular momentum. *New J. of Phys.*, vol. 811, p. 103024, 2009.

[151] Hill, S. and Wootters, W.: Entanglement of a pair of quantum bits. *Phys. Rev. Lett.*, vol. 78, pp. 5022–5025, 1997.

[152] Schwinger, J.: Unitary operator bases. *Proceedings of the national academy of sciences of the United States Of America*, vol. 46, no. 4, p. 570, 1960.

[153] Ivonovic, I.: Geometrical description of quantal state determination. *Journal of Physics A: Mathematical and General*, vol. 14, p. 3241, 1981.

[154] Wootters, W. and Fields, B.: Optimal state-determination by mutually unbiased measurements. *Annuals of Physics*, vol. 191, no. 2, pp. 363–381, 1989.

[155] Adamson, R.B.A. and Steinberg, A.M.: Improving quantum state estimation with mutually unbiased bases. *Phys. Rev. Lett.*, vol. 105, p. 030406, 2010.

[156] Fernández-Pérez, A., Klimov, A.B. and Saavedra, C.: Quantum process reconstruction based on mutually unbiased basis. *Phys. Rev. A*, vol. 83, p. 052332, 2011.

[157] Giovannini, D., Romero, J., Leach, J., Dudley, A., Forbes, A. and Padgett, M.: Characterization of high-dimensional entangled systems via mutually unbiased measurements. *Phys. Rev. Lett.*, vol. 110, p. 143601, 2013.

[158] Calderbank, A., Rains, E., Shor, P. and Sloane, N.: Quantum error correction and orthogonal geometry. *Phys. Rev. Lett.*, vol. 78, no. 3, pp. 405–408, 1997.

[159] Gottesman, D.: Class of quantum error-correcting codes saturating the quantum hamming bound. *Phys. Rev. A*, vol. 54, pp. 1862–1868, 1996.

[160] Bennett, C., Brassard, G. *et al.*: Quantum cryptography: Public key distribution and coin tossing. In: *Proceedings of IEEE International Conference on Computers, Systems and Signal Processing*, vol. 175. Bangalore, India, 1984.

[161] Barnett, S.M.: *Quantum Information*. Oxford University Press, 2009.

[162] Durt, T., Englert, B.-G., Bengtsson, I. and Zyczkowski, K.: On mutually unbiased bases. *International Journal of Quantum Information*, vol. 8, no. **, pp. 535–640, 2010.

[163] Sheridan, L. and Scarani, V.: Security proof for quantum key distribution using qudit systems. *Phys. Rev. A*, vol. 82, p. 030301, 2010.

[164] Ferenczi, A. and Lütkenhaus, N.: Symmetries in quantum key distribution and the connection between optimal attacks and optimal cloning. *Phys. Rev. A*, vol. 85, p. 052310, 2012.

[165] Mafu, M., Dudley, A., Goyal, S., Giovannini, D., McLaren, M., Padgett, M., Konrad, T., Petruccione, F., Lütkenhaus, H. and Forbes, A.: Higher-dimensional orbital angular momentum based quantum key distribution with mutually unbiased bases. *Phys. Rev. A*, vol. 46, pp. 15–28, 2013.

[166] Paterson, C.: Atmospheric turbulence and orbital angular momentum of single photons for optical communication. *Phys. Rev. Lett.*, vol. 94, p. 153901, 2005.

[167] Anguita, J., Neifeld, M. and Vasic, B.: Turbulence-induced channel crosstalk in an orbital angular momentum-multiplexed free-space optical link. *Phys. Rev. A*, vol. 47, pp. 2414–2429, 2008.

[168] Smith, B. and Raymer, M.: Two-photon wave mechanics. *Phys. Rev. A*, vol. 74, p. 062104, 2006.

[169] Fried, D.: Optical resolution through a randomly inhomogeneous medium for very long and very short exposures. *J. Opt. Soc. Am.*, vol. 56, pp. 1372–1379, 1966.

[170] Ursin, R., Tiefenbacher, F., Schmitt-Manderbach, T., Weier, H., Scheidl, T., Lindenthal, M., Blauensteiner, B., Jennewein, T., Perigues, J., Trojek, P., Ömer, B., Fürst, M., Meyenburg, M., Rarity, J., Sodnik, Z., Barbieri, C., Weinfurter, H. and Zeilinger, A.: Entanglement-based quantum communication over 144 km. *Nature Phys.*, vol. 3, pp. 481–486, 2007.